UNIVERSITY OF CALIFORNIA
RIVERSIDE

Surface Chemistry and Catalysis from First Principles

A Dissertation submitted in partial satisfaction
of the requirements for the degree of

Doctor of Philosophy

in

Chemistry

by

Guoxiang Hu

June 2018

Dissertation Committee:
Dr. De-en Jiang, Chairperson
Dr. Francisco Zaera
Dr. Gregory Beran

The Dissertation of Guoxiang Hu is approved:

_____

_____

_____

Committee Chairperson

University of California, Riverside

ACKNOWLEDGMENTS

First of all, I would like to give my sincere appreciation to my research advisor, Prof. De-en Jiang, for his valuable guidance, help and support during my PhD study. I absolutely admire his working style, and it has a very positive impact on my research. He is not only a great teacher, but also a very nice friend. I really enjoyed our group activities, including the parties, group travel to the beach and Mexico, et al.

I am grateful to my committee members, including Prof. Leonard Mueller, Prof. Gregory Beran, Prof. Eric Chronister, and Prof. Francisco Zaera, for the very helpful comments on my SYRE, qualifying exam, and dissertation defense. I also want to thank Prof. Christopher Bardeen, Prof. David Bocian, Prof. Jingsong Zhang, and Prof. Chia-en Chang for their great teaching during my first year of the PhD study.

I want to thank our experimental collaborators: Dr. Zili Wu at Oak Ridge National Laboratory (ORNL) for the valuable suggestions on the titanium dioxide and gold nanocluster projects, Prof. Yujie Sun at Utah State University for the nice collaboration on electrochemical water splitting on nitrogen doped transition metals, Prof. Dunwei Wang at Boston College for the helpful discussions on the selective methane oxidation at ambient conditions, Prof. Rongchao Jin at Carnegie Mellon University for the helpful comments on the thiolate-gold interface paper, Dr. Sheng Dai at ORNL and University of Tennessee for the helpful comments on the h-BN/metal paper, Prof. Dongil Lee at Yonsei University for the collaborations on hydrogen evolution reaction on gold nanoclusters, Prof. Yuichi Negishi at Tokyo University of Science for the collaboration on the thiolate-protected trimetallic alloy clusters, Prof. Shengqian Ma at University of South Florida for

the collaboration on hydrogen evolution reaction on hollow iron/molybdenum-nitrogen-doped porous carbon, and Prof. Lei Zhu at Florida State University for the collaboration on fluorescence of hydroxyphenyl-substituted “click” triazoles.

I would like to thank Jiang group members. I cannot be so happy and productive without them. I am grateful to their friendly help and valuable discussions: Dr. Qing Tang, Dr. Ziqi Tian, Dr. Bo Li, Dr. Runhong Huang, Dr. Huilong Dong, Dr. Rui Li, Cheng Zhan, Victor Fung, Chad Priest, Song Wang, Yangyunli Sun, Nicole Onishi, Rui Xie, Shaoze Zhang, Yadong Zhang, Jingwei Zhou, Weihong Wu, Cai Ning. I am also grateful to my friends at UCR for sharing their time with me for the colorful activities. I thank Ji Feng, Yufei Ni, Yaokai Duan, Shen Zhang, et al.

I am grateful to my lovely boyfriend, Nan Zhang, for his five-year accompany, his cooking of delicious food, and his support of my work. I thank my parents, who are in China now, for everything they give me.

We gratefully acknowledge the financial support from University of California, Riverside and the U.S. Department of Energy (DOE), Office of Science, Office of Basic Energy Sciences, Chemical Sciences, Geosciences, and Biosciences Division. We thank the computational resources from the National Energy Research Scientific Computing Center.

My apologies if I missed anyone. Best wishes to all.

Published materials are used as the following:

Chapter 3: Hu, G.; Tang, Q.; Jiang, D., CoP for Hydrogen Evolution: Implications from Hydrogen Adsorption. *Phys. Chem. Chem. Phys.* **2016**, *18*, 23864-23871.

Chapter 4: Hu, G.; Wu, Z.; Dai, S.; Jiang, D., Interface Engineering of Earth-Abundant Transition Metals by Boron Nitride for Selective Electroreduction of CO_2. *ACS Appl. Mater. Interfaces* **2018,** *10*, 6694-6700.

Chapter 5: Hu, G.; Jin, R.; Jiang, D., Beyond the Staple Motif: New Order at the Thiolate-gold Interface. *Nanoscale* **2016**, *8*, 20103-20110.

Chapter 6: Hu, G.; Tang, Q.; Lee, D.; Wu, Z.; Jiang, D., Metallic Hydrogen in Atomically Precise Gold Nanoclusters. *Chem. Mater.* **2017**, *29*, 4840-4847.

Chapter 7: Hu, G.; Wu, Z.; Jiang, D., Stronger-Than-Pt Hydrogen Adsorption in a Au_{22} Nanocluster for Hydrogen Evolution Reaction. *J. Mater. Chem. A* **2018**, 6, 7532-7537.

Chapter 9: Hu, G.; Wu, Z.; Jiang, D., First Principles Insight into H_2 Activation on the Surfaces of Different TiO_2 polymorphs. *In preparation*.

ABSTRACT OF THE DISSERTATION

Surface Chemistry and Catalysis from First Principles

by

Guoxiang Hu

Doctor of Philosophy, Graduate Program in Chemistry
University of California, Riverside, June 2018
Dr. De-en Jiang, Chairperson

Hydrogen-catalyst interaction is the foundation of many technologies and processes. Herein we employ first principles density functional theory (DFT) techniques to investigate how hydrogen interacts with different catalytic systems, including cobalt phosphide (CoP), h-BN monolayer supported on transition metals (h-BN/metal), atomically precise gold nanoclusters, and titanium dioxide (TiO_2). Our study has important implications for the use of the catalysts for hydrogen evolution reaction (HER), CO_2 reduction, and H_2 activation.

Electrochemical HER using renewable energy can provide a sustainable supply of fuel for future societies with hydrogen as a key energy carrier. CoP is one of the most active earth-abundant electrocatalysts for HER. We have studied the adsorption structures and energetics of atomic hydrogen on several low-Miller-index surfaces of CoP. We find that CoP(111) is the most promising facet for high and long-lived HER activity. Compared to HER, CO_2 reduction is much harder. Since HER competes with CO_2

reduction at all negative potentials, a key criterion for selective catalysts in CO_2 reduction is the avoidance of HER. We have investigated the electrocatalytic activities of h-BN/Ni, h-BN/Co, and h-BN/Cu. We find that the competitive HER channel can be filtered out by the surface h-BN monolayer for h-BN/Ni and h-BN/Co, making them very good electrocatalysts for CO_2 reduction.

Atomically precise gold nanoclusters are a new class of catalysts, and it is able to establish structure-activity correlations due to their well-defined structures. Thiolate-protected gold nanoclusters have received considerable research attention, and have been reported to exhibit high HER activity. We have studied the thiolate-gold interface and find that the interfacial structures of thiolates on gold are surface sensitive. To understand HER on the thiolate-protected gold nanoclusters, we have studied how hydrogen interacts with $[Au_{25}(SR)_{18}]^q$ clusters (q=-1, 0, +1) and monoatom-doped bimetallic $[M_1Au_{24}(SR)_{18}]^q$ clusters (M=Pt, Pd, Ag, Cu, Hg, Cd, and q=-2, -1, 0). We conclude that $PtAu_{24}(SR)_{18}$, $PdAu_{24}(SR)_{18}$, and $CuAu_{24}(SR)_{18}$ clusters can be very good electrocatalysts for HER. Unlike the above thiolate-protected gold nanoclusters, where the surface gold atoms are fully coordinated by the thiolates, the $Au_{22}(L^8)_6$ cluster (L = 1,8-bis(diphenylphosphino) octane) is unique in that it contains eight coordinatively unsaturated (*cus*) gold atoms. We find that the eight *cus* gold atoms in the $Au_{22}(L^8)_6$ cluster can adsorb hydrogen stronger than Pt, thereby being a potentially promising catalyst for HER.

Hydrogen interaction with metal oxides is of growing interest recently. TiO_2 is one of the most extensively investigated metal oxides. We have studied the mechanisms of H_2

activation on the surfaces of different TiO_2 polymorphs, including rutile TiO_2(110), anatse TiO_2(101), and brookite TiO_2(210). We find that for all the three surfaces, although the homolytic dissociation of H_2 is thermodynamically more favorable, the heterolytic pathway is kinetically more favorable.

Table of Contents

List of Figures

List of Tables

Chapter 1

Introduction

This dissertation focuses on using first principles DFT to understand hydrogen interaction with different catalytic systems, including earth abundant materials, atomically precise gold nanoclusters, and titanium dioxide (TiO_2) surfaces. The study has important implications for the use of the catalysts for electrochemical hydrogen evolution reaction (HER), CO_2 reduction, and H_2 activation. Specifically speaking, this dissertation includes HER on different surfaces of CoP, CO_2 reduction on h-BN/metal (metal = Ni, Co, and Cu), HER on atomically precise gold nanoclusters, and H_2 activation on the surfaces of different TiO_2 polymorphs.

Chapter 2 shows the detailed computational methods. Briefly speaking, for solids and surfaces, the DFT calculations were performed with the Vienna *ab initio* simulation package (VASP) with periodic boundary conditions (PBC).[1] For molecules and metal nanoclusters, the calculations were performed with the Turbomole program (Version 6.5)[2] without the periodic boundary conditions.

Chapter 3 presents HER on different surfaces of CoP. The increasing global energy demands prompt intense research efforts in the exploration of catalytic systems for the conversion and storage of renewable energies. Electrocatalytic water splitting with renewable energy input, to produce hydrogen gas offers a promising strategy for this purpose.[3] The electricity needed to produce hydrogen can be provided by renewable

energy sources such as photovoltaic, wind and tidal power. Efficient water splitting requires high performance catalysts to facilitate its two half-reactions: hydrogen evolution reaction (HER) at the cathode and oxygen evolution reaction (OER) at the anode. Table 1.1 lists the chemical equations of HER and OER in acidic and alkaline solutions. To date, platinum is the most efficient electrocatalyst for HER. However, the low natural abundance and high cost of platinum hamper its wide use at the industrial scale. Thus, it is highly desirable to develop efficient, low-cost and earth-abundant electrocatalysts for HER.

Table 1.1. Chemical equations of HER and OER in acidic and alkaline solutions.

	Acidic solution	**Alkaline solution**
HER at the cathode	$2H^+(aq) + 2e^- \rightarrow H_2(g)$	$2H_2O(l) + 2e^- \rightarrow H_2(g) + 2OH^-(aq)$
OER at the anode	$2H_2O(l) \rightarrow O_2(g) + 4H^+(aq) + 4e^-$	$4OH^-(aq) \rightarrow O_2(g) + 2H_2O(l) + 4\ e^-$

CoP has been reported to be one of the most active, acid-stable, earth-abundant electrocatalysts for HER.[4] However, the nature of its high HER activity keeps unknown. For the mechanism of HER in acid media, two types of pathways have been proposed: the Volmer–Heyrovsky and the Volmer–Tafel mechanism. The Volmer reaction refers to the initial adsorption of protons from the acid solution to form adsorbed H ($H^+ + e^- \rightarrow H_{ad}$).[5] In the Volmer–Heyrovsky mechanism, the adsorbed hydrogen reacts with a solvated proton from the water layer to form H_2 ($H_{ad} + H^+ + e^- \rightarrow H_2$),[6] while in the Volmer–Tafel mechanism, the adsorbed hydrogen reacts with another adsorbed surface hydrogen to form H_2 ($H_{ad} + H_{ad} \rightarrow H_2$).[7] Obviously, hydrogen adsorption is very

important during the process of HER. In addition, Nørskov group has reported that Gibbs free energy of hydrogen adsorption (ΔG_H) is a descriptor for HER, and good HER catalysts are expected to have close-to-zero ΔG_H.[8] Therefore, we study the adsorption of hydrogen on (111), (110), (100), and (011) surfaces of CoP from first principles DFT in chapter 3. By calculating ΔG_H, we predicted the HER activities of the surfaces. With *ab initio* atomistic thermodynamics, we determined the most stable surface at the experimental conditions (1 atm H_2 pressure and 300K). We find that the (111) surface of CoP is the most promising facet for high and long-lived HER activity. The key feature of hydrogen adsorption on CoP(111) is that both Co bridge sites and P top sites are able to adsorb hydrogen with close-to-zero ΔG_H and that there is a synergy of Co and P atoms in adsorbing hydrogen.

Besides HER, we are also interested in CO_2 reduction. Electrochemical CO_2 can not only produce useful fuels but also low the atmospheric level of CO_2. Numerous researchers have studied electrochemical CO_2 reduction at the metal catalysts.[9] Compared to HER, CO_2 reduction is much harder. Since HER competes with CO_2 reduction at the cathode at all negative potentials, a key criterion for selective catalysts in CO_2 reduction is the avoidance of HER in the presence of CO_2.[10] Therefore, it is interesting to investigate if we can tune the selectivity of CO_2 reduction vs. HER by surface/interface engineering of the metal catalysts. It has been reported that monolayers of h-BN can be grown on various transition metals by chemical vapor deposition (CVD). Moreover, it has been shown that gold supported h-BN monolayers are very active for oxygen reduction reaction (ORR). The interesting point is that neither h-BN or Au shows high

catalytic activity for ORR.[11] Motivated by the importance of electrochemical CO_2 reduction and the potential of h-BN/metal as electrocatalysts, in Chapter 4, we study the electrocatalytic activities of h-BN/metal (metal = Ni, Co, and Cu) for CO_2 reduction from first principles DFT. We are focused on tuning the selectivity of CO_2 reduction vs. HER by surface engineering of the metal catalysts with h-BN monolayer.

For the mechanism of CO_2 reduction, the first protonation of CO_2 can proceed via two channels: (i) at the C atom to form *HCOO ($* + CO_2 + H^+ + e^- \rightarrow *HCOO$), then to HCOOH ($*HCOO + H^+ + e^- \rightarrow HCOOH$); (ii) at the O atom to form *COOH ($* + CO_2 + H^+ + e^- \rightarrow *COOH$), then to CO and H_2O ($*COOH + H^+ + e^- \rightarrow *CO + H_2O$).[12] Thus, the key intermediates for HER, CO_2 reduction to HCOOH, and CO_2 reduction to CO are H, HCOO, and COOH, respectively. To study the electrochemical activities of h-BN/Ni, h-BN/Co, and h-BN/Cu for HER and CO_2 reduction, we first examined their geometry and electronic structures. Then, we computed the binding energies of the key intermediates on h-BN, metal, and h-BN/metal. At last, we employed the computational hydrogen electrode model[13] to evaluate the free energy diagrams for HER and CO_2 reduction as well as their competition on these materials. We find that H binding on the metal can be significantly weakened by the h-BN monolayer, but the binding strength of HCOO is strong on both the metal and h-BN/metal, especially for Ni and Co. This different adsorption leads to selectivity control for HER vs. CO_2 reduction. We find that h-BN/Ni and h-BN/Co can be very good electrocatalysts for CO_2 reduction to HCOOH, because the competitive HER channel is filtered out.

Atomically precise gold nanoclusters are a new class of catalysts, and it is able to establish structure-activity correlations due to their well-defined structures.[14] Recently, it has been reported that both $Au_{25}(SR)_{18}$ and $PtAu_{24}(SR)_{18}$ exhibit high HER activity; more interestingly, the activity of $PtAu_{24}(SR)_{18}$ is much higher than that of $Au_{25}(SR)_{18}$, and $PtAu_{24}(SR)_{18}$ is among the most active molecular catalysts for HER.[15] It is therefore of great interest to investigate hydrogen interaction with atomically precise gold nanoclusters.

Chapter 5 presents the study of the interfacial structures between the ligands and gold. We find that the interfacial structures of thiolates on gold are surface sensitive: while a staple motif (such as –RS–Au–SR–) is preferred on Au(111), a bridging motif (–RS–) is preferred on Au(100) and Au(110). We further confirm the preference of the bridging motif for self-assembled monolayers (SAMs) on Au(100). With this surface sensitivity, we categorize the structure-known $Au_n(SR)_m$ clusters into three groups: (1) no bridging; (2) ambiguous bridging; (3) distinct bridging.

To understand HER on the thiolate-protected gold nanoclusters, in chapter 6, we study how hydrogen interacts with $[Au_{25}(SR)_{18}]^q$ clusters (q=-1, 0, +1) and monoatom-doped bimetallic $[M_1Au_{24}(SR)_{18}]^q$ clusters (M=Pt, Pd, Ag, Cu, Hg, Cd, and q=-2, -1, 0). We especially focus on the binding sites and energetics of hydrogen in the clusters and the changes to their superatomic free-electron count. We find that hydrogen behaves as a metal in these clusters and contributes its 1s electron to the superatomic free-electron count. By calculating ΔG_H, we predict that $PtAu_{24}(SR)_{18}$, $PdAu_{24}(SR)_{18}$, and $CuAu_{24}(SR)_{18}$ clusters can be very good electrocatalysts for HER. Our prediction of the

higher HER activity of $PtAu_{24}(SR)_{18}$ than $Au_{25}(SR)_{18}$ is in good agreement with the experimental results reported by Lee's group.

Unlike the above thiolate-protected Au nanoclusters, where the surface Au atoms are fully coordinated by the thiolate ligands, the $Au_{22}(L^8)_6$ cluster (L = 1,8-bis(diphenylphosphino) octane) is unique in that it contains eight coordinatively unsaturated (*cus*) Au atoms.[16] In Chapter 7, we investigate the interaction between hydrogen and the $Au_{22}(L^8)_6$ cluster. We find that the eight *cus* gold atoms in the $Au_{22}(L^8)_6$ cluster can adsorb hydrogen stronger than Pt, thereby being a potentially promising catalyst for HER. From the HOMO-LUMO gaps, frontier orbitals, and Bader charge analysis, we conclude that hydrogen behaves as a hydride or electron-withdrawing ligand in the $Au_{22}(L^8)_6$ clusters, in contrast with the metallic hydrogen in thiolate-protected gold nanoclusters. This study demonstrates the behavior of hydrogen in ligand-protected gold nanoclusters is ligand dependent and ligand-protected gold clusters with *cus* gold sites will be excellent electrocatalysts for HER.

Since atomically precise metal nanoclusters with their well-defined structures are a promising class of model catalysts to establish structure-activity correlations, especially for electrocatalysis where the reactions take place in ambient conditions, in Chapter 8, we highlight recent advances in electrocatalysis by atomically precise metal nanoclusters (mainly focused on gold and copper nanoclusters) for water splitting, CO_2 reduction, and some other reactions. These metal nanoclusters can be either used as homogeneous catalysts in solutions or loaded onto solid supports as heterogeneous catalysts. We also

point out several interesting directions to fully realize the potential of atomically precise nanoclusters in electrocatalysis.

So far, we have discussed hydrogen interaction with three-dimensional (CoP), two-dimensional (h-BN monolayer), and zero-dimensional (atomically precise gold nanoclusters) materials. Recently, it has been shown that hydrogen interaction with metal oxides is of growing interest.[17] Among the metal oxides, TiO_2 is one of the most important and extensively studied systems. Therefore, in Chapter 9, we study H_2 activation on the surfaces of different TiO_2 polymorphs, including rutile TiO_2(110), anatse TiO_2(101), and brookite TiO_2(210). We find that for all the three surfaces, although the homolytic dissociation of H_2 is thermodynamically more favorable, the heterolytic pathway is kinetically more favorable. For rutile TiO_2(110) and brookite TiO_2(210), the hydrides which are produced by the heterolytic dissociation of H_2 can easily transfer from Ti to O, finally yielding the homolytic products. However, for anatase TiO_2(101), the barrier of hydrogen transfer form Ti to O is very high. This indicates that hydrides on anatase TiO_2(101) can be kinetically stabilized. Thus, it is expected that hydrides on anatase TiO_2(101) can be experimentally detected by ^{1}H-NMR or INS. In addition, the hydrides can be evolved in the hydrogenation reactions of C-C or C-O multiple bonds.

In summary, this dissertation has presented hydrogen interaction with different dimensional materials and the applications of the materials in catalysis, such as HER, CO_2 reduction, and H_2 activation, by first principles DFT. DFT has been widely used in physics, chemistry and materials science to investigate the electronic structure of various

materials, and normally can yield satisfactory description of the materials. With an ultimate goal of knowledge-based design of functional materials for a sustainable society, our study provides valuable guidelines to experimental researchers for the design of novel catalysts, and provides computational insights into the mechanisms of the catalytic reactions.

References

1. Kresse, G.; Furthmüller, J., Efficient Iterative Schemes for Ab Initio Total-Energy Calculations Using a Plane-Wave Basis Set. *Phys. Rev. B* **1996**, *54*, 11169-11186.

2. Ahlrichs, R.; Bär, M.; Häser, M.; Horn, H.; Kölmel, C., Electronic Structure Calculations on Workstation Computers: The Program System Turbomole. *Chem. Phys. Lett.* **1989**, *162*, 165-169.

3. Lubitz, W.; Tumas, W., Hydrogen: An Overview. *Chem. Rev.* **2007**, *107*, 3900-3903.

4. Popczun, E. J.; Read, C. G.; Roske, C. W.; Lewis, N. S.; Schaak, R. E., Highly Active Electrocatalysis of the Hydrogen Evolution Reaction by Cobalt Phosphide Nanoparticles. *Angew. Chem. Int. Ed.* **2014**, *53*, 5427-5430.

5. Erdey-Gruz, T.; Volmer, M., Zur Theorie Der Wasserstoffüberspannung. *Z. Phys. Chem. A* **1930**, *150*, 203.

6. Heyrovský, J., A Theory of Overpotential. *Recl. Trav. Chim. Pays-Bas* **1927**, *46*, 582-585.

7. Tafel, J., Über Die Polarisation Bei Kathodischer Wasserstoffentwicklung. *Z. phys. Chem* **1905**, *50*, 641.

8. Nørskov, J. K.; Bligaard, T.; Logadottir, A.; Kitchin, J. R.; Chen, J. G.; Pandelov, S.; Stimming, U., Trends in the Exchange Current for Hydrogen Evolution. *J. Electrochem. Soc.* **2005**, *152*, J23-J26.

9. Ma, S.; Kenis, P. J., Electrochemical Conversion of Co_2 to Useful Chemicals: Current Status, Remaining Challenges, and Future Opportunities. *Curr. Opin. Chem. Eng.* **2013**, *2*, 191-199.

10. Peterson, A. A.; Nørskov, J. K., Activity Descriptors for Co_2 Electroreduction to Methane on Transition-Metal Catalysts. *J. Phys. Chem. Lett.* **2012**, *3*, 251-258.

11. Uosaki, K.; Elumalai, G.; Noguchi, H.; Masuda, T.; Lyalin, A.; Nakayama, A.; Taketsugu, T., Boron Nitride Nanosheet on Gold as an Electrocatalyst for Oxygen Reduction Reaction: Theoretical Suggestion and Experimental Proof. *J. Am. Chem. Soc.* **2014**, *136*, 6542-6545.

12. Hori, Y., Electrochemical Co_2 Reduction on Metal Electrodes. In *Modern Aspects of Electrochemistry*, Springer: 2008; pp 89-189.

13. Peterson, A. A.; Abild-Pedersen, F.; Studt, F.; Rossmeisl, J.; Nørskov, J. K., How Copper Catalyzes the Electroreduction of Carbon Dioxide into Hydrocarbon Fuels. *Energy Environ. Sci.* **2010**, *3*, 1311-1315.

14. Chakraborty, I.; Pradeep, T., Atomically Precise Clusters of Noble Metals: Emerging Link between Atoms and Nanoparticles. *Chem. Rev.* **2017**, *117*, 8208-8271.

15. Kwak, K.; Choi, W.; Tang, Q.; Kim, M.; Lee, Y.; Jiang, D.-e.; Lee, D., A Molecule-Like $Ptau_{24}(Sc_6h_{13})_{18}$ Nanocluster as an Electrocatalyst for Hydrogen Production. *Nat. Commun.* **2017**, *8*, 14723.

16. Chen, J.; Zhang, Q.-F.; Bonaccorso, T. A.; Williard, P. G.; Wang, L.-S., Controlling Gold Nanoclusters by Diphospine Ligands. *J. Am. Chem. Soc.* **2013**, *136*, 92-95.

17. Coperet, C.; Estes, D. P.; Larmier, K.; Searles, K., Isolated Surface Hydrides: Formation, Structure, and Reactivity. *Chem. Rev.* **2016**, *116*, 8463-8505.

Chapter 2

Computational Methods

2.1 Hydrogen adsorption on CoP

Spin-polarized DFT calculations were performed by using the Vienna *ab initio* simulation package (VASP).[1] The ion-electron interaction was described with the projector augmented wave (PAW) method.[2] Electron exchange-correlation was represented by the functional of Perdew, Burke and Ernzerhof (PBE) of generalized gradient approximation (GGA).[3] A cutoff energy of 400 eV was used for the plane-wave basis set. (111), (110), (100), and (011) surfaces were examined. About 10-Å thick slabs in (2 × 2) lateral cells with 15 Å of vacuum along the z-direction were used to model the adsorbate-surface systems. The Brillouin zone was sampled by (3×3×1) Monkhorst-Pack k-point mesh. Both the layer thickness and k-point mesh were tested to achieve a convergence of hydrogen adsorption energy within 0.04 eV. The top half of the slab was allowed to relax together with the adsorbed H atoms and the convergence threshold for structural optimization was set to be 0.025 eV/Å in force. Partial atomic charges were obtained using Bader charge analysis as implemented by Henkelman and co-workers.[4] We also used a different method REPEAT[5] to derive the atomic charges.

Surface energies was determined by using

$$\gamma = \frac{E_{slab} - NE_{bulk}}{2A} \quad (1)$$

where E_{slab} is the total energy of the surface slab, E_{bulk} is the total energy of the bulk unit cell (eV/CoP), N is the number of unit formula in the slab, and A is the surface area. The differential hydrogen adsorption energy ΔE_H was calculated by

$$\Delta E_H = E(CoP + nH) - E[CoP + (n-1)H] - \frac{1}{2}E(H_2) \quad (2)$$

where $E(CoP + nH)$ and $E[CoP + (n-1)H]$ represent the total energy of the CoP system with n and n-1 adsorbed hydrogen atoms on the surface, respectively, and $E(H_2)$ represents the total energy of a gas phase H_2 molecule. A negative value of ΔE_H suggests favorable absorption. The differential Gibbs free energy of adsorption ΔG_H was obtained by

$$\Delta G_H = \Delta E_H + \Delta E_{ZPE} - T\Delta S_H \quad (3)$$

where ΔE_{ZPE} is the difference in zero point energy between the adsorbed H and H in the gas phase H_2 molecule, and ΔS_H is the entropy difference between the adsorbed H and H_2 in the gas phase at standard conditions.

Ab initio atomistic thermodynamics[6] was used to identify the most stable phase of each surface at 1 atm H_2 and 300K. The Gibbs free energy of adsorption at a specific temperature and pressure $\Delta G^{ad}(T,p)$ was calculated by

$$\Delta G^{ad}(T,p) = \frac{1}{A}\left[E^{total}(N_H) - E^{total}(0) - \frac{N_H}{2}E_{H_2}^{total} - N_H\Delta\mu_H(T,p)\right] \quad (4)$$

where $E^{total}(N_H)$ is the total energy of the CoP system with N_H hydrogen atoms adsorbed on the surface, $E^{total}(0)$ is the total energy of the clean CoP surface, and $E_{H_2}^{total}$ is the total energy of a gas phase H_2 molecule. $\Delta\mu_H(T,p)$ is the chemical potential of hydrogen at different temperatures and pressures. Equation (4) allows one to plot the

Gibbs free energy of adsorption as a function of the hydrogen chemical potential for a specific surface at a specific H coverage. At any given hydrogen chemical potential, the stability of these H-covered surfaces can then be compared. $\Delta\mu_H(T,p)$ is related to specific (T,p)-conditions by

$$\Delta\mu_H(T,p) = \Delta\mu_H(T,p^0) + \frac{1}{2}k_B T ln\left(\frac{p}{p^0}\right) \quad (5)$$

where $\Delta\mu_H(T,p^0)$ is the hydrogen chemical potential at the standard pressure which can be looked up from the thermodynamic tables.[7]

2.2 CO_2 reduction on h-BN/metal

Spin-polarized DFT calculations were performed by using the same computational methods as described in 2.1. The calculated h-BN lattice parameter is 2.504Å, which is in good agreement with the experimental value.[8] H-BN/metal surfaces were modeled with slabs with 4 layers of metal and one layer of h-BN in (4 × 4) lateral cells. In all structural optimizations, the atoms in the bottom two metal layers were fixed while the other atoms including adsorbates were fully relaxed. A vacuum space with a length of 20 Å was employed along the z-direction to avoid the artificial interactions between the slab and its repeated images. The van der Waals interactions were included *via* the DFT-D3 method.[9]

The binding energy of H (ΔE_H) was calculated by $\Delta E_H = E(catalyst + H) - E(catalyst) - \frac{1}{2}E(H_2)$, where $E(catalyst + H)$, $E(catalyst)$, and $E(H_2)$ represent the total energy of the catalyst-H system, the energy of the catalyst, and the energy of one gas phase H_2 molecule, respectively. Binding energies of HCOO (ΔE_{HCOO}) and COOH

(ΔE_{COOH}) were calculated with $\Delta E_{HCOO/COOH} = E(catalyst + HCOO/COOH) - E(catalyst) - E(CO_2) - \frac{1}{2}E(H_2)$, where $E(catalyst + HCOO/COOH)$ and $E(CO_2)$ represent the total energy of the catalyst with one adsorbed HCOO or COOH and the energy of one gas phase CO_2 molecule, respectively. A negative value of the binding energy suggests favorable adsorption.

The change in Gibbs free energy (ΔG) for all electrocatalytic steps was defined as $\Delta G = \Delta E + \Delta E_{ZPE} - T\Delta S$. ΔE can be directly determined by the DFT total energies. ΔE_{ZPE} is the zero-point energy difference between the products and the reactants, and the zero-point energy was calculated by summing vibrational frequencies ω_ν over all normal modes ν: $E_{ZPE} = \frac{1}{2}\sum \hbar\omega_\nu$. ΔS is the entropy difference between the products and the reactants. The entropies of the free molecules at 298.15 K and 1 atm were taken from the NIST database,[10] while for the adsorbed species, the vibrational entropy was considered and calculated by the methods described by Cramer.[11] The calculated zero-point energy and entropy corrections at 298.15 K for various gas-phase and adsorbed species are provided in Table 2.1 and 2.2.

Table 2.1. Zero-point energy (ZPE) and entropy (TΔS) corrections for various gas-phase species at T=298.15K.

Species	ZPE (eV)	TΔS (eV)
CO_2	0.31	0.67
CO	0.13	0.61
H_2	0.30	0.40
HCOOH	0.90	1.04
H_2O	0.60	0.67

Table 2.2. Zero-point energy (ZPE) and entropy (TΔS) corrections for the adsorbed species on Ni(111) and h-BN/Ni(111) at T=298.15K.

Surface	Species	ZPE (eV)	TΔS (eV)
Ni(111)	H*	0.17	0.01
Ni(111)	HCOO*	0.61	0.16
Ni(111)	COOH*	0.59	0.11
Ni(111)	CO*	0.17	0.09
h-BN/Ni(111)	H*	0.26	~ 0.00
h-BN/Ni(111)	HCOO*	0.66	0.14
h-BN/Ni(111)	COOH*	0.64	0.19
h-BN/Ni(111)	CO*	0.15	0.21

In order to determine the contribution of solvation effect on the free energy of reaction intermediates, we calculated the adsorption energies of HCOO and COOH on h-BN/Ni(111) covered with water molecules. A hexagonal water layer was placed on top of

the HCOO and COOH intermediates. The energy difference between the adsorption energy with and without the presence of water gives the estimation of the solvation energy. We found that HCOO and COOH were stabilized by 0.05 eV and 0.15 eV, respectively. These values are relatively small and can be neglected.

2.3 Thiolate-gold interface

DFT calculations were performed by using the same computational methods as described in 2.1. The calculated Au fcc lattice parameter is 4.169Å, which agrees reasonably with the experimental value (4.078Å). The gold surfaces were modeled with four layers of slabs in (4 × 4) lateral cells for Au(111) and Au(100), and six layers of slab in (3 × 4) lateral cells for Au(110), with 15 Å of vacuum along the z-direction. The top half of the slab was allowed to relax together with the adsorbed thiolates. The vdW interactions were included *via* the DFT-D3 method for the structural optimizations with the experimental ligand TBBT.[9]

The binding energy of the bridging motif (-RS-) was calculated by

$$E_b = E_{thiol/Au\_slab} - E_{Au\_slab} - E_{SR} \quad (6)$$

where E_{thiol/Au_slab}, E_{Au_slab}, and E_{SR} represent the total energy of the adsorbate-substrate system, the energy of the Au slab, and the energy of one gas phase SR, respectively. The binding energy of the staple motif (-RS-Au-SR-) was calculated by

$$E_b = \frac{1}{2}(E_{thiol/Au\_slab} - E_{Au\_slab} - 2E_{SR} - E_{Au}^{Bulk}) \quad (7)$$

where E_{Au}^{Bulk} is the energy of one bulk Au atom. Here we considered the energy involved in Au adatom formation needed for the staple motif.[12]

2.4 Hydrogen adsorption on atomically precise gold nanoclusters

DFT calculations with periodic boundary conditions (PBC) were performed by using the same computational methods as described in 2.1. We first put the cluster in a cubic box (30×30×30 $Å^3$) and optimized the structure of the cluster. The initial structures of the clusters are form the crystallographic information files provided by the experiments. Spin polarization was used for system of odd-number electrons. Geometry relaxations were carried out using the conjugate-gradient algorithm with a criterion that all the residual force components on each atom are less than 0.03 eV/ Å. Γ point only was used to sample the k space.

The hydrogen adsorption energies ΔE_H on the gold nanoclusters were calculated by

$$\Delta E_H = E(Au + nH) - E[Au + (n-1)H] - E(H) \quad (8)$$

where $E(Au + nH)$ and $E[Au + (n-1)H]$ represent the total energy of the gold nanocluster with n and n-1 adsorbed H, respectively. $E(H)$ represents the total energy of one hydrogen atom. A negative value of ΔE_H suggests favorable absorption. To find the optimal adsorption site of hydrogen, initially we add hydrogen over the cluster's "pocket" site, where the inner Au_{13} core is not completely blocked by the protecting ligands. It is found that hydrogen will spontaneously bind to the inner Au_{13} core during the structure optimization. In addition, we tested hydrogen binding to the Au atoms of the protecting staple motifs. We find that they all have weaker binding energies. For the structures of more than one hydrogen adsorbed on the clusters, we tested different configurations, and the results of the most stable ones are shown.

The Gibbs free energies of hydrogen adsorption ΔG_H were obtained by

$$\Delta G_H = E(Au + H) - E(Au) - \frac{1}{2}E(H_2) + \Delta E_{ZPE} - T\Delta S_H \quad (9)$$

where $E(Au + H)$ represents the total energy of the gold nanocluster with one adsorbed H, $E(Au)$ represents the energy of the gold nanocluster without adsorbed H, and $E(H_2)$ represents the energy of one gas phase H_2 molecule. ΔE_{ZPE} is the difference in zero point energy between the adsorbed H and H in the gas phase H_2 molecule. ΔS_H is the difference in entropy between the adsorbed H and $\frac{1}{2}$ gas phase H_2 molecule.

For charged clusters such as $[PtAu_{24}(SR)_{18}]^{2-}$, the energetics was further checked with the Turbomole program (Version 6.5)[13] without the periodic boundary conditions at the same DFT-PBE level with the def2-TZVP basis sets[14] and a scalar-relativistic effective-core potential with 60 core electrons was used for Au[15]; the difference was found to be within 0.10 eV. The frontier orbitals were also generated from the Turbomole program.

In the end, we verified our results of $[Au_{25}(SR)_{18}]^q$ (q=-1,0,+1) clusters using more accurate hybrid functionals, namely Heyd–Scuseria–Ernzerhof (HSE)[16] in VASP and PBE0[17] in Turbomole. The calculated hydrogen adsorption energies with HSE in VASP and PBE0 in Turbomole are shown in Table 2.3 and Table 2.4, respectively. In addition, the HOMO-LUMO gaps calculated with these two hybrid functionals are listed in Table 2.5. As one can see, these results follow the same trend as the PBE results.

Table 2.3. Free-electron count (**n**) of $[Au_{25}(SR)_{18}]^{-}$, $[Au_{25}(SR)_{18}]^{0}$, and $[Au_{25}(SR)_{18}]^{+}$ and their sequential adsorption energy (eV) for hydrogen calculated with the hybrid functional HSE in VASP: first, ΔE_{H1}; second, ΔE_{H2}; third, ΔE_{H3}. R=CH_3.

Cluster	n	ΔE_{H1}	ΔE_{H2}	ΔE_{H3}
$[Au_{25}(SR)_{18}]^{-}$	8	-0.85	--	--
$[Au_{25}(SR)_{18}]^{0}$	7	-2.19	-0.84	--
$[Au_{25}(SR)_{18}]^{+}$	6	-1.72	-2.06	-1.11

Table 2.4. Free-electron count (**n**) of $[Au_{25}(SR)_{18}]^{-}$, $[Au_{25}(SR)_{18}]^{0}$, and $[Au_{25}(SR)_{18}]^{+}$ and their sequential adsorption energy (eV) for hydrogen calculated with the hybrid functional PBE0 in Turbomole: first, ΔE_{H1}; second, ΔE_{H2}; third, ΔE_{H3}. R=CH_3.

Cluster	n	ΔE_{H1}	ΔE_{H2}	ΔE_{H3}
$[Au_{25}(SR)_{18}]^{-}$	8	-0.89	--	--
$[Au_{25}(SR)_{18}]^{0}$	7	-2.03	-0.89	--
$[Au_{25}(SR)_{18}]^{+}$	6	-1.81	-2.16	-1.19

Table 2.5. HOMO-LUMO gaps of $[Au_{25}(SR)_{18}]^{-}$, $[Au_{25}H(SR)_{18}]^{0}$, and $[Au_{25}H_2(SR)_{18}]^{+}$ calculated with the hybrid functionals. R=CH_3.

Cluster	$[Au_{25}(SR)_{18}]^{-}$	$[Au_{25}H(SR)_{18}]^{0}$	$[Au_{25}H_2(SR)_{18}]^{+}$
HSE in VASP	1.73	1.77	1.80
PBE0 in Turbomole	2.48	2.49	2.46

2.5 Hydrogen adsorption on a Au_{22} nanocluster

DFT calculations with periodic boundary conditions (PBC) were performed by using the same computational methods as described in 2.4. The initial structure of the Au_{22} cluster is form the crystallographic information file provided by the experimental researchers.[18] Phenyl groups were replaced by hydrogens for the purpose of simplifying the calculations.

The frontier orbitals were also generated from the Turbomole program (Version 6.5)[13] as described in 2.4

Periodic DFT calculations at the same level of theory were performed for the Pt(111) surface. The Pt(111) surface was modeled with four layers of slabs in (4 × 4) lateral cells, and with 15 Å of vacuum along the *z*-direction. During the structural optimizations, the top two layers of the slab were allowed to relax together with the adsorbed H.

The differential hydrogen adsorption energy ΔE_H and the differential Gibbs free energy of hydrogen adsorption ΔG_H were calculated by the same methods as described in 2.1.

2.6 H_2 activation on TiO_2

Spin-polarized DFT calculations were performed by using the methods as described in 2.1. The on-site Coulomb interaction was included using the DFT+U method described by Dudarev et al.[19] with a Hubbard parameter of U=3.5 eV for the Ti atoms used in previous studies.[20-21] The rutile TiO_2(110), anatase TiO_2(101), and brookite TiO_2(210) surfaces were examined. They were modeled with three-layer-thick slabs with 2 × 2 super cells. A vacuum of 15 Å along the z-direction was employed. The topmost TiO_2 layers of the slabs together with the adsorbates were allowed to relax during the structure optimizations. The climbing-image nudged elastic band (CI-NEB) method implemented in VASP was used to determine the energy barriers.[22] The transition states were obtained by relaxing the force below 0.05 eV/Å.

Reference

1. Kresse, G.; Furthmüller, J., Efficient Iterative Schemes for Ab Initio Total-Energy Calculations Using a Plane-Wave Basis Set. *Phys. Rev. B* **1996**, *54*, 11169-11186.

2. Blöchl, P. E., Projector Augmented-Wave Method. *Phys. Rev. B* **1994**, *50*, 17953-17979.

3. Perdew, J. P.; Burke, K.; Ernzerhof, M., Generalized Gradient Approximation Made Simple. *Phys. Rev. Lett.* **1996**, *77*, 3865-3868.

4. Tang, W.; Sanville, E.; Henkelman, G., A Grid-Based Bader Analysis Algorithm without Lattice Bias. *J. Phys. Condens. Matter* **2009**, *21*, 084204.

5. Campaná, C.; Mussard, B.; Woo, T. K., Electrostatic Potential Derived Atomic Charges for Periodic Systems Using a Modified Error Functional. *J. Chem. Theory Comput.* **2009**, *5*, 2866-2878.

6. Rogal, J.; Reuter, K., Ab Initio Atomistic Thermodynamics for Surfaces: A Primer. **2006**.

7. Stull, D. R.; Prophet, H. *Janaf Thermochemical Tables*; DTIC Document: 1971.

8. Yoo, C.; Akella, J.; Cynn, H.; Nicol, M., Direct Elementary Reactions of Boron and Nitrogen at High Pressures and Temperatures. *Phys. Rev. B* **1997**, *56*, 140.

9. Grimme, S.; Antony, J.; Ehrlich, S.; Krieg, H., A Consistent and Accurate Ab Initio Parametrization of Density Functional Dispersion Correction (Dft-D) for the 94 Elements H-Pu. *J. Chem. Phys.* **2010**, *132*, 154104.

10. Linstrom, P. J.; Mallard, W., Nist Chemistry Webbook; Nist Standard Reference Database No. 69. **2001**.

11. Cramer, C. J., *Essentials of Computational Chemistry: Theories and Models*; John Wiley & Sons, 2013.

12. Grumelli, D.; Maza, F. L.; Kern, K.; Salvarezza, R. C.; Carro, P., Surface Structure and Chemistry of Alkanethiols on Au(100)-(1 × 1) Substrates. *J. Phys. Chem. C* **2016**, *120*, 291-296.

13. Ahlrichs, R.; Bär, M.; Häser, M.; Horn, H.; Kölmel, C., Electronic Structure Calculations on Workstation Computers: The Program System Turbomole. *Chem. Phys. Lett.* **1989**, *162*, 165-169.

14. Weigend, F.; Ahlrichs, R., Balanced Basis Sets of Split Valence, Triple Zeta Valence and Quadruple Zeta Valence Quality for H to Rn: Design and Assessment of Accuracy. *Phys. Chem. Chem. Phys.* **2005**, *7*, 3297-3305.

15. Andrae, D.; Haeussermann, U.; Dolg, M.; Stoll, H.; Preuss, H., Energy-Adjustedab Initio Pseudopotentials for the Second and Third Row Transition Elements. *Theor. Chim. Acta.* **1990**, *77*, 123-141.

16. Krukau, A. V.; Vydrov, O. A.; Izmaylov, A. F.; Scuseria, G. E., Influence of the Exchange Screening Parameter on the Performance of Screened Hybrid Functionals. *J Chem. Phys.* **2006**, *125*, 224106.

17. Adamo, C.; Barone, V., Toward Reliable Density Functional Methods without Adjustable Parameters: The Pbe0 Model. *J. Chem. Phys.* **1999**, *110*, 6158-6170.

18. Chen, J.; Zhang, Q.-F.; Bonaccorso, T. A.; Williard, P. G.; Wang, L.-S., Controlling Gold Nanoclusters by Diphospine Ligands. *J. Am. Chem. Soc.* **2013**, *136*, 92-95.

19. Dudarev, S.; Botton, G.; Savrasov, S.; Humphreys, C.; Sutton, A., Electron-Energy-Loss Spectra and the Structural Stability of Nickel Oxide: An Lsda+ U Study. *Phys. Rev. B* **1998**, *57*, 1505.

20. Aschauer, U.; Chen, J.; Selloni, A., Peroxide and Superoxide States of Adsorbed O_2 on Anatase Tio_2(101) with Subsurface Defects. *Phys. Chem. Chem. Phys.* **2010**, *12*, 12956-12960.

21. Aschauer, U.; Selloni, A., Hydrogen Interaction with the Anatase Tio_2(101) Surface. *Phys. Chem. Chem. Phys.* **2012**, *14*, 16595-16602.

22. Henkelman, G.; Uberuaga, B. P.; Jónsson, H., A Climbing Image Nudged Elastic Band Method for Finding Saddle Points and Minimum Energy Paths. *J. Chem. Phys.* **2000**, *113*, 9901-9904.

Chapter 3

CoP for Hydrogen Evolution: Implications from Hydrogen Adsorption

Abstract

Cobalt phosphide (CoP) is one of the most promising, earth-abundant electrocatalysts discovered to date for hydrogen evolution reaction (HER), yet the mechanism is not well understood. Since hydrogen adsorption is a key factor of HER activity, here we examine the adsorption of atomic hydrogen on the low-Miller-index surfaces of CoP, including (111), (110), (100), and (011), by using periodic density functional theory. From the calculated Gibbs free energy of adsorption, we predict that (111), (110), and (011) surfaces will have good catalytic activities for HER. From ab initio atomistic thermodynamics, we find that the stabilities of the surfaces at 1 atm H_2 and 300 K follow the trend of (111) > (100) ~ (110) >> (011). On the most stable (111) surface, both Co bridge sites and P top sites are found to be able to adsorb hydrogen with a close-to-zero free energy change and the synergy of proximal Co and P atoms on the surface results in a better HER activity. Our work provides important insights into CoP's excellent HER activity and a basis for further mechanistic understanding of HER on CoP and other transition-metal phosphides.

3.1 Introduction

Water splitting using renewable energy can provide a sustainable supply of fuel for future societies with hydrogen as a key energy carrier.[1] To date, platinum remains the most efficient electrocatalyst for hydrogen evolution reaction (HER). However, the low natural abundance and high cost of platinum hamper its wide use at the industrial scale. Thus, it is highly desirable to develop efficient, low-cost and earth-abundant electrocatalysts for HER and an enormous amount of research efforts have been devoted to it over the past decade.

Transition metal phosphides have emerged as alternative materials for HER electrocatalysts due to their high catalytic activities compared to other non-precious electrocatalysts and their relatively low costs compared to platinum. For example, phosphides of nickel,[2-13] cobalt,[14-33] iron,[34-38] copper,[39] molybdenum,[40-45] and tungsten[46] have been found to electrocatalytically generate hydrogen with low overpotentials at operationally relevant current densities. In particular, the cobalt phosphide system, which has been studied extensively, exhibits high HER activities and high stabilities under strongly acidic conditions across a diverse group of morphologies, characteristic grain sizes, support materials, and synthetic preparations. Among these systems, multi-faceted single-crystalline cobalt phosphide (CoP) nanoparticles deposited on a titanium foil electrode exhibit outstanding activities, with overpotentials of only −70 and −85 mV (at a loading density of ~ 2mg/cm^2) to produce cathodic current densities of −10 and −20 mA/cm^2, respectively.[14] Despite the exciting experimental results of CoP, the mechanism

of HER on CoP is not well understood, which is essential for further improving the activities and stabilities of the HER electrocatalysts.

Two types of possible pathways have been proposed for the mechanism of HER in acid media: the Volmer–Heyrovsky vs. the Volmer–Tafel mechanism. The Volmer reaction refers to the initial adsorption of protons from the acid solution to form adsorbed H ($H^+ + e^- \rightarrow H_{ad}$).[47] In the Volmer–Heyrovsky mechanism, a solvated proton from the water layer reacts with one adsorbed surface hydrogen to form H_2 ($H_{ad} + H^+ + e^- \rightarrow H_2$),[48] while in the Volmer–Tafel mechanism, two adsorbed surface hydrogens next to each other react to form an H_2 molecule ($H_{ad} + H_{ad} \rightarrow H_2$).[49] Thus, good HER electrocatalysts should be able to attract protons from the solution, while still can desorb H_2. Nørskov and coworkers have correlated experimental exchange currents with calculated hydrogen adsorption energies from density functional theory (DFT), where maximum activity is obtainable when Gibbs free energy of hydrogen adsorption (ΔG_H) is zero.[50] This is mainly because lower ΔG_H results in a very strong binding of the atomic hydrogen and hinders desorption of H_2, while higher ΔG_H prevents the binding of atomic hydrogen on the catalyst surfaces. Both of them will slow the reaction. Therefore, ΔG_H is considered as a good descriptor of HER activity, and good HER electrocatalysts are expected to have close-to-zero ΔG_H.

To understand HER on CoP in particular and to provide insights and guidelines for designing transition metal phosphide HER electrocatalysts in general, herein we have studied in detail the adsorption structures and energetics of atomic hydrogen on several low-Miller-index surfaces of CoP from first principles DFT. We use the calculated ΔG_H

to predict the HER activities of the surfaces. We further employ ab initio atomistic thermodynamics to determine the most stable and active surface of CoP at 1 atm H_2 pressure and 300K.

3.2 Results and discussion

We start with the bulk structure of CoP, followed by the clean surfaces including (111), (110), (100), and (011). We then examine and compare hydrogen adsorption on these surfaces.

3.2.1 Bulk CoP

Bulk CoP has a B31 or MnP-type structure, with a symmetry group of Pnma. In this type of structure, each metal atom is surrounded by six phosphorous atoms situated in a distorted octahedral configuration (Figure 3.1a), while each phosphorous atom is surrounded by six metal atoms forming a highly distorted triangular prism (Figure 3.1b). The experimental[51] and calculated lattice parameters of bulk CoP are listed in Table 3.1. One can see that the calculated values are in good agreement with the experimental values.

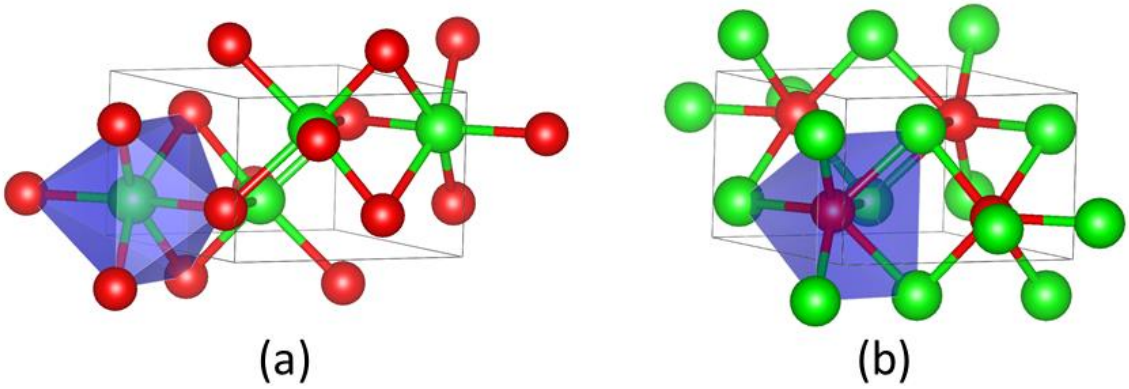

Figure 3.1. Bulk CoP: (a) Each Co atom is surrounded by six P atoms situated in a distorted octahedral configuration; (b) each P atom is surrounded by six Co atoms at the corners of a highly distorted triangular prism. Co, green; P, red.

Table 3.1. Comparison of experimental[51] and calculated lattice parameters of the bulk CoP.

Lattice Parameter	**a (Å)**	**b (Å)**	**c (Å)**
Experimental	5.077	3.281	5.587
Calculated	5.070	3.265	5.545

3.2.2 Clean Surfaces

Low Miller-index surfaces are usually considered first in surface science studies due to their higher stabilities than higher index surfaces. We consider here four such surfaces: (111), (110), (100), and (011). Figure 3.2 shows the structures of these clean CoP surfaces and Table 3.2 shows their calculated surface energies. One can see that the stabilities of the clean surfaces in vacuum follow the trend of (011) > (110) > (111) > (100). In general, surfaces with higher atom packing densities are expected to have higher stabilities. Here, we find that the surface packing densities of (011), (110), (111), and

(100) are 25 atom/nm^2, 24 atom/nm^2, 24 atom/nm^2, and 22 atom/nm^2, respectively, which indeed confirms the highest stability of the (011) surface and the lowest stability of the (100) surface. To learn the electronic structure of these surfaces, their electronic density of states (DOS) have been calculated. As shown in Figure 3.3, they are all metallic and have non-zero DOS at the Fermi level. Being the most stable one, the (011) surface also has the lowest DOS at the Fermi level.

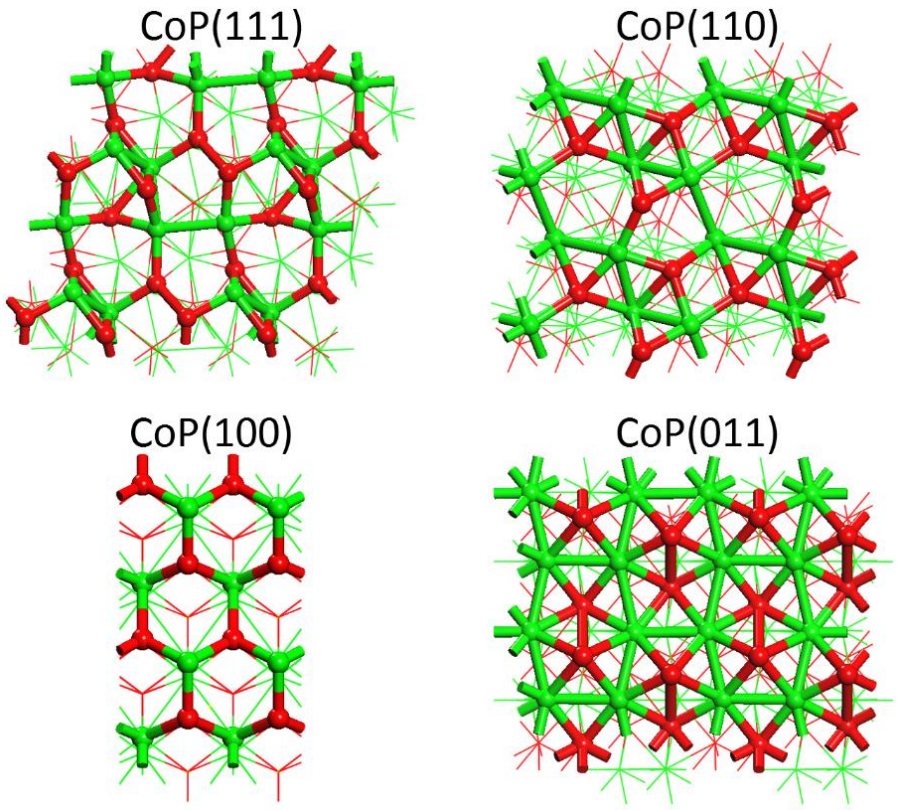

Figure 3.2. Top views of clean CoP surfaces. Co, green; P, red.

Table 3.2. Calculated surface energies of clean CoP surfaces.

	CoP(111)	**CoP(110)**	**CoP(100)**	**CoP(011)**
Surface Energy (meV/Å^2)	140.4	117.0	151.0	70.4

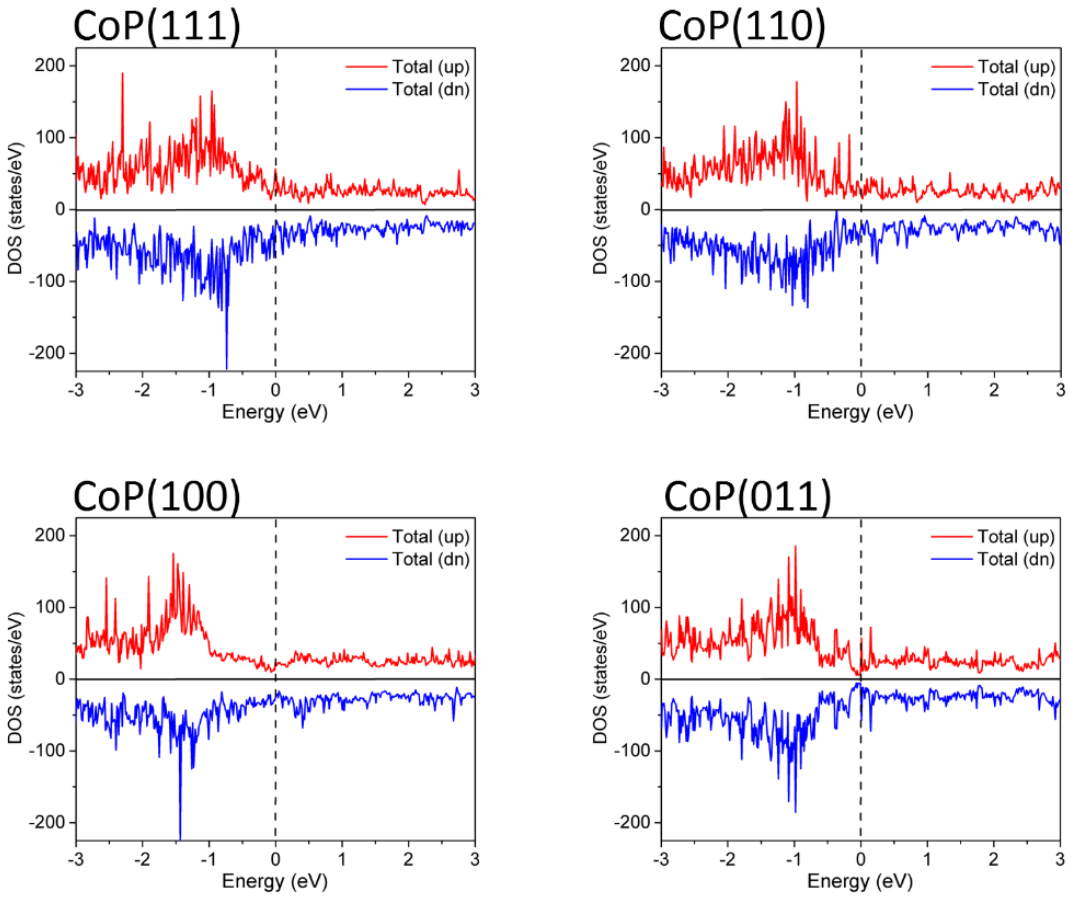

Figure 3.3. Spin-polarized total electronic density of states (DOS) of clean CoP surfaces. The Fermi level (dashed line) is set as zero.

3.2.3 Hydrogen Adsorption on the CoP(111) surface

As mentioned in the Introduction, ΔG_H is considered as a descriptor of HER activity, and good HER electrocatalysts should have close-to-zero ΔG_H . We next show the structures and ΔG_H of H adsorption on the four CoP surfaces. Figure 3.4 shows the calculated ΔG_H and ΔE_H for CoP(111) at different hydrogen coverages (here 100% coverage = 11 H-atom/nm^2). ΔG_H is more positive than ΔE_H because ΔS is negative when referencing to the H_2 state and the $T\Delta S$ term is roughly constant at -0.18 eV across the coverage range. One can see that ΔG_H is close-to-zero for 25% ~ 75% hydrogen coverage, indicating that the (111) surface will have good catalytic activity for HER at this coverage range. This supports the previous experimental finding that CoP nanostructures exposing predominately (111) surface have high HER activities.[23] The other interesting finding of H adsorption on CoP(111) is that ΔG_H shows a zigzag pattern with H coverage from 25% to 75%, which closely correlates with the adsorption sites, as discussed next.

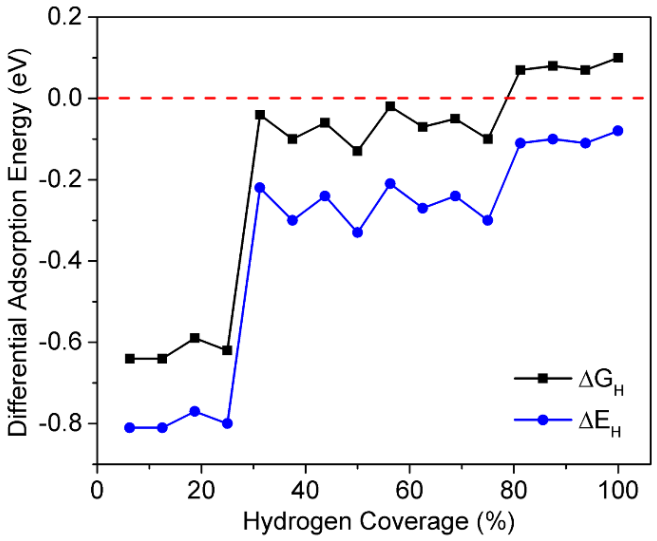

Figure 3.4. Differential adsorption energy (ΔE_H) and adsorption free energy (ΔG_H) as a function of hydrogen coverage on CoP(111).

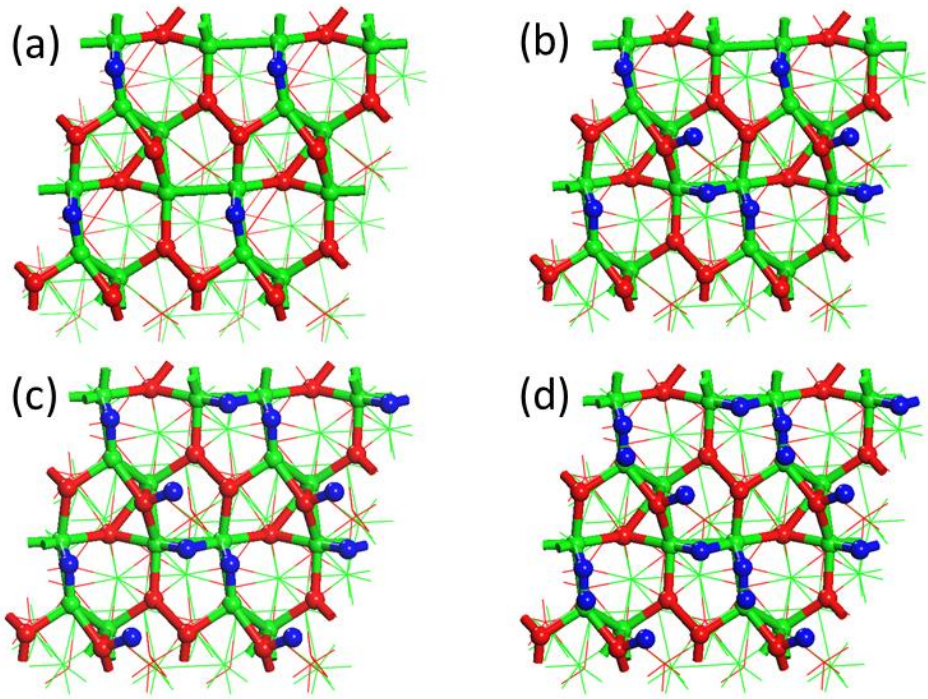

Figure 3.5. Optimized structures of CoP(111) at different H coverages: (a) 25%; (b) 50%; (c) 75%; (d) 100%. 100% coverage = 11 H-atom/nm^2. H, blue; Co, green; P, red.

Figure 3.5 shows the optimized structures of CoP(111) with different hydrogen coverages. We find four types of stable hydrogen adsorption sites on CoP(111). For the first 25% hydrogen atoms, they are strongly adsorbed at cobalt bridge sites. During 25% ~ 75% hydrogen coverage, there is an alternative adsorption between cobalt bridge sites and phosphorous top sites, leading to a zigzagged ΔG_H with a small fluctuation. More important, ΔG_H is close-to-zero during this range, so both cobalt bridge sites and phosphorous top sites could be the active sites for HER on the (111) surface. For the 75% to 100% coverage, the extra hydrogen atoms are adsorbed at cobalt top sites, leading to more than one hydrogen atoms on some cobalt atoms.

The "zigzag" pattern between 25% and 75% hydrogen coverage suggests a synergy between proximal cobalt and phosphorous sites in adsorbing H atoms, conductive to HER. To understand this behavior, Table 3.3 shows differential hydrogen adsorption energies (ΔE_H) at the phosphorous top site at 0% and 31% hydrogen coverages. One can see that when there is no hydrogen adsorbed on Co (0%), the interaction of H with P is weak but when there are hydrogens already adsorbed on Co (31%), the H-P interaction becomes stronger. In other words, hydrogen adsorption at Co facilitates hydrogen adsorption at P. We found that this is due to the weakening of the Co-P bond induced by hydrogen adsorption on Co, as evidenced by the increasing Co-P bond length, which results in less negative charge on P and stronger H-P covalent bonding. This synergy between Co and P for adsorbing H, as shown in Scheme 1, could be a key to CoP's high HER activity.

Table 3.3. Differential hydrogen adsorption energies (ΔE_H) at the P site, Co-P bond length ($r_{Co\text{-}P}$), and charges on P (P_{charge}) at 0% and 31% hydrogen coverages.

Hydrogen Coverage	**0%**	**31%**
ΔE_H (eV)	-0.10	-0.30
$r_{Co\text{-}P}$ (Å)	2.125	2.197
P_{charge} (|e|)	-0.257(Bader), -0.308(REPEAT)	-0.213(Bader), -0.266(REPEAT)

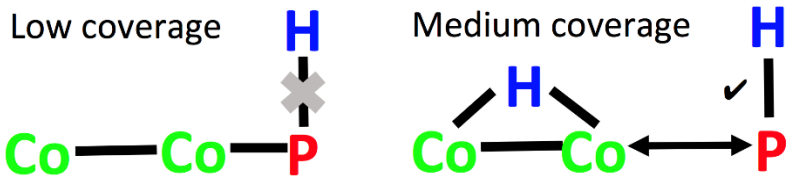

Scheme 1 The synergy between Co and P on CoP(111) in adsorbing H at medium coverage.

To evaluate the most stable coverage of H on CoP(111) at the experimental HER conditions (1 atm H_2 and 300 K), we used ab initio atomistic thermodynamics to determine $\Delta G^{ad}(T,p)$ as a function of hydrogen chemical potential ($\Delta\mu_H$) or pressure at T=300K. Figure 3.6 shows the calculated $\Delta G^{ad}(T,p)$ vs. $\Delta\mu_H$ relationship: each line represents a given H coverage. One can see that at extremely low hydrogen pressure, clean surface is the most stable, while at very high hydrogen pressure, 100% hydrogen coverage is the most stable (Figure 3.6a). At ambient pressures, Figure 3.6b shows that 75% hydrogen coverage is the most stable with ΔG^{ad} = -19.53 meV/Å^2 at 1 atm. At this coverage, both Co and P sites adsorb H.

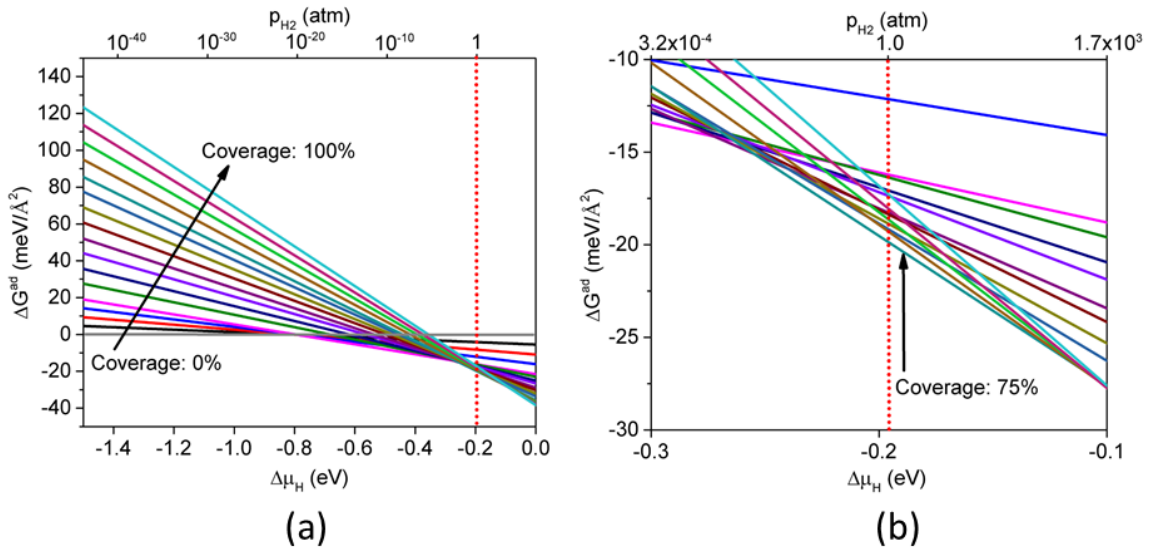

Figure 3.6. Gibbs free energy of adsorption (ΔG^{ad}) at 300K as a function of hydrogen chemical potential ($\Delta\mu_H$) or H_2 pressure for CoP(111) with different hydrogen coverages: (a) $\Delta\mu_H$ from -1.5 to 0 eV; (b) $\Delta\mu_H$ from -0.3 to -0.1 eV.

3.2.4 Hydrogen Adsorption on the CoP(110) surface.

Figure 3.7 shows ΔG_H and ΔE_H for the CoP(110) surface at different hydrogen coverages (100% coverage = 12 H-atom/nm^2). For a favorable adsorption ($\Delta G_H < 0$), we found that ΔG_H is close to zero when hydrogen coverage is in the range of 25% ~ 50% ($\Delta G_H \sim$ -0.10 eV). When hydrogen coverage is above 50%, ΔG_H is slightly positive but also close to zero. Figure 3.7 suggests that the CoP(110) surface can also be good for HER activity for a large range of H coverage. Figure 3.8 shows the optimized structures of CoP(110) at different hydrogen coverages. From 0% to 100% coverage, hydrogen atoms occupy cobalt bridge sites, phosphorous top sites, cobalt top sites, and another kind of cobalt top sites successively. Figure 3.9 plots ΔG^{ad} as a function of $\Delta\mu_H$ for CoP(110) at different hydrogen coverages. One can see that 50% hydrogen coverage is the most

stable at 1 atm and 300 K with ΔG^{ad} = -13.37 meV/Å^2. At this coverage, Figure 3.7 and 3.8 suggest that both the P and Co top sites are most likely to be active for HER.

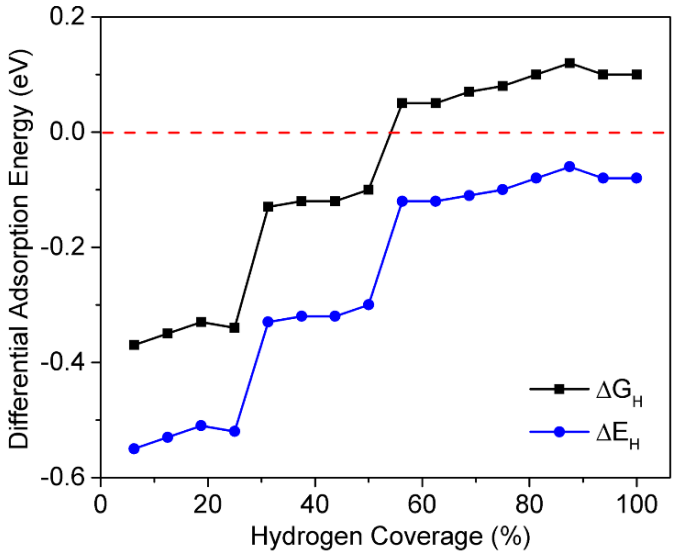

Figure 3.7. Differential adsorption energy (ΔE_H) and adsorption free energy (ΔG_H) as a function of hydrogen coverage on CoP(110).

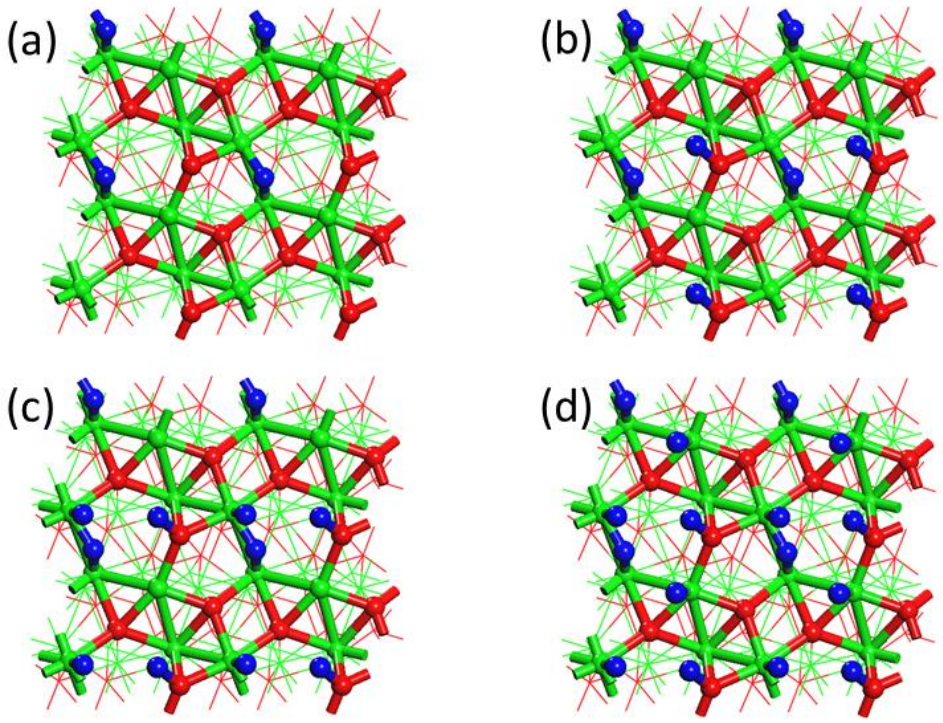

Figure 3.8. Optimized structures of CoP(110) at different H coverages: (a) 25%; (b) 50%; (c) 75%; (d) 100%. 100% coverage = 12 H-atom/nm^2. H, blue; Co, green; P, red.

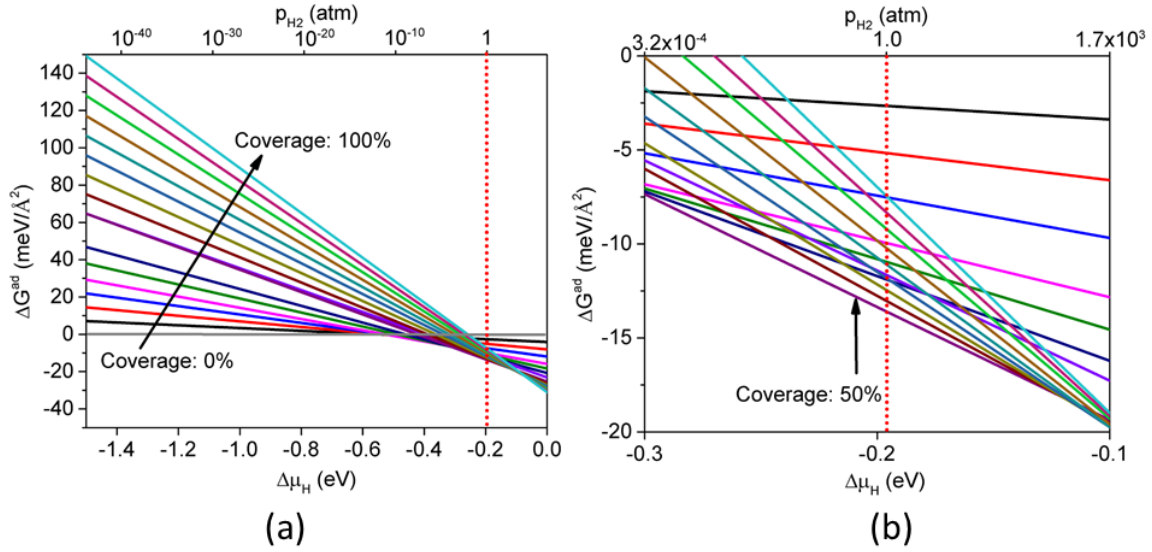

Figure 3.9. Gibbs free energy of adsorption (ΔG^{ad}) at 300K as a function of hydrogen chemical potential ($\Delta\mu_H$) or H_2 pressure for CoP(110) with different hydrogen coverages: (a) $\Delta\mu_H$ from -1.5 to 0 eV; (b) $\Delta\mu_H$ from -0.3 to -0.1 eV.

3.2.5 Hydrogen Adsorption on the CoP(100) surface

Figure 3.10a shows ΔG_H and ΔE_H for CoP(100) at different hydrogen coverages. One can see that there is no H coverage where $\Delta G_H \sim 0$, so CoP(100) is not likely to be good for HER. Figure 3.11 shows the optimized structures of CoP(100) with different hydrogen coverages. We find two types of stable hydrogen adsorption sites on CoP(100): cobalt bridge sites for the first 33% hydrogen atoms and cobalt top sites for the following 67% hydrogen atoms. Unlike (111) and (110) surfaces, only cobalt atoms adsorb hydrogen on the (100) surface. This might be the reason why we do not find $\Delta G_H \sim 0$ on CoP(100). Figure 3.10b plots ΔG^{ad} as a function of $\Delta\mu_H$ for CoP(100) and we find that 33% hydrogen coverage is the most stable at 1 atm and 300 K with ΔG^{ad} = -13.56 meV/Å^2.

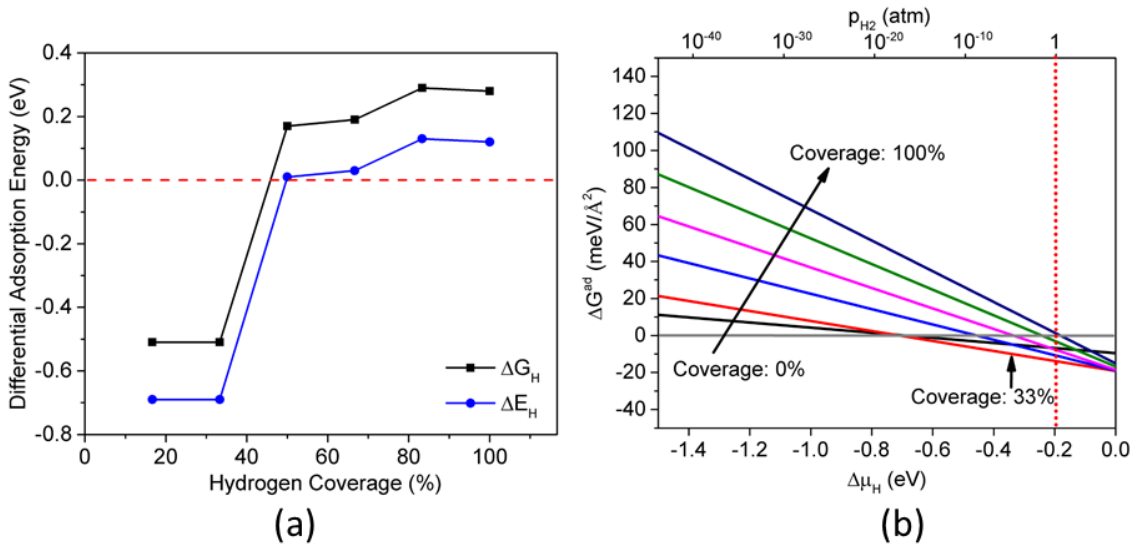

Figure 3.10. (a) Differential adsorption energy (ΔE_H) and adsorption free energy (ΔG_H) as a function of hydrogen coverage on CoP(100). (b) Plots of the calculated Gibbs free energy of adsorption (ΔG^{ad}) at 300K as a function of hydrogen chemical potential ($\Delta\mu_H$) for CoP (100) surface with different hydrogen coverages.

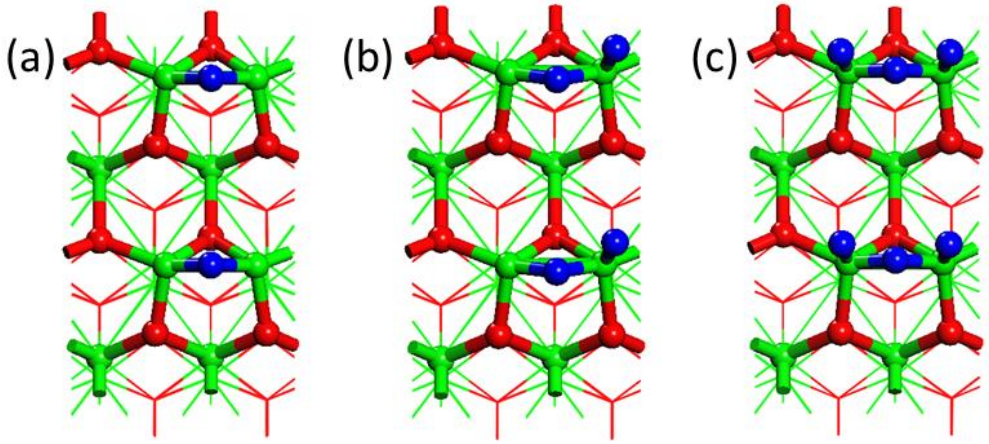

Figure 3.11. Optimized structures of CoP(100) at different H coverages: (a) 33%; (b) 67%; (c) 100%. 100% coverage = 8 H-atom/nm^2. H, blue; Co, green; P, red.

3.2.6 Hydrogen Adsorption on the CoP(011) surface

Figure 3.12a shows ΔG_H and ΔE_H for CoP(011) at different hydrogen coverages. One can see that the adsorption of H on CoP(011) is in general much weaker than on the other three surfaces. On the other hand, this leads to a quite large range of H coverages from 0 to 50% where $\Delta G_H \sim 0$, indicating that CoP(011) may have good activity for HER. Figure 3.13 shows the optimized structures of CoP(011) surface at different hydrogen coverages. We find two types of stable hydrogen adsorption sites on CoP(011). The first 50% coverage of hydrogen atoms prefer phosphorous top sites with $\Delta G_H \sim 0$, so phosphorous top sites could be the active sites for HER on the (011) surface. This is in agreement with a recent study.[33] The last 50% coverage of hydrogen atoms occupy cobalt bridge sites. Figure 3.12b plots ΔG^{ad} as a function of $\Delta\mu_H$ for CoP(011) at different hydrogen coverages. One can see that 25% hydrogen coverage is the most stable phase at 1 atm and 300 K with $\Delta G^{ad} \sim 0$ meV/Å^2, while the clean surface is only slightly higher in energy. This again agrees with the fact that the adsorption of H on CoP(011) is rather weak.

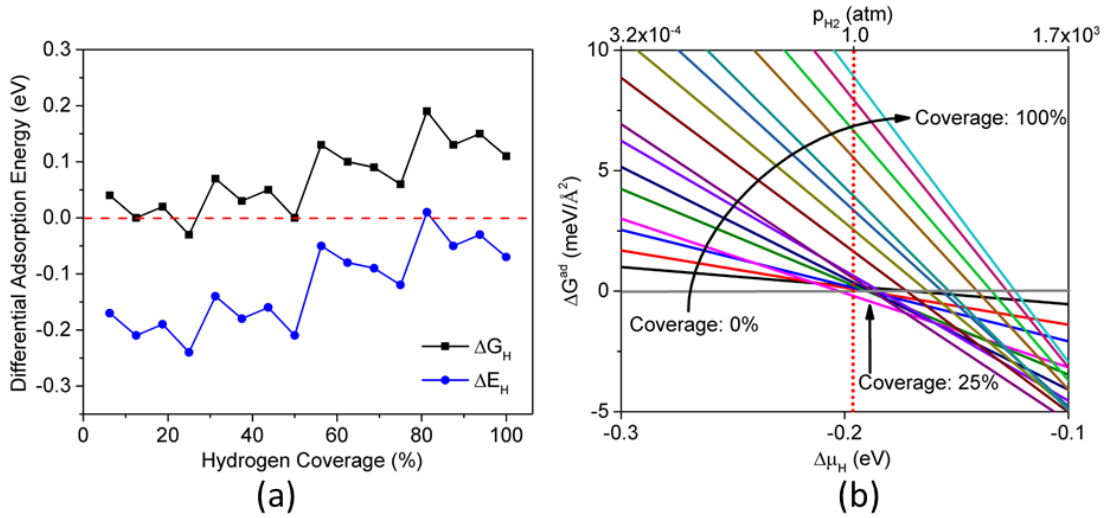

Figure 3.12. (a) Differential adsorption energy (ΔE_H) and adsorption free energy (ΔG_H) as a function of hydrogen coverage on CoP(011). (b) Gibbs free energy of adsorption (ΔG^{ad}) at 300K as a function of hydrogen chemical potential ($\Delta\mu_H$) or H_2 pressure for CoP(011) with different hydrogen coverages.

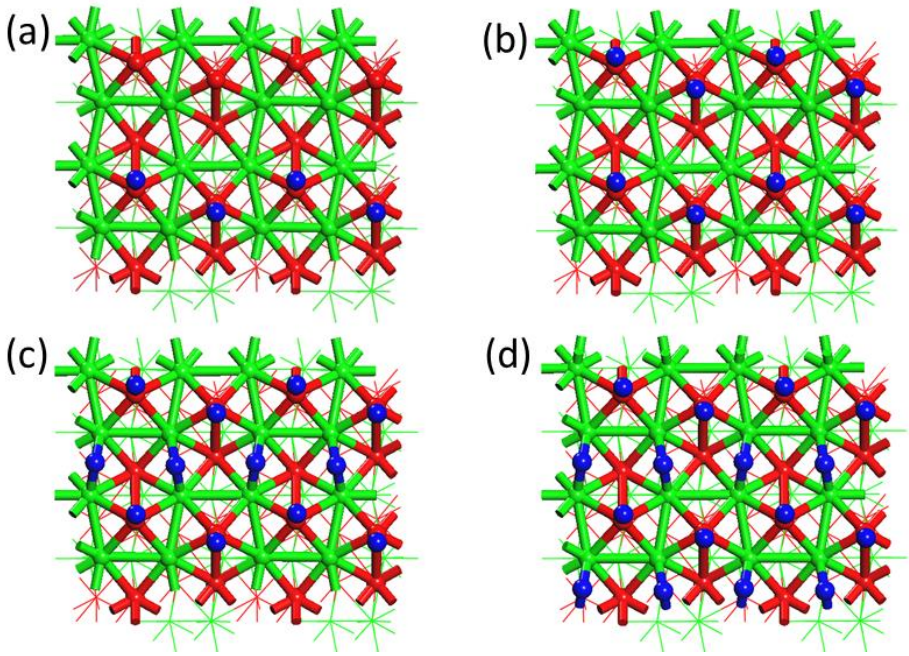

Figure 3.13. Optimized structures of CoP(011) at different H coverages: (a) 25%; (b) 50%; (c) 75%; (d) 100%. 100% coverage = 12 H-atom/nm^2. H, blue; Co, green; P, red.

3.2.7 Comparison of (111), (110), (100), and (011) surfaces of CoP

Now that we have studied hydrogen adsorption on the four low Miller-index surfaces of CoP, we can compare them together in terms of stability and HER activity. Using $\Delta G_H \sim 0$ as a criterion, we predict that (111), (110), and (011) surfaces of CoP should have good catalytic activities for HER, while (100) should not. Taking into account ab initio atomistic thermodynamics, Table 3.4 shows the comparison of ΔG^{ad} at 1 atm H_2 and 300K for the most stable coverage of each surface. One can see that CoP(111) has the most negative ΔG^{ad} followed by (100) and (110), while (011) has a close-to-zero ΔG^{ad}. In other words, at the reaction conditions, the stability trend is (111) > (100) ~ (110) >> (011). From this perspective, we think that the CoP(111) surface is the most promising facet for high-activity HER.

Table 3.4. Hydrogen adsorption free energies (ΔG^{ad}) at 1atm and 300K of the most stable coverage for each CoP surface.

	CoP(111)	**CoP(110)**	**CoP(100)**	**CoP(011)**
ΔG^{ad} **(meV/Å²)**	-19.53	-13.37	-13.56	-0.08

Our present DFT study of the adsorption of atomic hydrogen on the low-Miller-index surfaces of CoP, including (111), (110), (100), and (011), presents several interesting implications. First, CoP nanostructures that expose different crystal facets would be expected to exhibit different activities for HER catalysis. From our calculated ΔG_H, we predict that (111), (110), and (011) surfaces of CoP will have good catalytic activities for

HER. So experimental researchers could prepare highly branched nanostructures that expose a high density of these surfaces. Second, both Co and P on the surfaces play important roles in catalyzing HER. Particularly, on (111) surface, both Co bridge sites and P top sites are found to be able to adsorb hydrogen with a close-to-zero free energy change, indicating that the synergy of proximal Co and P atoms on the surface can result in a better HER activity. Third, hydrogen coverage, pressure, and temperature all have effects on the stabilities of the surfaces. We find that the stabilities of the clean surfaces in vacuum are different from the stabilities at 1 atm H_2 and 300K. The stabilities of the clean surfaces in vacuum follow the trend of (011) > (110) > (111) > (100), while the stabilities of the surfaces at 1 atm H_2 and 300K follow the trend of (111) > (100) ~ (110) >> (011). This suggests that if one purposefully prepares the catalyst with the (111) facet, then the catalyst is likely to have a longer lifetime given its high stability during the reaction conditions, while the (011) surface might transform to other more stable surfaces under reaction conditions. Last but not the least, 75% coverage of hydrogen on CoP(111) would be very helpful for the Volmer-Tafel mechanism, as higher surface coverage would be good for two adsorbed hydrogens next to each other to react and form an H_2 molecule. Likewise, the 25% coverage of optimal adsorption on CoP(011) would likely favor the Volmer-Heyrovsky mechanism, in which a solvated proton from the water layer reacts with one adsorbed surface hydrogen to form H_2. This will be a prelude to our full kinetic study of HER on CoP surfaces in the future, as we recently did for HER on MoS_2.[52]

3.3 Conclusions

To shed light on the activity of hydrogen evolution reaction (HER) on CoP, we have studied the adsorption of atomic hydrogen on the low-Miller-index surfaces of CoP, including (111), (110), (100), and (011), by using periodic DFT. From the calculated ΔG_H, we predict that (111), (110), and (011) surfaces will have good catalytic activities for HER. From ab initio atomistic thermodynamics, we find that the stabilities of the surfaces at 1 atm H_2 and 300K follow the trend of (111) > (100) ~ (110) >> (011). So combining ΔG_H and stability, we conclude that the (111) surface of CoP is the most promising facet for high and long-lived HER activity. The key feature of hydrogen adsorption on the (111) is that both Co bridge sites and P top sites are able to adsorb hydrogen with a close-to-zero free energy change and that there is a synergy of proximal Co and P atoms on the CoP(111) surface in adsorbing hydrogen. These insights open a door for further mechanistic understanding of HER on CoP and other phosphides.

References

1. Lubitz, W.; Tumas, W., Hydrogen: An Overview. *Chem. Rev.* **2007**, *107*, 3900-3903.

2. Liu, P.; Rodriguez, J. A., Catalysts for Hydrogen Evolution from the [NiFe] Hydrogenase to the $Ni_2P(001)$ Surface: The Importance of Ensemble Effect. *J. Am. Chem. Soc.* **2005**, *127*, 14871-14878.

3. Popczun, E. J.; McKone, J. R.; Read, C. G.; Biacchi, A. J.; Wiltrout, A. M.; Lewis, N. S.; Schaak, R. E., Nanostructured Nickel Phosphide as an Electrocatalyst for the Hydrogen Evolution Reaction. *J. Am. Chem. Soc.* **2013**, *135*, 9267-9270.

4. Feng, L.; Vrubel, H.; Bensimon, M.; Hu, X., Easily-Prepared Dinickel Phosphide (Ni_2P) Nanoparticles as an Efficient and Robust Electrocatalyst for Hydrogen Evolution. *Phys. Chem. Chem. Phys.* **2014**, *16*, 5917-5921.

5. Huang, Z.; Chen, Z.; Chen, Z.; Lv, C.; Meng, H.; Zhang, C., $Ni_{12}p_5$ Nanoparticles as an Efficient Catalyst for Hydrogen Generation Via Electrolysis and Photoelectrolysis. *ACS Nano* **2014**, *8*, 8121-8129.

6. Laursen, A.; Patraju, K.; Whitaker, M.; Retuerto, M.; Sarkar, T.; Yao, N.; Ramanujachary, K.; Greenblatt, M.; Dismukes, G., Nanocrystalline Ni_5p_4: A Hydrogen Evolution Electrocatalyst of Exceptional Efficiency in Both Alkaline and Acidic Media. *Energy & Environ. Sci.* **2015**, *8*, 1027-1034.

7. Wang, X.; Kolen'ko, Y. V.; Bao, X. Q.; Kovnir, K.; Liu, L., One-Step Synthesis of Self-Supported Nickel Phosphide Nanosheet Array Cathodes for Efficient Electrocatalytic Hydrogen Generation. *Angew. Chem. Int. Ed.* **2015**, *54*, 8188-8192.

8. Pan, Y.; Yang, N.; Chen, Y.; Lin, Y.; Li, Y.; Liu, Y.; Liu, C., Nickel Phosphide Nanoparticles-Nitrogen-Doped Graphene Hybrid as an Efficient Catalyst for Enhanced Hydrogen Evolution Activity. *J. Power Sources* **2015**, *297*, 45-52.

9. Cai, Z.; Song, X.; Wang, Y.; Chen, X., Electrodeposition-Assisted Synthesis of Ni_2P Nanosheets on 3d Graphene/Ni Foam Electrode and Its Performance for Electrocatalytic Hydrogen Production. *ChemElectroChem* **2015**, *2*, 1665-1671.

10. Li, J.; Li, J.; Zhou, X.; Xia, Z.; Gao, W.; Ma, Y.; Qu, Y., Highly Efficient and Robust Nickel Phosphides as Bifunctional Electrocatalysts for Overall Water-Splitting. *ACS Appl. Mater. Interfaces* **2016**, *8*, 10826-10834.

11. Wang, X.; Li, W.; Xiong, D.; Petrovykh, D. Y.; Liu, L., Bifunctional Nickel Phosphide Nanocatalysts Supported on Carbon Fiber Paper for Highly Efficient and Stable Overall Water Splitting. *Adv. Funct. Mater.* **2016**.

12. Jiang, N.; You, B.; Sheng, M.; Sun, Y., Bifunctionality and Mechanism of Electrodeposited Nickel-Phosphorous Films for Efficient Overall Water Splitting. *ChemCatChem* **2016**, *8*, 106-112.

13. You, B.; Jiang, N.; Sheng, M.; Bhushan, M. W.; Sun, Y., Hierarchically Porous Urchin-Like Ni_2P Superstructures Supported on Nickel Foam as Efficient Bifunctional Electrocatalysts for Overall Water Splitting. *ACS Catal.* **2016**, *6*, 714-721.

14. Popczun, E. J.; Read, C. G.; Roske, C. W.; Lewis, N. S.; Schaak, R. E., Highly Active Electrocatalysis of the Hydrogen Evolution Reaction by Cobalt Phosphide Nanoparticles. *Angew. Chem. Int. Ed.* **2014**, *53*, 5427-5430.

15. Tian, J.; Liu, Q.; Asiri, A. M.; Sun, X., Self-Supported Nanoporous Cobalt Phosphide Nanowire Arrays: An Efficient 3d Hydrogen-Evolving Cathode over the Wide Range of Ph 0-14. *J. Am. Chem. Soc.* **2014**, *136*, 7587-7590.

16. Jiang, P.; Liu, Q.; Ge, C.; Cui, W.; Pu, Z.; Asiri, A. M.; Sun, X., Cop Nanostructures with Different Morphologies: Synthesis, Characterization and a Study of Their Electrocatalytic Performance toward the Hydrogen Evolution Reaction. *J. Mater. Chem. A* **2014**, *2*, 14634-14640.

17. Liu, Q.; Tian, J.; Cui, W.; Jiang, P.; Cheng, N.; Asiri, A. M.; Sun, X., Carbon Nanotubes Decorated with CoP Nanocrystals: A Highly Active Non-Noble-Metal Nanohybrid Electrocatalyst for Hydrogen Evolution. *Angew. Chem. Int. Ed.* **2014**, *53*, 6710-6704.

18. Pu, Z.; Liu, Q.; Jiang, P.; Asiri, A. M.; Obaid, A. Y.; Sun, X., Cop Nanosheet Arrays Supported on a Ti Plate: An Efficient Cathode for Electrochemical Hydrogen Evolution. *Chem. Mater.* **2014**, *26*, 4326-4329.

19. Saadi, F. H.; Carim, A. I.; Verlage, E.; Hemminger, J. C.; Lewis, N. S.; Soriaga, M. P., CoP as an Acid-Stable Active Electrocatalyst for the Hydrogen-Evolution Reaction: Electrochemical Synthesis, Interfacial Characterization and Performance Evaluation. *J. Phys. Chem. C* **2014**, *118*, 29294-29300.

20. Li, Q.; Xing, Z.; Asiri, A. M.; Jiang, P.; Sun, X., Cobalt Phosphide Nanoparticles Film Growth on Carbon Cloth: A High-Performance Cathode for Electrochemical Hydrogen Evolution. *Int. J. Hydrogen Energy* **2014**, *39*, 16806-16811.

21. Du, H.; Liu, Q.; Cheng, N.; Asiri, A. M.; Sun, X.; Li, C. M., Template-Assisted Synthesis of CoP Nanotubes to Efficiently Catalyze Hydrogen-Evolving Reaction. *J. Mater. Chem. A* **2014**, *2*, 14812-14816.

22. Huang, Z.; Chen, Z.; Chen, Z.; Lv, C.; Humphrey, M. G.; Zhang, C., Cobalt Phosphide Nanorods as an Efficient Electrocatalyst for the Hydrogen Evolution Reaction. *Nano Energy* **2014**, *9*, 373-382.

23. Popczun, E. J.; Roske, C. W.; Read, C. G.; Crompton, J. C.; McEnaney, J. M.; Callejas, J. F.; Lewis, N. S.; Schaak, R. E., Highly Branched Cobalt Phosphide Nanostructures for Hydrogen-Evolution Electrocatalysis. *J. Mater. Chem. A* **2015**, *3*, 5420-5425.

24. Callejas, J. F.; Read, C. G.; Popczun, E. J.; McEnaney, J. M.; Schaak, R. E., Nanostructured Co_2p Electrocatalyst for the Hydrogen Evolution Reaction and Direct Comparison with Morphologically Equivalent Cop. *Chem. Mater.* **2015**, *27*, 3769-3774.

25. Li, L.; Li, X.; Ai, L.; Jiang, J., Mof-Derived Nanostructured Cobalt Phosphide Assemblies for Efficient Hydrogen Evolution Reaction. *RSC Adv.* **2015**, *5*, 90265-90271.

26. Vigil, J. A.; Lambert, T. N., Nanostructured Cobalt Phosphide-Based Films as Bifunctional Electrocatalysts for Overall Water Splitting. *RSC Adv.* **2015**, *5*, 105814-105819.

27. Jiang, N.; You, B.; Sheng, M.; Sun, Y., Electrodeposited Cobalt-Phosphorous-Derived Films as Competent Bifunctional Catalysts for Overall Water Splitting. *Angew. Chem. Int. Ed.* **2015**, *54*, 6251-4.

28. You, B.; Jiang, N.; Sheng, M.; Gul, S.; Yano, J.; Sun, Y., High-Performance Overall Water Splitting Electrocatalysts Derived from Cobalt-Based Metal–Organic Frameworks. *Chem. Mater.* **2015**, *27*, 7636-7642.

29. Liu, M.; Li, J., Cobalt Phosphide Hollow Polyhedron as Efficient Bifunctional Electrocatalysts for the Evolution Reaction of Hydrogen and Oxygen. *ACS Appl. Mater. Interfaces* **2016**, *8*, 2158-2165.

30. Pan, Y.; Lin, Y.; Chen, Y.; Liu, Y.; Liu, C., Cobalt Phosphide-Based Electrocatalysts: Synthesis and Phase Catalytic Activity Comparison for Hydrogen Evolution. *J. Mater. Chem. A* **2016**, *4*, 4745-4754.

31. Huang, H.; Yu, C.; Yang, J.; Zhao, C.; Han, X.; Liu, Z.; Qiu, J., Strongly Coupled Architectures of Cobalt Phosphide Nanoparticles Assembled on Graphene as Bifunctional Electrocatalysts for Water Splitting. *ChemElectroChem* **2016**, *3*, 719-725.

32. Tan, Y.; Wang, H.; Liu, P.; Cheng, C.; Zhu, F.; Hirata, A.; Chen, M., 3d Nanoporous Metal Phosphides toward High-Efficiency Electrochemical Hydrogen Production. *Adv. Mater.* **2016**, *28*, 2951-2955.

33. Ha, D.-H.; Han, B.; Risch, M.; Giordano, L.; Yao, K. P. C.; Karayaylali, P.; Shao-Horn, Y., Activity and Stability of Cobalt Phosphides for Hydrogen Evolution Upon Water Splitting. *Nano Energy* **2016**.

34. Callejas, J. F.; McEnaney, J. M.; Read, C. G.; Crompton, J. C.; Biacchi, A. J.; Popczun, E. J.; Gordon, T. R.; Lewis, N. S.; Schaak, R. E., Electrocatalytic and Photocatalytic Hydrogen Production from Acidic and Neutral-Ph Aqueous Solutions Using Iron Phosphide Nanoparticles. *ACS nano* **2014**, *8*, 11101-11107.

35. Jiang, P.; Liu, Q.; Liang, Y.; Tian, J.; Asiri, A. M.; Sun, X., A Cost-Effective 3d Hydrogen Evolution Cathode with High Catalytic Activity: Fep Nanowire Array as the Active Phase. *Angew. Chem. Int. Ed.* **2014**, *53*, 12855-12859.

36. Yan, Y.; Xia, B. Y.; Ge, X.; Liu, Z.; Fisher, A.; Wang, X., A Flexible Electrode Based on Iron Phosphide Nanotubes for Overall Water Splitting. *Chemistry* **2015**, *21*, 18062-18067.

37. Lv, C.; Peng, Z.; Zhao, Y.; Huang, Z.; Zhang, C., The Hierarchical Nanowires Array of Iron Phosphide Integrated on a Carbon Fiber Paper as an Effective Electrocatalyst for Hydrogen Generation. *J. Mater. Chem. A* **2016**, *4*, 1454-1460.

38. Son, C. Y.; Kwak, I. H.; Lim, Y. R.; Park, J., Fep and FeP_2 Nanowires for Efficient Electrocatalytic Hydrogen Evolution Reaction. *Chem. Commun.* **2016**, *52*, 2819-2822.

39. Tian, J.; Liu, Q.; Cheng, N.; Asiri, A. M.; Sun, X., Self-Supported Cu_3p Nanowire Arrays as an Integrated High-Performance Three-Dimensional Cathode for Generating Hydrogen from Water. *Angew. Chem. Int. Ed.* **2014**, *53*, 9577-9581.

40. Xiao, P.; Sk, M. A.; Thia, L.; Ge, X.; Lim, R. J.; Wang, J.-Y.; Lim, K. H.; Wang, X., Molybdenum Phosphide as an Efficient Electrocatalyst for the Hydrogen Evolution Reaction. *Energy Environ. Sci.* **2014**, *7*, 2624-2629.

41. McEnaney, J. M.; Crompton, J. C.; Callejas, J. F.; Popczun, E. J.; Biacchi, A. J.; Lewis, N. S.; Schaak, R. E., Amorphous Molybdenum Phosphide Nanoparticles for Electrocatalytic Hydrogen Evolution. *Chem. Mater.* **2014**, *26*, 4826-4831.

42. Xing, Z.; Liu, Q.; Asiri, A. M.; Sun, X., Closely Interconnected Network of Molybdenum Phosphide Nanoparticles: A Highly Efficient Electrocatalyst for Generating Hydrogen from Water. *Adv. Mater.* **2014**, *26*, 5702-5707.

43. Deng, C.; Ding, F.; Li, X.; Guo, Y.; Ni, W.; Yan, H.; Sun, K.; Yan, Y.-M., Templated-Preparation of a Three-Dimensional Molybdenum Phosphide Sponge as a High Performance Electrode for Hydrogen Evolution. *J. Mater. Chem. A* **2016**, *4*, 59-66.

44. Yao, Z.; Su, Y.; Lu, C.; Yang, C.; Xu, Z.; Zhu, J.; Zhuang, X.; Zhang, F., Template-Directed Approach to Two-Dimensional Molybdenum Phosphide–Carbon Nanocomposites with High Catalytic Activities in the Hydrogen Evolution Reaction. *New J. Chem.* **2016**, *40*, 6015-6021.

45. Pu, Z.; Wei, S.; Chen, Z.; Mu, S., Flexible Molybdenum Phosphide Nanosheet Array Electrodes for Hydrogen Evolution Reaction in a Wide Ph Range. *Appl. Catal. B: Environ.* **2016**, *196*, 193-198.

46. McEnaney, J. M.; Crompton, J. C.; Callejas, J. F.; Popczun, E. J.; Read, C. G.; Lewis, N. S.; Schaak, R. E., Electrocatalytic Hydrogen Evolution Using Amorphous Tungsten Phosphide Nanoparticles. *Chem. Commun.* **2014**, *50*, 11026-11028.

47. Erdey-Gruz, T.; Volmer, M., Zur Theorie Der Wasserstoffüberspannung. *Z. Phys. Chem. A* **1930**, *150*, 203.

48. Heyrovský, J., A Theory of Overpotential. *Recl. Trav. Chim. Pays-Bas* **1927**, *46*, 582-585.

49. Tafel, J., Über Die Polarisation Bei Kathodischer Wasserstoffentwicklung. *Z. phys. Chem* **1905**, *50*, 641.

50. Nørskov, J. K.; Bligaard, T.; Logadottir, A.; Kitchin, J. R.; Chen, J. G.; Pandelov, S.; Stimming, U., Trends in the Exchange Current for Hydrogen Evolution. *J. Electrochem. Soc.* **2005**, *152*, J23-J26.

51. Rundqvist, S., Phosphides of the B31 (MnP) Structure Type. *Acta Chem. Scand.* **1962**, *16*, 287-292.

52. Tang, Q.; Jiang, D. E., Mechanism of Hydrogen Evolution Reaction on 1T-MoS_2 from First Principles. *ACS Catal.* **2016**, *6*, 4953-4961.

Chapter 4

Interface Engineering of Earth-Abundant Transition Metals by Boron Nitride for Selective Electroreduction of CO_2

Abstract

Two-dimensional atomically thin hexagonal boron nitride (h-BN) monolayer has attracted considerable research interest. Given the tremendous progress in the synthesis of h-BN monolayers on transition metals and their potential as electrocatalysts, we investigate the electrocatalytic activities of h-BN/Ni, h-BN/Co, and h-BN/Cu interfaces for CO_2 reduction by first-principles density functional theory. We find that with the h-BN monolayer on the metal, electrons transfer from the metal to the interface and accumulate under the B atoms. By calculating the binding energies of three key intermediates (H, HCOO, and COOH) for hydrogen evolution and CO_2 reduction, we find that H binding on the metal can be significantly weakened by the h-BN monolayer, preventing the hydrogen-evolution reaction (HER). But the binding strength of HCOO is strong on both the metal and h-BN/metal, especially for Ni and Co, promoting the CO_2 reduction channel. Based on the free-energy diagrams, we predict that h-BN/Ni and h-BN/Co can be very good electrocatalysts for CO_2 reduction to HCOOH while the competitive HER channel is filtered out by the surface h-BN monolayer. Our study opens a new way for selective electroreduction of CO_2 via the interface engineering of the h-BN/metal system.

4.1 Introduction

Hexagonal boron nitride (h-BN) has been employed in a variety of applications due to its excellent properties like high thermal conductivity, chemical stability, refractory nature, high electrical resistivity, and lubricity.[1-4] Like graphene, h-BN monolayer as a two-dimensional atomically thin material has recently attracted considerable attention.[5-9] The structural similarity of graphene and h-BN makes h-BN monolayer a promising substrate for graphene electronics.[10-14] Furthermore, h-BN monolayers have been widely used as templates to support, decouple, and assemble individual adsorbates or nanostructures.[15-19]

Monolayers of h-BN can be successfully grown on various transition metals by chemical vapor deposition (CVD) and subsequent chemical reactions.[20-25] Depending on the lattice mismatch and interaction strength between h-BN and the metal, a variety of morphologies have been achieved such as uniform commensurate layer on Ni(111),[26-27] Moiré pattern on Pd(111),[28] strongly corrugated nanomesh topology on Rh(111),[15] and one-dimensional superstructure on Fe(110).[29] Usually, a large lattice mismatch combined with strong h-BN/metal interaction causes considerable geometric corrugations. Despite the extensive experimental studies on the synthesis of h-BN monolayers on transition metals, the application of such interface materials is still in its infancy but shows great promise.[30-35] For example, Taketsugu and coworkers reported the oxygen reduction reaction (ORR) activity of h-BN monolayer supported on Au, from a combined experimental and theoretical effort.[31] Recently, Mao, et al. investigated the chemisorption of O_2 molecule on h-BN monolayers supported on Ni, Co, and Cu from first-principles calculations.[35]

Previous studies show that commensurate h-BN monolayer can be formed only on Ni(111), Co(0001), and Cu(111) which have the smallest lattice mismatch (< 2.3%) with h-BN.[36-37] Ni, Co, and Cu are all earth-abundant transition metals, and numerous researchers have studied the electrochemical reduction of CO_2 at these metal electrodes.[38-42] It is found that Ni and Co do not possess strong activity in CO_2 reduction. On the contrary, they mainly produce H_2. Cu is unique in its ability to produce hydrocarbon fuels from CO_2 reduction at high overpotentials. At low overpotentials, H_2 is the main product instead.[43] Since CO_2 reduction competes with hydrogen evolution reaction (HER) at all negative potentials, a key criterion for selective catalysts in CO_2 reduction is the avoidance of HER in the presence of CO_2.[44]

The tremendous progress in the synthesis of h-BN monolayers on transition metals and their potential as electrocatalysts to overcome BN's poor electronic conductivity prompted us to investigate the activities of h-BN/Ni, h-BN/Co, and h-BN/Cu toward electrochemical CO_2 reduction by first-principles density functional theory (DFT). We first examine the geometry and electronic structures of h-BN/Ni, h-BN/Co, and h-BN/Cu. Then, we compute the binding energies of key intermediates during HER and CO_2 reduction on the three different systems: (a) unsupported h-BN monolayer; (b) the metal surfaces, Ni(111), Co(0001), and Cu(111); (c) the h-BN/metal composite. Next, we employ the computational hydrogen electrode model[45] to evaluate the free energy diagrams for the hydrogen evolution and CO_2 reduction reactions as well as their competition on these materials.

4.2 Results and discussion

4.2.1 Geometry and electronic structures of h-BN/Ni, h-BN/Co, and h-BN/Cu. In agreement with previous theoretical and experimental studies, we found that the most stable configuration of h-BN on the three metal surfaces has N on top of the metal and B on the fcc hollow site (Figure 4.1 top) from our DFT-PBE-D3 geometry optimizations.[36-37] All the subsequent calculations are carried out with this configuration. The distances between h-BN and the metal top layers are 2.18 Å, 2.14 Å, and 3.02 Å for Ni, Co, and Cu, respectively. From the side view of the structures (Figure 4.1 bottom), one can see that the interfacial interaction is the weakest for Cu, which is reflected in the interfacial binding energy per BN unit: -0.25 eV on Ni, -0.34 eV on Co, and -0.16 eV on Cu. From the plots of the charge density difference (Figure 4.1 bottom), one can clearly see that electrons migrate to the interfacial region and accumulate mainly below the electron-deficient B atoms. It is expected that the electrons at the interface will play important roles in electrocatalysis.

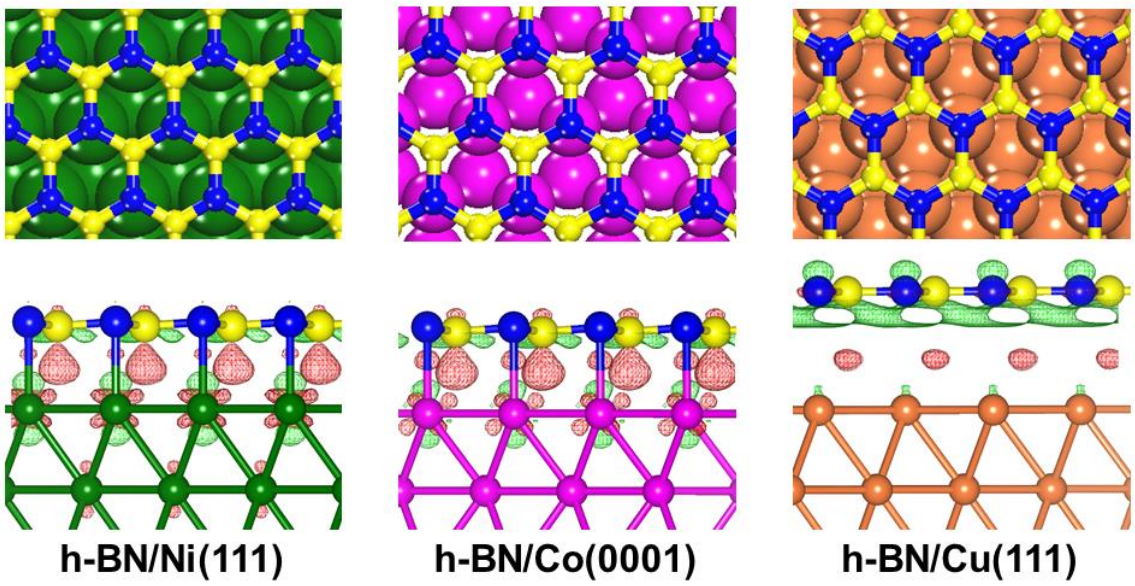

Figure 4.1. Top view (upper panel) and side view (lower panel) of the optimized structures for h-BN/Ni(111), h-BN/Co(0001), and h-BN/Cu(111). In the side view, isosurface plots of the charge density difference are also shown. The charge accumulation region is in red and the charge depletion region is in green. The isosurface value for h-BN/Ni(111) and h-BN/Co(0001) is 0.004 eV/Å^3, while for h-BN/Cu(111) it is 0.0006 eV/Å^3. B, yellow; N, blue; Ni, green; Co, magenta; Cu, orange.

4.2.2 Adsorption of key intermediates on h-BN/Ni, h-BN/Co, and h-BN/Cu.

To understand the electrocatalytic activities of h-BN/Ni, h-BN/Co, and h-BN/Cu toward CO_2 reduction, we first examine the binding energies of three key intermediates (*H, *HCOO, and *COOH). *H is the only intermediate during HER (* + H^+ + e^- → *H; *H + H^+ + e^- → H_2 or *H + *H → H_2), and the free energy of H adsorption has been used as a descriptor for HER activity.[46] The first protonation of CO_2 can proceed via two channels: (i) at the C atom to form *HCOO (* + CO_2 + H^+ + e^- → *HCOO), then to HCOOH (*HCOO + H^+ + e^- → HCOOH); (ii) at the O atom to form *COOH (* + CO_2 + H^+ + e^- → *COOH), then to CO and H_2O (*COOH + H^+ + e^- → *CO + H_2O).[41]

Figure 4.2 shows the binding energies of H, HCOO, and COOH on the h-BN monolayer, Ni(111) surface, and h-BN/Ni(111). One can see that they are all very

positive on h-BN, indicating that the h-BN monolayer itself is very inert and the adsorption is highly unfavorable. On the contrary, Ni(111) has strong interaction with the three intermediates, especially HCOO. Interestingly, h-BN/Ni(111) displays a very different trend from either h-BN or Ni(111). The comparison with Ni(111) is especially interesting: the binding of H and COOH is greatly reduced on h-BN/Ni(111) than on Ni(111), while the strong binding of HCOO is only affected slightly. This change in binding will have a profound impact on the selectivity of CO_2 reduction vs. HER as we will examine below. In addition, we compared the binding energies of CO_2 and H_2O on h-BN, Ni, and h-BN/Ni in Table 4.1. One can see that CO_2 has a slightly favorable interaction with all three surfaces at a similar strength, while H_2O adsorption is much more stronger on Ni(111) than on h-BN or h-BN/Ni(111).

Table 4.1. Binding energies (eV) of CO_2 and H_2O on h-BN, Ni(111), and h-BN/Ni(111).

	h-BN	**Ni(111)**	**h-BN/Ni(111)**
CO_2	-0.17	-0.22	-0.23
H_2O	-0.12	-0.52	-0.16

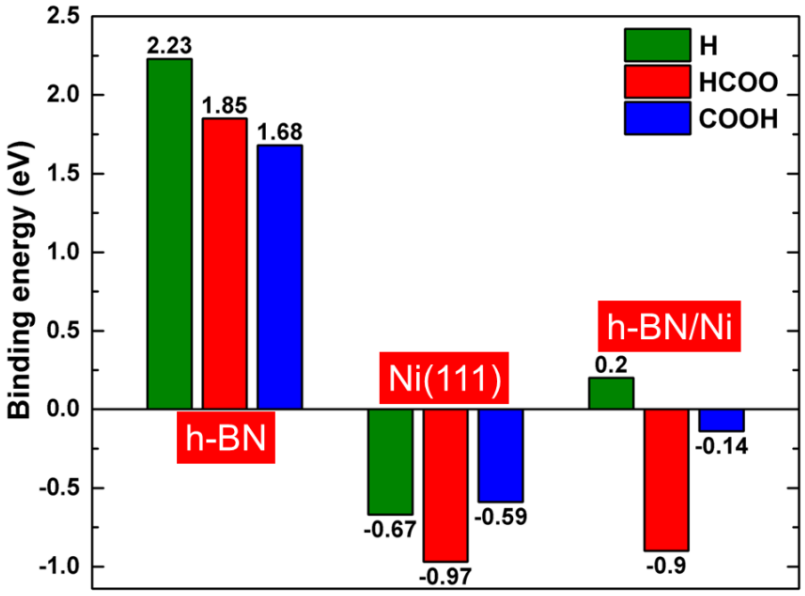

Figure 4.2. Binding energies (eV) of H, HCOO, and COOH on the h-BN monolayer, Ni(111), and h-BN/Ni(111).

The optimized geometry structures for H, HCOO, and COOH on h-BN, Ni(111), and h-BN/Ni(111) are shown in Figure 4.3. On the unsupported h-BN monolayer, H is bonded to B with a distance of 1.370 Å, while HCOO and COOH are more than 2 Å away from the surface. On Ni(111), H is at the fcc hollow site with H-Ni distance of 1.710 Å; HCOO is bonded to two Ni atoms through two O atoms (O-Ni distance: 1.963Å), and COOH is bridged between two Ni atoms through C and O atoms (C-Ni: 1.859 Å; O-Ni:2.032 Å). On h-BN/Ni(111), all three intermediates interact with the B atoms: 1.232 Å H-B bond for H, 1.657 Å O-B bond for HCOO, and 1.654 Å C-B bond for COOH. From Figure 4.1, we know that electronic charges are transferred from Ni to B in h-BN/Ni(111). These extra electrons can provide the valence for adsorbing the intermediates. Our analysis of the Bader charges of the adsorbates on h-BN/Ni(111)

support this explanation: we found that there is -0.451|e| on H, -0.706|e| on HCOO, and -0.543|e| on COOH.

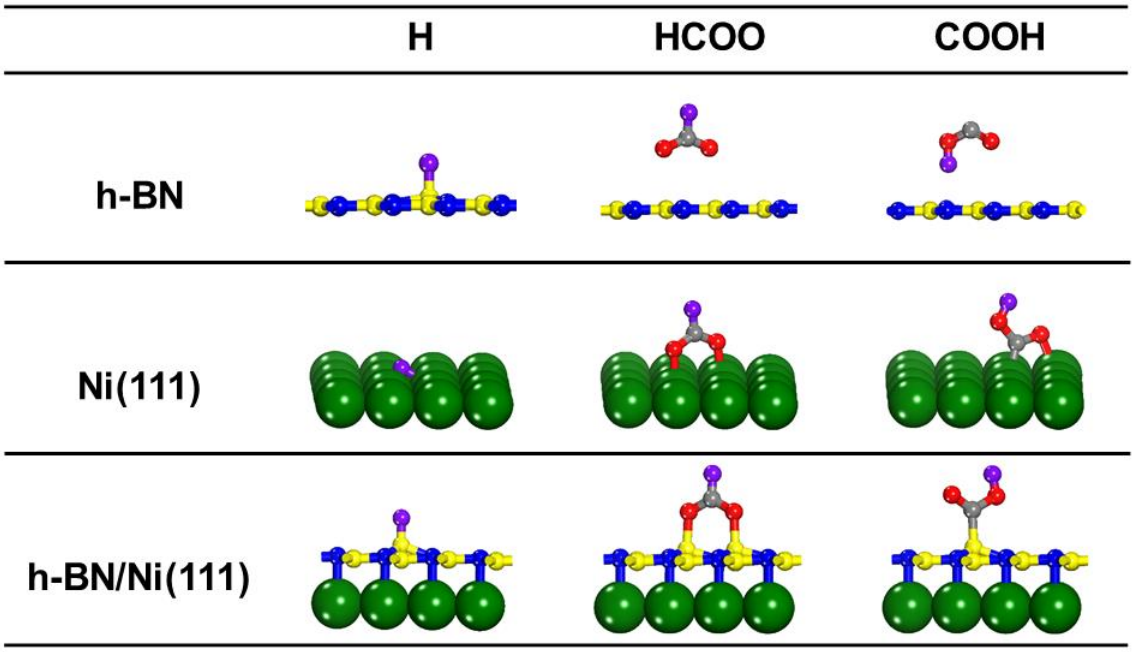

Figure 4.3. Optimized geometry structures for H, HCOO, and COOH on the h-BN monolayer, Ni(111), and h-BN/Ni(111). Only the topmost layer of Ni is shown. B, yellow; N, blue; Ni, green; H, purple; C, grey; O, red.

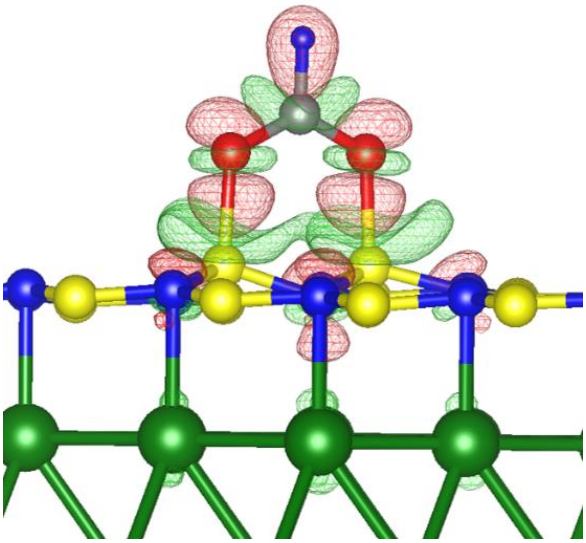

Figure 4.4. Isosurface plot of the charge density difference for HCOO adsorption on h-BN/Ni(111). The charge accumulation region is in red and the charge depletion region is in green. The isosurface value is 0.004 eV/Å^3. B, yellow; N, blue; Ni, green; H, purple; C, grey; O, red.

In order to further understand the mechanism of HCOO adsorption on h-BN/Ni(111), we plotted the charge density difference for HCOO adsorption on h-BN/Ni(111). As shown in Figure 4.4, there is a significant electron transfer from mainly the B atoms (and slightly the subsurface Ni atoms) to the O atoms of the HCOO intermediate and along the B-O bonds on the h-BN surface. In other words, the electrons accumulated on the B atoms of h-BN from the Ni substrate (Figure 4.1) are now used to promote adsorption of the HCOO intermediate on the surface.

We further analyzed the local density of states for the HCOO intermediate adsorbed on the unsupported h-BN and the h-BN/Ni surface. First, one can see that due to the charge transfer from the metal substrate, the Ni-supported h-BN becomes slightly metallic (Figure 4.5b), in contrast with the wide gap in the unsupported h-BN (Figure 4.5a). Second, the 2p orbitals of B atoms in h-BN are much better hybridized with the 2p

orbitals of O atoms in HCOO on h-BN/Ni (Figure 4.5b) than on h-BN alone (Figure 4.5a). So the Ni metal promotes HCOO adsorption on BN by charge transfer to BN, particularly to the B atoms (Figure 4.1) that then bond via their 2p orbitals to the O 2p orbitals of HCOO.

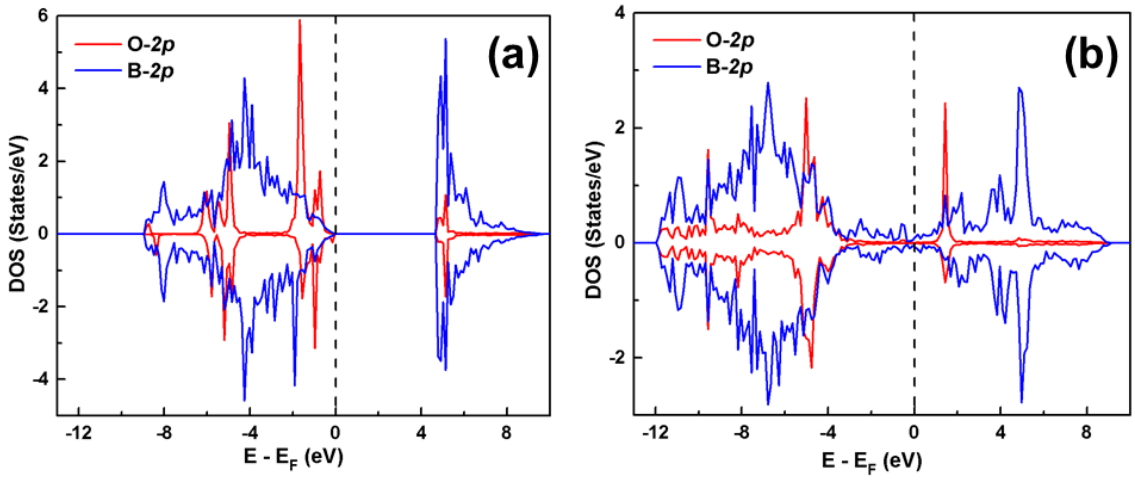

Figure 4.5. Local density of states (DOS) of the HCOO intermediate: (a) on the unsupported h-BN; (b) on h-BN/Ni.

Figure 4.3 shows that the favored intermediate on h-BN/Ni(111) is the one that preferentially binds via O (HCOO), rather than via C (COOH). The key reason for this selectivity is the difference in electronegativity between C (2.55) and O (3.44). Because B (2.04) is electron-deficient, a more electronegative element such as O can pull more electrons away from B than C does, thereby forming a stronger bond. This reasoning is in agreement with the Bader charge analysis after adsorption: there is more electron transfer from the h-BN/Ni(111) surface to the HCOO intermediate via the surface B-O bonds (-0.706|e|) than to the COOH intermediate via the surface B-C bond (-0.543|e|). In addition, the difference between the two types of bonds is well reflected in the gas-phase bond

strengths which are 8.38 eV for B-O and 4.64 eV for B-C.[47] Hence the preference of B to bond with O than with C also manifests on the h-BN/Ni(111) surface, though to a less extent. The theoretical study of O_2 adsorption and reaction on h-BN/metal surfaces by Mao, et al.[35] further confirmed that the h-BN/metal interfaces would be very beneficial for oxygen-involved catalysis, such as CO_2 reduction, oxygen reduction, and deoxygenation.

Table 4.2 shows the binding energies of H, HCOO, and COOH on Co(0001), h-BN/Co(0001), Cu(111), and h-BN/Cu(111). The interfacial structure and bonding of h-BN/Ni(111) and h-BN/Co(0001) are very similar (Figure 4.1), so we found that their binding energies for H, HCOO, and COOH also have the same trend, in comparison with those on h-BN and the metal. The interfacial interaction of h-BN/Cu(111) is much weaker, so the electronic structure of h-BN on Cu(111) is less perturbed; in this case, both H and COOH adsorptions are still quite unfavorable, while HCOO is favorable but not very strong. Figure 4.6 shows the optimized geometry structures for H, HCOO, and COOH on Co(0001), h-BN/Co(0001), Cu(111), and h-BN/Cu(111).

Table 4.2. Binding energies (eV) of H, HCOO, and COOH on Co(0001), h-BN/Co(0001), Cu(111), and h-BN/Cu(111).

	H	**HCOO**	**COOH**
Co(0001)	-0.65	-1.04	-0.57
h-BN/Co(0001)	0.28	-0.77	-0.05
Cu(111)	-0.33	-0.76	0.01
h-BN/Cu(111)	0.74	-0.35	0.42

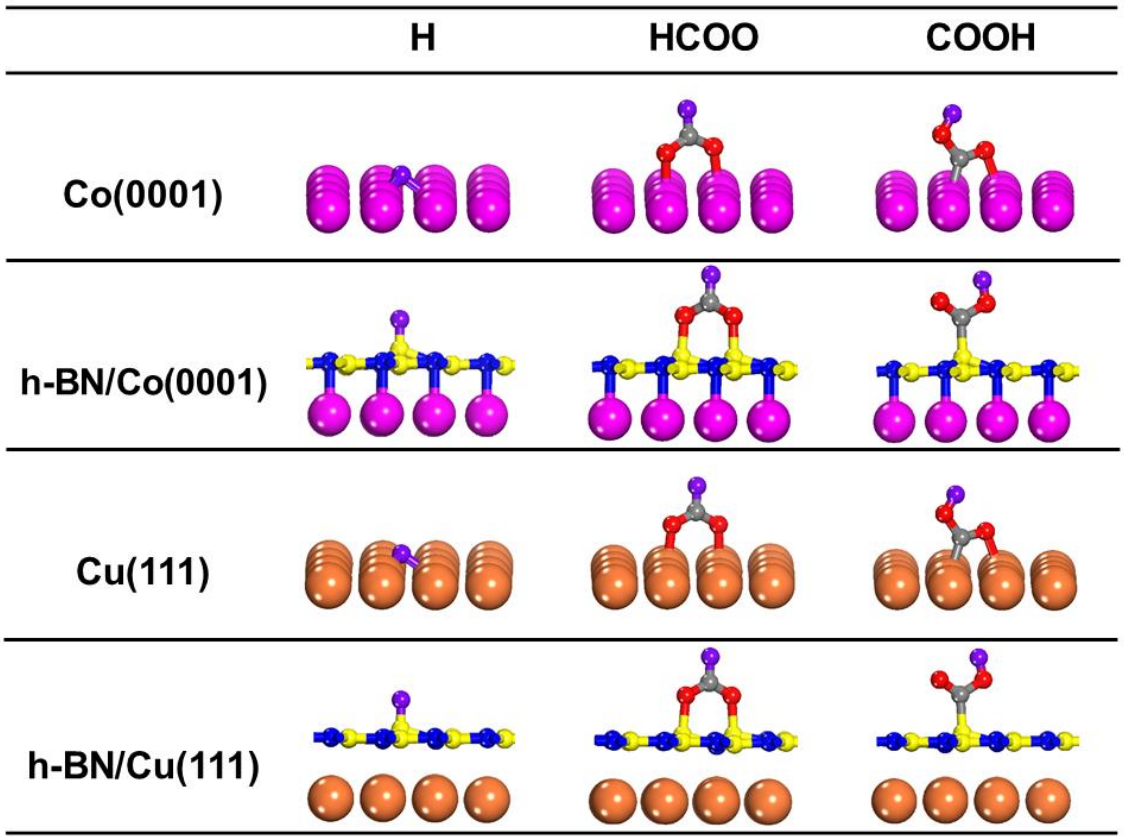

Figure 4.6. Optimized geometry structures for H, HCOO, and COOH on Co(0001), h-BN/Co(0001), Cu(111), and h-BN/Cu(111). Only the topmost layer of the metal is shown. B, yellow; N, blue; Co, magenta; Cu, orange; H, purple; C, grey; O, red.

4.2.3 Electrocatalytic activities of h-BN/Ni, h-BN/Co, and h-BN/Cu for CO_2 reduction.

The distinct difference in binding energies among H, HCOO, and COOH due to the presence of the h-BN on the metal and the interfacial electron transfer suggests that the h-BN/metal systems can be used as electrocatalysts to control the selectivity of CO_2 reduction and the competition against HER. To test this idea, we calculated the free-energy profiles for the formation of H_2, HCOOH, and CO on both the pure metal and the h-BN/metal system. Figure 4.7 shows the free energy diagrams for Ni(111) and h-

BN/Ni(111). As one can see, on the Ni(111) surface, formation of H_2 (rather than HCOOH or CO) is the most favorable pathway, which is in agreement with the experimental observations.[38-39] On h-BN/Ni(111), formation of HCOOH becomes more favorable, because the competitive process of HER is filtered out by the h-BN layer due to the weak binding of H. Therefore, in contrast to Ni, h-BN/Ni can be a very good electrocatalyst for selective CO_2 reduction to HCOOH.

The free-energy changes in Figure 4.7 indicate that CO_2 reduction to HCOOH is preferred than HER on h-BN/Ni. To confirm that this is also the case kinetically, we have computed the activation energies for the elementary electrochemical reduction steps. We used an explicit solvation model of proton in a water cluster for the CO_2 reduction to HCOOH step. The activation energy was found to be 0.09 eV for CO_2 to HCOO, and the subsequent step of HCOO to HCOOH was also found to have a small barrier of about 0.10 eV. (We note that similar magnitude of activation energies was found for electrochemical proton reduction of O_2 to OOH and OH to H_2O on Pt.[48-49]) Since the reaction free-energy itself for the first HER step is already at 0.50 eV, the much smaller activation energies for CO_2 reduction to HCOOH hence confirmed the selectivity of CO_2 reduction over HER on the h-BN/Ni surface.

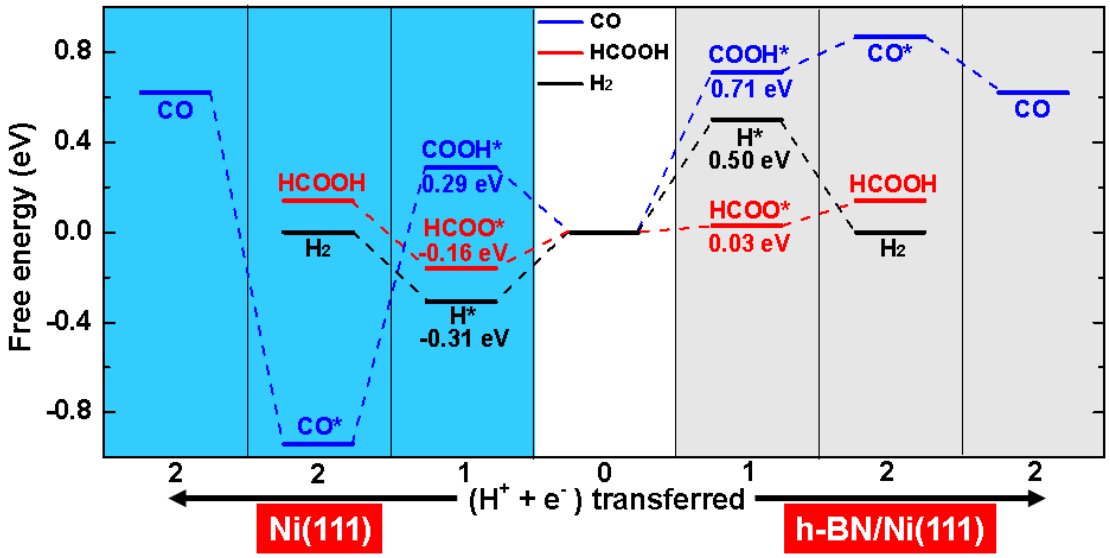

Figure 4.7. Calculated free energy diagrams for the reaction pathways to CO (blue), HCOOH (red), and H_2 (black) on Ni(111) (left) and h-BN/Ni(111) (right).

The free energy diagrams for h-BN/Co and h-BN/Cu are shown in Figure 4.8 and Figure 4.9, respectively. We found that HER on Co can be also suppressed by the h-BN layer, making h-BN/Co a good catalyst for CO_2 reduction to HCOOH as well. However, h-BN/Cu is not as promising as h-BN/Co or h-BN/Ni for CO_2 reduction, despite that the HER activity is also highly suppressed. As shown in Figure 4.9, the free energy change (ΔG) of the potential-limiting step for the formation of HCOOH on h-BN/Cu is quite positive (0.57 eV) due to the weak binding of HCOO, while that for the formation of CO is even higher (1.35 eV). This can be attributed to the weak interaction between h-BN and Cu.

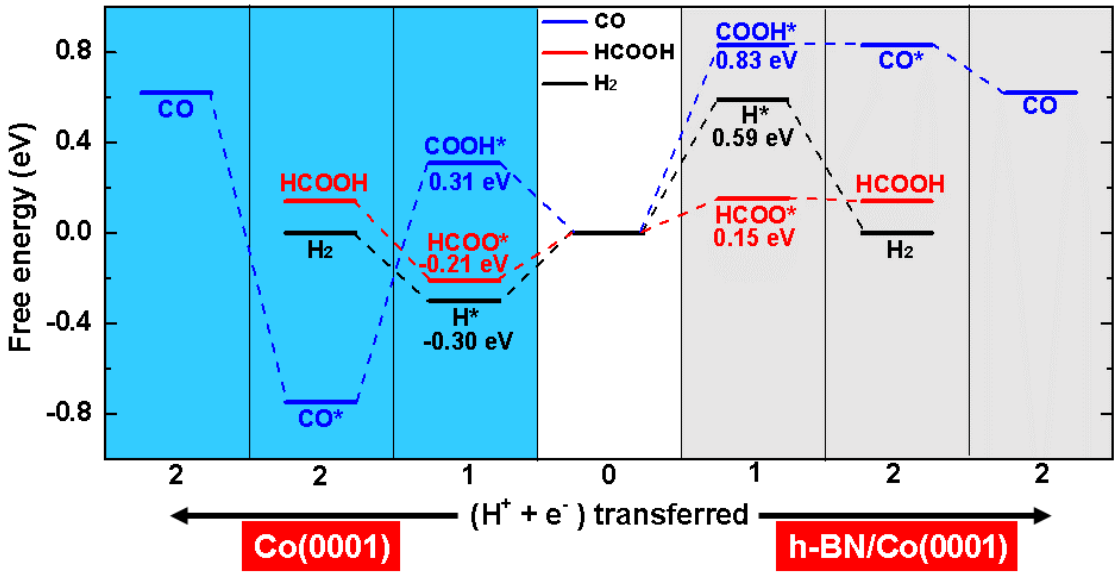

Figure 4.8. Calculated free energy diagrams for the reaction pathways to CO (blue), HCOOH (red), and H_2 (black) on Co(0001) (left) and h-BN/Co(0001) (right).

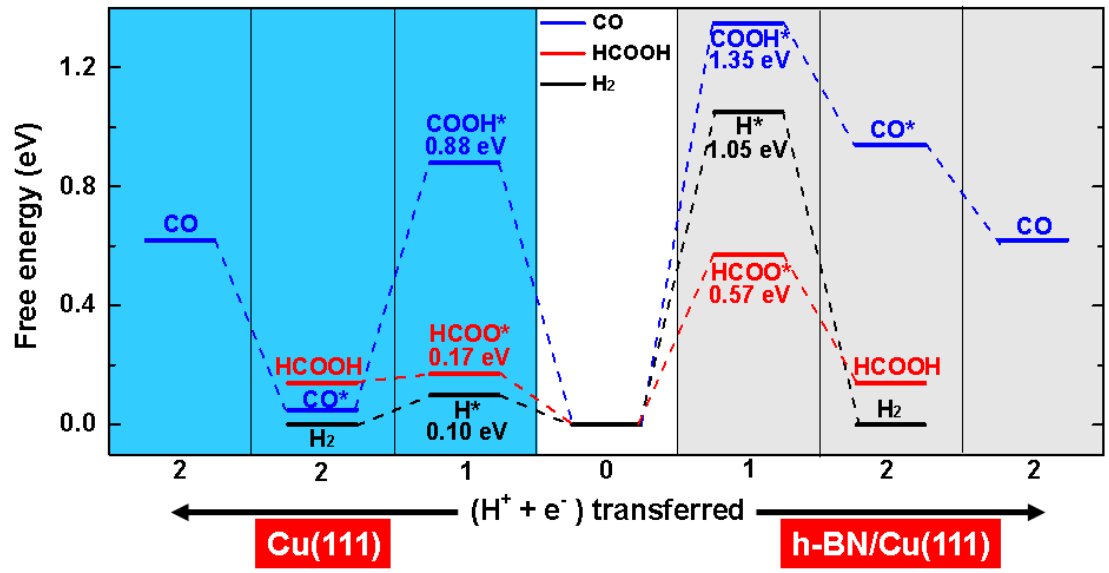

Figure 4.9. Calculated free energy diagrams for the reaction pathways to CO (blue), HCOOH (red), and H_2 (black) on Cu(111) (left) and h-BN/Cu(111) (right).

4.3 Implications.

The results presented in the current work will have a broad impact. First, we show that the chemically inert h-BN monolayer can be used as an electrocatalyst for CO_2 reduction when combined with a suitable transition metal. This will bring new opportunities to the application of h-BN in the area of catalysis. Second, we develop an environmental-friendly catalyst for the electrochemical CO_2 reduction to HCOOH. Electrochemical CO_2 reduction has attracted great attention recently, since it can not only produce useful fuels but also low the atmospheric level of CO_2. Although catalysts such as Pb, Hg, In, and Sn are also able to promote CO_2 reduction to HCOOH,[38-39, 42] they are highly toxic, expensive, or both. Last but not the least, our results suggest a new method to control reaction selectivity via interface engineering with the h-BN monolayer.

The present work focuses on a perfect h-BN monolayer on different transition metals. We note that the selectivity can be dramatically changed if the h-BN layer is not perfect but contains defects and/or edges. In fact, it has been shown that the BN nanosheet on gold is highly active for HER due to the edge sites.[50] So it would be interesting to find out how the defects and edges impact the h-BN/metal catalyst's selectivity for CO_2 reduction vs. HER. Further studies are warranted.

4.4 Conclusions

In summary, we have investigated the interfacial materials of the h-BN monolayer supported on transition metals including Co, Ni, and Cu as well as their electrocatalytic activities for CO_2 reduction from first principles. We found that electron transfer from the

metal to h-BN led to a unique chemical reactivity of the h-BN/metal interface for the key intermediates during hydrogen evolution and CO_2 reduction. Namely, H adsorption is greatly reduced on the h-BN/metal surface, while HCOO adsorption is only slightly affected, in comparison with adsorption on the pure metal surface. This differential adsorption led to selectivity control for electroreduction of CO_2. The calculated free energy profiles showed that h-BN/Ni and h-BN/Co can be very good electrocatalysts for CO_2 reduction to HCOOH by avoiding HER. This work demonstrates the great potential of tuning the chemical reactivity of a metal surface by interfacing the h-BN monolayer for selectivity control in electrocatalysis.

References

1. Lipp, A.; Schwetz, K. A.; Hunold, K., Hexagonal Boron Nitride: Fabrication, Properties and Applications. *J. Eur. Ceram. Soc.* **1989**, *5*, 3-9.

2. Watanabe, K.; Taniguchi, T.; Kanda, H., Direct-Bandgap Properties and Evidence for Ultraviolet Lasing of Hexagonal Boron Nitride Single Crystal. *Nat. Mater.* **2004**, *3*, 404-409.

3. Raman, C.; Meneghetti, P., Boron Nitride Finds New Applications in Thermoplastic Compounds. *Plastics, Additives and Compounding* **2008**, *10*, 26-31.

4. Watanabe, K.; Taniguchi, T.; Niiyama, T.; Miya, K.; Taniguchi, M., Far-Ultraviolet Plane-Emission Handheld Device Based on Hexagonal Boron Nitride. *Nat. Photon.* **2009**, *3*, 591-594.

5. Grant, J. T.; Carrero, C. A.; Goeltl, F.; Venegas, J.; Mueller, P.; Burt, S. P.; Specht, S. E.; McDermott, W. P.; Chieregato, A.; Hermans, I., Selective Oxidative Dehydrogenation of Propane to Propene Using Boron Nitride Catalysts. *Science* **2016**, *354*, 1570-1573.

6. Vu, Q. A.; Shin, Y. S.; Kim, Y. R.; Kang, W. T.; Kim, H.; Luong, D. H.; Lee, I. M.; Lee, K.; Ko, D.-S.; Heo, J., Two-Terminal Floating-Gate Memory with Van Der Waals Heterostructures for Ultrahigh on/Off Ratio. *Nat. Commun.* **2016**, *7*, 12725.

7. Liu, S.; van Duin, A. C.; van Duin, D. M.; Liu, B.; Edgar, J. H., Atomistic Insights into Nucleation and Formation of Hexagonal Boron Nitride on Nickel from First-Principles-Based Reactive Molecular Dynamics Simulations. *ACS nano* **2017**, *11*, 3585-3596.

8. Ma, L.; Zeng, X. C., Catalytic Directional Cutting of Hexagonal Boron Nitride: The Roles of Interface and Etching Agents. *Nano Lett.* **2017**, *17*, 3208-3214.

9. Qi, Y.; Zhang, Z.; Deng, B.; Zhou, X.; Li, Q.; Hong, M.; Li, Y.; Liu, Z.; Zhang, Y., Irreparable Defects Produced by the Patching of H-Bn Frontiers on Strongly Interacting Re (0001) and Their Electronic Properties. *J. Am. Chem. Soc.* **2017**, *139*, 5849-5856.

10. Giovannetti, G.; Khomyakov, P. A.; Brocks, G.; Kelly, P. J.; Van Den Brink, J., Substrate-Induced Band Gap in Graphene on Hexagonal Boron Nitride: Ab Initio Density Functional Calculations. *Phys. Rev. B* **2007**, *76*, 073103.

11. Ci, L.; Song, L.; Jin, C.; Jariwala, D.; Wu, D.; Li, Y.; Srivastava, A.; Wang, Z.; Storr, K.; Balicas, L., Atomic Layers of Hybridized Boron Nitride and Graphene Domains. *Nat. Mater.* **2010**, *9*, 430-435.

12. Dean, C. R.; Young, A. F.; Meric, I.; Lee, C.; Wang, L.; Sorgenfrei, S.; Watanabe, K.; Taniguchi, T.; Kim, P.; Shepard, K. L., Boron Nitride Substrates for High-Quality Graphene Electronics. *Nat. Nanotechnol.* **2010**, *5*, 722-726.

13. Britnell, L.; Gorbachev, R. V.; Jalil, R.; Belle, B. D.; Schedin, F.; Katsnelson, M. I.; Eaves, L.; Morozov, S. V.; Mayorov, A. S.; Peres, N. M., Electron Tunneling through Ultrathin Boron Nitride Crystalline Barriers. *Nano Lett.* **2012**, *12*, 1707-1710.

14. Jiang, Y.; Mao, J.; Duan, J.; Lai, X.; Watanabe, K.; Taniguchi, T.; Andrei, E. Y., Visualizing Strain-Induced Pseudomagnetic Fields in Graphene through an Hbn Magnifying Glass. *Nano Lett.* **2017**, *17*, 2839-2843.

15. Corso, M.; Auwärter, W.; Muntwiler, M.; Tamai, A.; Greber, T.; Osterwalder, J., Boron Nitride Nanomesh. *Science* **2004**, *303*, 217-220.

16. Muntwiler, M.; Auwärter, W.; Seitsonen, A.; Osterwalder, J.; Greber, T., Rocking-Motion-Induced Charging of C_{60} on H-BN/Ni(111). *Phys. Rev. B* **2005**, *71*, 121402.

17. Kahle, S.; Deng, Z.; Malinowski, N.; Tonnoir, C. n.; Forment-Aliaga, A.; Thontasen, N.; Rinke, G.; Le, D.; Turkowski, V.; Rahman, T. S., The Quantum Magnetism of Individual Manganese-12-Acetate Molecular Magnets Anchored at Surfaces. *Nano Lett.* **2011**, *12*, 518-521.

18. Zhu, W., et al., Taming Interfacial Electronic Properties of Platinum Nanoparticles on Vacancy-Abundant Boron Nitride Nanosheets for Enhanced Catalysis. *Nat. Commun.* **2017**, *8*, 15291.

19. Zhao, J.; Chen, Z., Single Mo Atom Supported on Defective Boron Nitride Monolayer as an Efficient Electrocatalyst for Nitrogen Fixation: A Computational Study. *J. Am. Chem. Soc.* **2017**, *139*, 12480-12487.

20. Shi, Y.; Hamsen, C.; Jia, X.; Kim, K. K.; Reina, A.; Hofmann, M.; Hsu, A. L.; Zhang, K.; Li, H.; Juang, Z.-Y., Synthesis of Few-Layer Hexagonal Boron Nitride Thin Film by Chemical Vapor Deposition. *Nano Lett.* **2010**, *10*, 4134-4139.

21. Song, L.; Ci, L.; Lu, H.; Sorokin, P. B.; Jin, C.; Ni, J.; Kvashnin, A. G.; Kvashnin, D. G.; Lou, J.; Yakobson, B. I., Large Scale Growth and Characterization of Atomic Hexagonal Boron Nitride Layers. *Nano Lett.* **2010**, *10*, 3209-3215.

22. Müller, F.; Hüfner, S.; Sachdev, H.; Laskowski, R.; Blaha, P.; Schwarz, K., Epitaxial Growth of Hexagonal Boron Nitride on Ag (111). *Phys. Rev. B* **2010**, *82*, 113406.

23. Kim, K. K.; Hsu, A.; Jia, X.; Kim, S. M.; Shi, Y.; Hofmann, M.; Nezich, D.; Rodriguez-Nieva, J. F.; Dresselhaus, M.; Palacios, T., Synthesis of Monolayer Hexagonal

Boron Nitride on Cu Foil Using Chemical Vapor Deposition. *Nano Lett.* **2011**, *12*, 161-166.

24. Sutter, P.; Lahiri, J.; Albrecht, P.; Sutter, E., Chemical Vapor Deposition and Etching of High-Quality Monolayer Hexagonal Boron Nitride Films. *ACS nano* **2011**, *5*, 7303-7309.

25. Ismach, A.; Chou, H.; Ferrer, D. A.; Wu, Y.; McDonnell, S.; Floresca, H. C.; Covacevich, A.; Pope, C.; Piner, R.; Kim, M. J., Toward the Controlled Synthesis of Hexagonal Boron Nitride Films. *ACS Nano* **2012**, *6*, 6378-6385.

26. Nagashima, A.; Tejima, N.; Gamou, Y.; Kawai, T.; Oshima, C., Electronic Dispersion Relations of Monolayer Hexagonal Boron Nitride Formed on the Ni (111) Surface. *Phys. Rev. B* **1995**, *51*, 4606.

27. Auwärter, W.; Kreutz, T.; Greber, T.; Osterwalder, J., Xpd and Stm Investigation of Hexagonal Boron Nitride on Ni (111). *Surf. Sci.* **1999**, *429*, 229-236.

28. Morscher, M.; Corso, M.; Greber, T.; Osterwalder, J., Formation of Single Layer H-BN on Pd (111). *Surf. Sci.* **2006**, *600*, 3280-3284.

29. Vinogradov, N. A.; Zakharov, A.; Ng, M. L.; Mikkelsen, A.; Lundgren, E.; Mårtensson, N.; Preobrajenski, A., One-Dimensional Corrugation of the H-BN Monolayer on Fe (110). *Langmuir* **2012**, *28*, 1775-1781.

30. Berner, S.; Corso, M.; Widmer, R.; Groening, O.; Laskowski, R.; Blaha, P.; Schwarz, K.; Goriachko, A.; Over, H.; Gsell, S., Boron Nitride Nanomesh: Functionality from a Corrugated Monolayer. *Angew. Chem. Int. Ed.* **2007**, *46*, 5115-5119.

31. Uosaki, K.; Elumalai, G.; Noguchi, H.; Masuda, T.; Lyalin, A.; Nakayama, A.; Taketsugu, T., Boron Nitride Nanosheet on Gold as an Electrocatalyst for Oxygen Reduction Reaction: Theoretical Suggestion and Experimental Proof. *J. Am. Chem. Soc.* **2014**, *136*, 6542-6545.

32. Zhang, Y.; Weng, X.; Li, H.; Li, H.; Wei, M.; Xiao, J.; Liu, Z.; Chen, M.; Fu, Q.; Bao, X., Hexagonal Boron Nitride Cover on Pt (111): A New Route to Tune Molecule–Metal Interaction and Metal-Catalyzed Reactions. *Nano Lett.* **2015**, *15*, 3616-3623.

33. Deng, D.; Novoselov, K.; Fu, Q.; Zheng, N.; Tian, Z.; Bao, X., Catalysis with Two-Dimensional Materials and Their Heterostructures. *Nat. Nanotechnol.* **2016**, *11*, 218-230.

34. Lyalin, A.; Gao, M.; Taketsugu, T., When Inert Becomes Active: A Fascinating Route for Catalyst Design. *Chem. Rec.* **2016**, *16*, 2324-2337.

35. Mao, K.; Wu, X.; Yang, J., Enhanced Selective Oxidation of H-Bn Nanosheet through a Substrate-Mediated Localized Charge Effect. *Phys. Chem. Chem. Phys.* **2017**, *19*, 4435-4439.

36. Laskowski, R.; Blaha, P.; Schwarz, K., Bonding of Hexagonal Bn to Transition Metal Surfaces: An Ab Initio Density-Functional Theory Study. *Phys. Rev. B* **2008**, *78*, 045409.

37. Diaz, J. G.; Ding, Y.; Koitz, R.; Seitsonen, A. P.; Iannuzzi, M.; Hutter, J., Hexagonal Boron Nitride on Transition Metal Surfaces. *Theor. Chem. Acc.* **2013**, *132*, 1350.

38. Hori, Y.; Kikuchi, K.; Suzuki, S., Production of Co and Ch_4 in Electrochemical Reduction of Co_2 at Metal Electrodes in Aqueous Hydrogencarbonate Solution. *Chem. Lett.* **1985**, *14*, 1695-1698.

39. Noda, H.; Ikeda, S.; Oda, Y.; Imai, K.; Maeda, M.; Ito, K., Electrochemical Reduction of Carbon Dioxide at Various Metal Electrodes in Aqueous Potassium Hydrogen Carbonate Solution. *Bull. Chem. Soc. Jpn.* **1990**, *63*, 2459-2462.

40. Jitaru, M.; Lowy, D.; Toma, M.; Toma, B.; Oniciu, L., Electrochemical Reduction of Carbon Dioxide on Flat Metallic Cathodes. *J. Appl. Electrochem.* **1997**, *27*, 875-889.

41. Hori, Y., Electrochemical CO_2 Reduction on Metal Electrodes. In *Modern Aspects of Electrochemistry*, Springer: 2008; pp 89-189.

42. Ma, S.; Kenis, P. J., Electrochemical Conversion of CO_2 to Useful Chemicals: Current Status, Remaining Challenges, and Future Opportunities. *Curr. Opin. Chem. Eng.* **2013**, *2*, 191-199.

43. Hori, Y.; Murata, A.; Takahashi, R., Formation of Hydrocarbons in the Electrochemical Reduction of Carbon Dioxide at a Copper Electrode in Aqueous Solution. *J. Chem. Soc., Faraday Trans. 1* **1989**, *85*, 2309-2326.

44. Peterson, A. A.; Nørskov, J. K., Activity Descriptors for CO_2 Electroreduction to Methane on Transition-Metal Catalysts. *J. Phys. Chem. Lett.* **2012**, *3*, 251-258.

45. Peterson, A. A.; Abild-Pedersen, F.; Studt, F.; Rossmeisl, J.; Nørskov, J. K., How Copper Catalyzes the Electroreduction of Carbon Dioxide into Hydrocarbon Fuels. *Energy Environ. Sci.* **2010**, *3*, 1311-1315.

46. Nørskov, J. K.; Bligaard, T.; Logadottir, A.; Kitchin, J. R.; Chen, J. G.; Pandelov, S.; Stimming, U., Trends in the Exchange Current for Hydrogen Evolution. *J. Electrochem. Soc.* **2005**, *152*, J23-J26.

47. Haynes, W. M., *Crc Handbook of Chemistry and Physics*; CRC press, 2014.

48. Janik, M. J.; Taylor, C. D.; Neurock, M., First-Principles Analysis of the Initial Electroreduction Steps of Oxygen over Pt (111). *J. Electrochem. Soc.* **2009**, *156*, B126-B135.

49. Tripković, V.; Skúlason, E.; Siahrostami, S.; Nørskov, J. K.; Rossmeisl, J., The Oxygen Reduction Reaction Mechanism on Pt (111) from Density Functional Theory Calculations. *Electrochim. Acta* **2010**, *55*, 7975-7981.

50. Uosaki, K.; Elumalai, G.; Dinh, H. C.; Lyalin, A.; Taketsugu, T.; Noguchi, H., Highly Efficient Electrochemical Hydrogen Evolution Reaction at Insulating Boron Nitride Nanosheet on Inert Gold Substrate. *Sci. Rep.* **2016**, *6*, 32217.

Chapter 5

Beyond the Staple Motif: New Order at the Thiolate-gold Interface

Abstract

Staple motifs in the form of -RS(AuSR)$_x$- (x=1, 2, 3, etc.) are the most common structural feature at the interface of the thiolate-protected gold nanoclusters, $Au_n(SR)_m$. However, the recently solved structure of $Au_{92}(SR)_{44}$, in which the facets of the Au_{84} core are protected mainly by the bridging thiolates, challenges the staple hypothesis. Herein we explore the surface sensitivity of the thiolate-gold interface from first principles density functional theory. We find that the interfacial structures of thiolates on gold are surface sensitive: while the staple motif (such as -RS-Au-SR-) is preferred on Au(111), the bridging motif (-RS-) is preferred on Au(100) and Au(110). We show that this surface sensitivity is closely related to the coordination number of the surface Au atom on the different surfaces. To confirm the bridging motif is preferred on Au(100), we study self-assembled monolayers on Au(100) with two different ligands (the simple ligand methylthiolate and the experimental ligand 4-tert-butylbenzenethiolate). With this surface sensitivity, we categorize the structure-known $Au_n(SR)_m$ clusters into three groups: (1) no bridging; (2) ambiguous bridging; (3) distinct bridging. We further employ the surface sensitivity of the thiolate-Au interface to predict the protecting motifs of face-centered cubic (fcc) gold nanoparticles of different shapes. Our study provides a unifying view of

the $Au_n(SR)_m$ structures with guidelines for structure predictions of larger $Au_n(SR)_m$ clusters of a fcc core.

5.1 Introduction

Thiolate-protected gold nanoclusters in the formula of $Au_n(SR)_m$ have received considerable attention over the past decade owing to their unique structures and physicochemical properties that are not seen in the larger gold nanoparticles or bulk gold.[1-10] Their potential applications range from catalysis to bioimaging and protein labeling.[11-16] To date, total structures of about 20 such clusters ranging from $Au_{18}(SC_6H_{11})_{14}$ to $Au_{133}(SPh\text{-}p\text{-}^tBu)_{52}$ have been successfully solved via single-crystal X-ray crystallography.[17-38] Structure determinations of these clusters provide profound insights into the thiolate-gold interface and bonding, which are key to the formation and stability of the thiolate-protected gold nanoclusters. Among these clusters, $Au_{102}(SPh\text{-}p\text{-}COOH)_{44}$ was the first one crystallized and characterized; the 44 thiolate groups of the cluster form 19 RS-Au-SR motifs and 2 RS-Au-SR-Au-SR motifs on the cluster surface, which were termed the staple motif.[35] Similar RS-Au-SR motifs were also found in self-assembled monolayers (SAMs) on Au(111) with both experimental and theoretical studies.[39-41] These reports highlight the importance of the staple motifs at the thiolate-gold interface; it was hence hypothesized that the staple motifs are preferred at the thiolate-gold interface than the isolated or bridging thiolate (-RS-) group. Computationally, the preference of the staple motif over the bridging thiolate was demonstrated on Au(111) and small gold nanoclusters such as Au_{38}.[42]

The staple hypothesis has been successfully applied to predict structures for $Au_n(SR)_m$ clusters of known compositions and confirmed in subsequently reported structures. For example, Akola et al. proposed a structure model for $Au_{25}(SR)_{18}^-$,[43] in which an icosahedral Au_{13}-core is protected by 6 dimeric staple motifs, which was confirmed independently by two experimental research groups.[22-23] Likewise, Pei et al. and Aikens et al. have predicted the structure of $Au_{38}(SR)_{24}$ to have a face-fused bi-icosahedral Au_{23} core protected by six dimeric and three monomeric staple motifs,[44-45] which was again confirmed in the experimental crystal structure.[31]

As the dominance of the staple motif began to take root in our thinking of the thiolate-gold interface, the line between the staple motif and the bridging thiolate has become blurred in some reported structures, including Au_{36}(SPh-*p*-^{t}Bu)$_{24}$, Au_{28}(SPh-*p*-^{t}Bu)$_{20}$, and $[Au_{23}(S\text{-}c\text{-}C_6H_{11})_{16}]^-$. For example, the structure of Au_{36}(SPh-*p*-^{t}Bu)$_{24}$ can be viewed to have an fcc Au_{28} kernel protected by 4 dimeric staple motifs on 4 Au(111) facets and 12 bridging motifs on 6 Au(100) facets, or alternatively, as a Au_{20} kernel protected by 4 "regular" dimeric staple motifs and additional 4 "distorted" dimeric staple motifs.[30, 46] Likewise, this ambiguity is also manifested in $[Au_{23}(S\text{-}c\text{-}C_6H_{11})_{16}]^-$ and Au_{28}(SPh-*p*-^{t}Bu)$_{20}$.[47] Due to this duality in viewing the gold-thiolate interface, the staple hypothesis has been challenged but survived.

The recently solved structure of Au_{92}(SPh-*p*-^{t}Bu)$_{44}$, however, challenges the staple hypothesis to the fullest extent and demands a rethinking of the thiolate-gold interface, because here there is no ambiguity. Au_{92}(SPh-*p*-^{t}Bu)$_{44}$ has a highly regular fcc Au_{84} kernel with 16-gold-atom (001) facets and 12-gold-stom (100) and (010) facets, which

are distinctly and clearly covered by the bridging thiolates.[34] This new structure raises the key question about the surface sensitivity of the thiolate-gold interface. Previously, the preference of the staple motif was demonstrated only for the Au(111) surface. It is therefore of great importance to examine the energetic stability of staple vs. bridging mode at the gold-thiolate interface for other surfaces such as (100) and (110). In addition, the structure of $Au_{92}(SPh\text{-}p\text{-}^{t}Bu)_{44}$ now gives more weight to the view of the bridging thiolate for structures where ambiguity existed.

To understand the bridging motifs at the interface of the thiolate-protected gold nanoclusters in particular and to provide guidelines for future structure predictions in general, herein we study the surface sensitivity of the thiolate-gold interface with three low-Miller-index surfaces of gold including Au(111), Au(100), and Au(110) from first-principles density functional theory (DFT). We then explain the energetic trend found. Next we leverage the surface sensitivity to categorize the existing clusters into three groups: (1) no bridging, (2) ambiguous bridging, and (3) distinct bridging. Furthermore, we employ the surface sensitivity to predict the protecting motifs of fcc gold nanoparticles (smaller than 3 nm) with different shapes.

5.2 Results and Discussion

5.2.1 Bridging and staple motifs on Au(111), Au(100), and Au(110)

To examine the surface sensitivity of the thiolate-gold interface, we use the methylthiolate (MT) as an example. We tested all the possible adsorption sites on the three surfaces: top site, bridge site, fcc site, and hcp site on Au(111); top site, bridge site,

and square 4-fold hollow site on Au(100); top site, long bridge site, short bridge site, pseudo 3-fold hollow site, and rectangular 4-fold hollow site on Au(110). By comparing the binding energies, we find that the bridge sites are the most stable adsorption sites for MT on all the three surfaces. The sizes of the systems and the convergence test are summarized and provided in Tables 5.1-5.3. Figure 5.1 shows the most stable structures for MT on the three surfaces, where each MT binds to two neighboring surface gold atoms. This is also found to be the case for different Au-thiolate-Au interfaces of the molecular nanowires.[48-49]

Table 5.1. Binding energies (eV) of MT at different adsorption sites on Au(111) with different layers of slab. The initial angle between the surface normal and S-C bond is 30°. Structures started with the hcp sites all relaxed to the bridge sites.

	4 layers	**5 layers**	**6 layers**
top	-1.64	-1.57	-1.67
bridge	-1.99	-1.96	-2.08
fcc	-1.94	-1.91	-2.02
hcp	bridge	bridge	bridge

Table 5.2. Binding energies (eV) of MT at different adsorption sites on Au(100) with different layers of slab. Structures started with the top sites all relaxed to the bridge sites.

	4 layers	**5 layers**	**6 layers**
top	bridge	bridge	bridge
bridge	-2.41	-2.34	-2.36
square 4-fold hollow	-2.18	-2.08	-2.19

Table 5.3. Binding energies (eV) of MT at different adsorption sites on Au(110) with different layers of slab. Structures started with the top sites, pseudo 3-fold hollow sites, and rectangular 4-fold hollow sites all relaxed to the short bridge sites.

	4 layers	**5 layers**	**6 layers**
top	short bridge	short bridge	short bridge
long bridge	-2.39	-2.31	-2.36
short bridge	-2.59	-2.47	-2.56
pseudo 3-fold hollow	short bridge	short bridge	short bridge
rectangular 4-fold hollow	short bridge	short bridge	short bridge

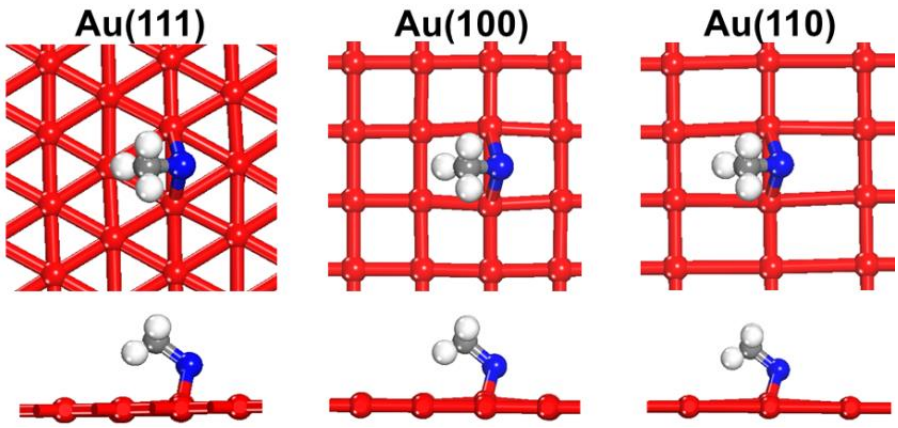

Figure 5.1. Top (upper panel) and side (lower panel) views of the optimized structures for bridging MT on Au(111), Au(100), and Au(110) surfaces. Only the topmost surface layer is shown. Au, red; S, blue; C, grey; H, white.

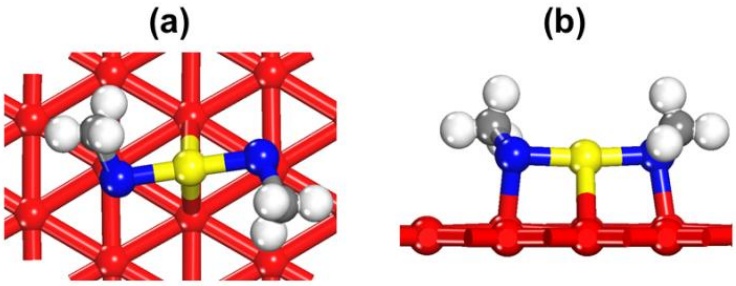

Figure 5.2. Top (a) and side (b) views of the optimized structures for $CH_3S{-}Au_{adatom}{-}SCH_3$ staple motif on Au(111). Only the topmost surface layer is shown. Au_{adatom}, yellow; other Au, red; S, blue; C, grey; H, white.

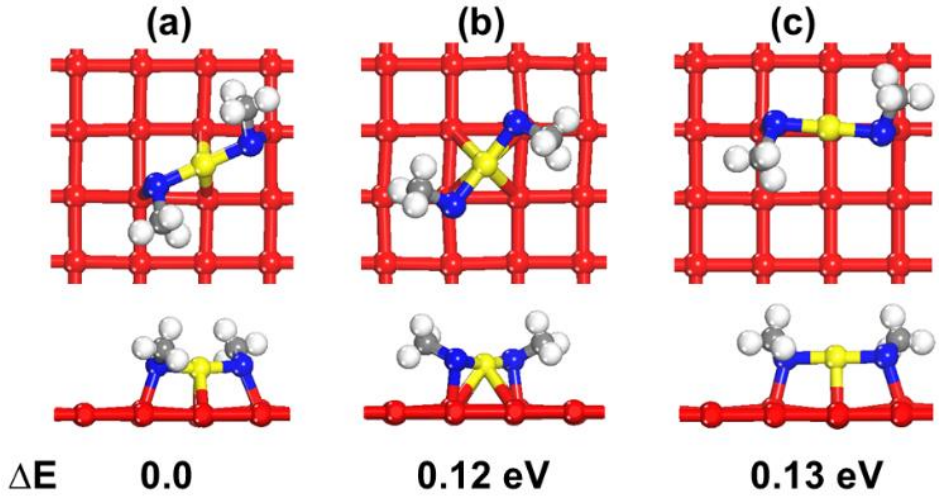

Figure 5.3. Top (upper panel) and side (lower panel) views of the optimized structures for the staple motifs on Au(100). (a) Au_{adatom} at the bridge site; (b) Au_{adatom} at the hollow site; (c) Au_{adatom} at the top site. Differences of the total energies based on four layers of slabs in (4 × 4) lateral cells are listed. Only the topmost surface layer is shown. Au_{adatom}, yellow; other Au, red; S, blue; C, grey; H, white.

We next examine the staple motif ($CH_3S{-}Au_{adatom}{-}SCH_3$) on Au surfaces. Figure 5.2 shows the optimized structure of the most stable form of the staple motif on Au(111).[39] We find three types of staple motifs on Au(100) of comparable energy (Figure 5.3). In the most stable structure (Figure 5.3a), the Au adatom is at the bridge site and the staple motif lays diagonally across two neighboring Au squares. For the second type (Figure 5.3b), the Au adatom is at the hollow site, and the staple motif lays diagonally across one

Au square. In the third type (Figure 5.3c), the Au adatom is at the top site and the staple motif lays on top of the long edge of two neighboring Au squares. On Au(110) we explored five types of staple motifs (Figure 5.4). The first three (Figure 5.4a-c) are close in energy. In the most stable structure (Figure 5.4a), the Au adatom is at the top site and the staple motif lays on top of two neighboring short Au-Au edges. In the second type (Figure 5.4b), the Au adatom is at the hollow site and the staple motif lays diagonally cross the Au rectangle. In the third type (Figure 5.4c), the Au adatom is at the long-bridge site and the staple motif lays diagonally across two neighboring Au rectangles sharing the long edge.

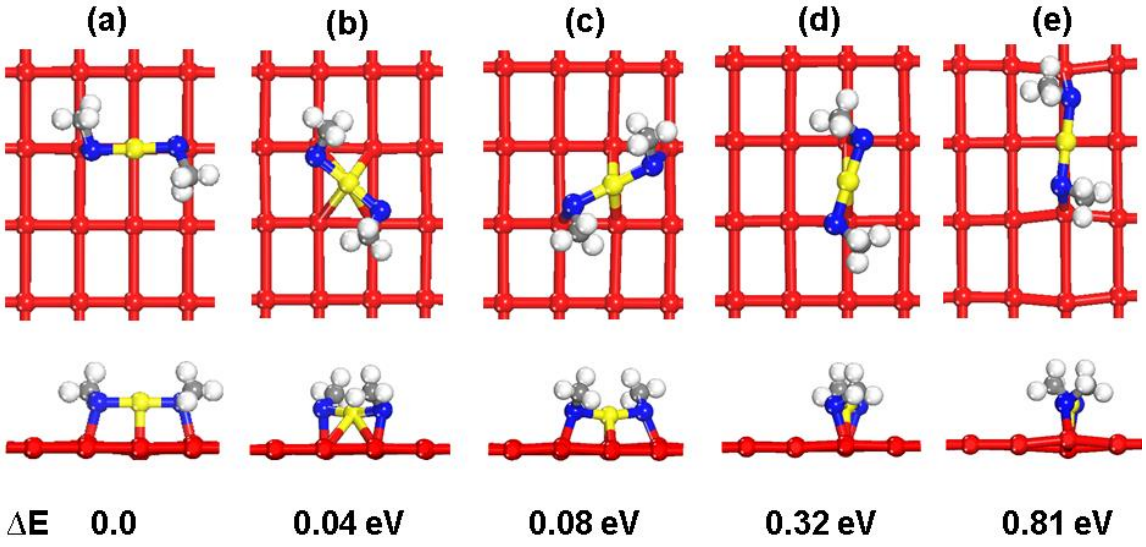

Figure 5.4. Top (upper panel) and side (lower panel) views of the optimized structures for the staple motifs on Au(110). (a) and (e) Au_{adatom} at the top site; (b) Au_{adatom} at the rectangular hollow site; (c) and (d) Au_{adatom} at the long bridge site. Differences of the total energies based on six layers of slabs in (3 × 4) lateral cells are listed. Only the topmost surface layer is shown. Au_{adatom}, yellow; other Au, red; S, blue; C, grey; H, white.

Figure 5.5 compares the binding energy per thiolate for the most stable modes of the bridging and staple motifs on the three Au surfaces. One can see that although the staple motif is preferred on Au(111), the bridging motif is preferred on Au(100) and Au(110). Clearly, the binding mode of the thiolate on Au is surface sensitive. From Au(111) to Au(100) to Au(110), the thiolate group binding stronger with Au for both the staple motif and the bridging motif, but apparently the increase is more dramatic for the bridging motif, especially from Au(111) to Au(100). This is the key underlying reason for the surface sensitivity of the binding motif.

To understand the increasing binding energies for the bridging motif, Table 5.4 lists the Au-S distance and the partial charge on Au that binds to S, together with the Au-Au coordination number of the different surfaces. One can see that the increasing binding energies from (111) to (100) to (110) correlate well with the shortening Au-S distance and the increasing charge transfer from S to Au. This trend can be well explained by the coordination numbers of the surface Au atoms, which decreases from 9 to 8 to 7 for Au(111), Au(100), and Au(110), respectively. Low-coordinate Au atoms are more active and therefore have stronger interactions with the thiolate group; and more so for the bridging thiolate than for the thiolate in the staple motif.

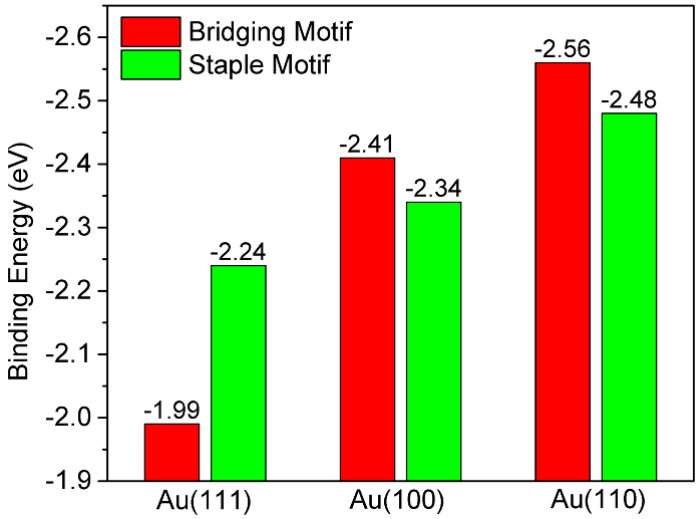

Figure 5.5. Comparison of binding energies per MT for the most stable modes of the bridging and staple motifs on the three Au surfaces. The coverages of each motif on Au(111), Au(100), and Au(110) surfaces are 1/16 ML, 1/16 ML, and 1/12 ML, respectively.

To further confirm the binding mode of the thiolate on Au(100), we studied SAMs on Au(100) with bridging and staple motifs. As shown in Figure 5.6, the sulfur overlayer has a coverage of 50%, and the overall patterning symmetry is c(2×2). For the bridging motif, one thiolate covers two Au atoms at the bridging site (Figure 5.6a), while for the staple motif, with the Au adatom at the bridge site, two thiolates cover diagonally across two neighboring Au squares (Figure 5.6b). In this case, we find that the binding energies per thiolate of the bridging and staple motifs are -2.35 eV and -1.89 eV, respectively. Clearly, SAMs on Au(100) with the bridging motif are more stable than the staple motif. In addition, we replaced the MT with the experimental ligand 4-tert-butylbenzenethiolate (TBBT), and considered the van der Waals (vdW) interactions between the ligands. The same trend was found. With a coverage of 25%, the binding energy per TBBT of the bridging motif is -3.01 eV, which is 0.48 eV lower than the staple motif (-2.53 eV).

These all indicate that the bridging motif rather than the staple motif is preferred on Au(100). Of course, the thiolate family of ligands are rich and more than just TBBT. Because of the relatively small energetic difference between the bridging and staple motifs, one can expect that the substituent effects (such as electron-drawing with fluorinated thiols, water-soluble ones with –GSH, etc.) may affect the interfacial ligand bonding. We hope to further explore them in the future.

Table 5.4. Binding energies $\mathbf{E_b}$, Au-S bond lengths $\mathbf{r_{Au\text{-}S}}$, Bader charges on Au atoms bonded to S of bridging MT on Au(111), Au(100) and Au(110) surfaces. Coordination numbers of surface Au atoms C.N. (Au) for each surface are also listed.

	Au(111)	**Au(100)**	**Au(110)**
$r_{Au\text{-}S}$/Å	2.475	2.428	2.416
Bader charge (Au)/|e|	+0.049	+0.060	+0.068
C.N. (Au-Au)	9	8	7

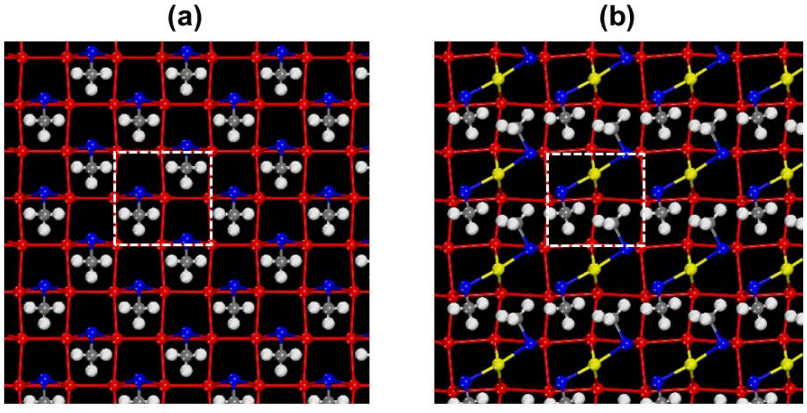

Figure 5.6. Top views of SAMs on Au(100) with the (a) bridging motif and (b) staple motif. The dotted-line box indicates the unit cell. Only the topmost surface layer is shown. Au_{adatom}, yellow; other Au, red; S, blue; C, grey; H, white.

5.2.2 Categorizing thiolate-protected gold nanoclusters

The surface sensitivity of the gold-thiolate interface as shown in Figure 5.5 can now explain the existence of the bridging motifs in some $Au_n(SR)_m$ clusters. Given this insight, it is necessary to view the existing $Au_n(SR)_m$ clusters from the geometry and facet of their cores. Our analysis of the surface sensitivity is based on the fcc geometry, while many $Au_n(SR)_m$ clusters have different core geometries. So we will first categorize all the existing thiolate-protected gold nanoclusters according to their interfacial motifs and then correlate them to the core geometry.

Table 5.5. Categorizing thiolate-protected gold nanoclusters into three groups: "no bridging", "ambiguous bridging", and "distinct bridging".

Category	cluster	kernel	protecting motifs
No bridging	$Au_{18}(SR)_{14}$	hcp-based Au_9	$Au_4(SR)_5 + Au_2(SR)_3 + 3\ Au(SR)_2$ [17]
	$Au_{20}(SR)_{16}$	bitetrahedral Au_7	$Au_8(SR)_8 + Au_3(SR)_4 + 2\ Au(SR)_2$ [18]
	$Au_{24}(SR)_{20}$	bitetrahedral Au_8	$4\ Au_4(SR)_5$ [21]
	$Au_{25}(SR)_{18}^{-1/0}$	Ic-based Au_{13}	$6\ Au_2(SR)_3$ [22-23]
	$Au_{30}(SR)_{18}$	hcp-based Au_{18}	$6\ Au_2(SR)_3$ [27]
	$Au_{38}(SR)_{24}$[a]	Ic-based Au_{23}	$6\ Au_2(SR)_3 + 3\ Au(SR)_2$ [31]
	$Au_{102}(SR)_{44}$	M-Dh-based Au_{79}	$2\ Au_2(SR)_3 + 19\ Au(SR)_2$ [35]
	$Au_{130}(SR)_{50}$	M-Dh-based Au_{105}	$25\ Au(SR)_2$ [36]
	$Au_{133}(SR)_{52}$	Ic-based Au_{107}	$26\ Au(SR)_2$ [37-38]
Ambiguous bridging	$Au_{23}(SR)_{16}^-$	fcc-based Au_{15}	$2\ Au_3(SR)_4 + 2\ Au(SR)_2 + 4\ SR$ [19]
	$Au_{28}(SR)_{20}$[b]	fcc-based Au_{20}	$4\ Au_2(SR)_3 + 8\ SR$ [24]
	$Au_{36}(SR)_{24}$	fcc-based Au_{28}	$4\ Au_2(SR)_3 + 12\ SR$ [28]
	$Au_{40}(SR)_{24}$	fcc-based Au_{34}	$6\ Au(SR)_2 + 12\ SR$ [33, 50]
	$Au_{44}(SR)_{28}$	fcc-based Au_{36}	$4\ Au_2(SR)_3 + 16\ SR$ [51]
	$Au_{52}(SR)_{32}$	fcc-based Au_{44}	$4\ Au_2(SR)_3 + 20\ SR$ [33, 51]
Distinct bridging	$Au_{92}(SR)_{44}$	fcc-based Au_{84}	$8\ Au(SR)_2 + 28\ SR$ [34]

[a] $Au_{38}(SR)_{24}$ has two isomers: Q and T,[31-32] and isomer Q is presented here. [b] $Au_{28}(SR)_{20}$ has two ligand-induced isomers: $Au_{28}(SPh\text{-}p\text{-}^tBu)_{20}$ and $Au_{28}(S\text{-}c\text{-}C_6H_{11})_{20}$,[24-25] and $Au_{28}(SPh\text{-}p\text{-}^tBu)_{20}$ is presented here.

We found that all the reported $Au_n(SR)_m$ clusters can be summarized into three groups based on their protecting motifs (Table 5.5): (1) no bridging, i.e., staple motifs only; (2) ambiguous bridging, i.e., having bridging motifs but ambiguous bridging only, in addition to staple motifs; (3) distinct bridging, i.e., having distinct bridging motifs, in

addition to staple motifs and ambiguous bridging (if any). Table 5.5 shows that $Au_n(SR)_m$ clusters with non-fcc cores, including icosahedral (Ic), Marks decahedral (M-Dh), and hexagonal close packing (hcp), have staple motifs only and no bridging thiolates at the interface. A common structural feature of these cores is the dominance of the Au_3 triangles on the core surface. Similar to Au(111), these triangles prefer the staple motif. This may be why only staple motifs exist at the interface of these clusters with non-fcc cores. Figure 5.7a shows the typical structure of "no bridging": $Au_{38}(SR)_{24}$.[31] As one can see, the core surface only exhibits Au_3 triangles, and it is simply protected by the staple motifs.

Table 5.5 also shows that for the clusters with bridging motifs, either ambiguous or distinct bridging, they all have fcc kernels. This can be due to the fact that fcc-based kernels have exposing (100) facets and a clear confirmation of the surface sensitivity that we found for bulk fcc Au as shown in Figure 5.5. Especially for the magic series $Au_{28}(SR)_{20}$, $Au_{36}(SR)_{24}$, $Au_{44}(SR)_{28}$ and $Au_{52}(SR)_{32}$ reported by Jin group, they all have 4 Au_5 or Au_6 {111} facets, and have 8, 12, 16, and 20 Au_4 {100} squares, respectively. Significantly, the surface-protecting modes of these clusters obey the same rules, i.e., each {111} facet is protected by one dimeric staple motif, and each {100} square is protected by one bridging motif.[50] Similarly for $Au_{23}(SR)_{16}^-$ and $Au_{40}(SR)_{24}$, the bridging motifs all appear over the squares. These structures are called ambiguous bridging because the bridging thiolates can be viewed alternatively as part of dimeric staple motifs with a different core geometry. Figure 5.7b shows the typical structure of "ambiguous bridging": $Au_{36}(SR)_{24}$.[28] The ambiguous bridging motifs are colored with blue. As one

can see, these 12 ambiguous bridging motifs can be viewed alternatively as 4 dimeric staple motifs. But our finding of the surface sensitivity supports the view from the bridging thiolate where the core takes a compact fcc geometry, instead of a less ordered and hard-to-describe core as in the view from the staple motif. A previous study calculated the Bader charges on gold atoms of the thiolate-protected $Au_{28}(SMe)_{20}$ cluster, and found that gold atoms related to the ambiguous motifs have lower Bader charges than the core atoms.[47] Therefore, chemically speaking, these ambiguous motifs are more like staple motifs. However, here we emphasizes more on the structure and energetic perspectives, which together with the chemical view offer a more complete picture. In the case of $Au_{92}(SR)_{44}$, distinct bridging thiolates are observed on the planar (100) facets because these bridging motifs cannot be viewed as part of the staple motifs. In addition to the distinct bridging thiolates on the facets, there are ambiguous bridging thiolates at the edges and corners of the tetragonal $Au_{92}(TBBT)_{44}$. This has previously been explained by the boundary effect, i.e., the corner-site can be viewed as protected by −S–Au–S–Au–S– dimeric staple motif, which is actually assembled from three simple bridging thiolates at the three joining facets. Similarly, the edge is protected by −S–Au–S– monomeric staple motifs, and they can be decomposed into two bridging thiolates at the two connecting facets.[34] Figure 5.7c shows the structure of the only "distinct bridging": $Au_{92}(SR)_{44}$. Although only one member belongs to this type, we think that there will be more structures in this type to be discovered. Below we present predictions of possible type-3 structures.

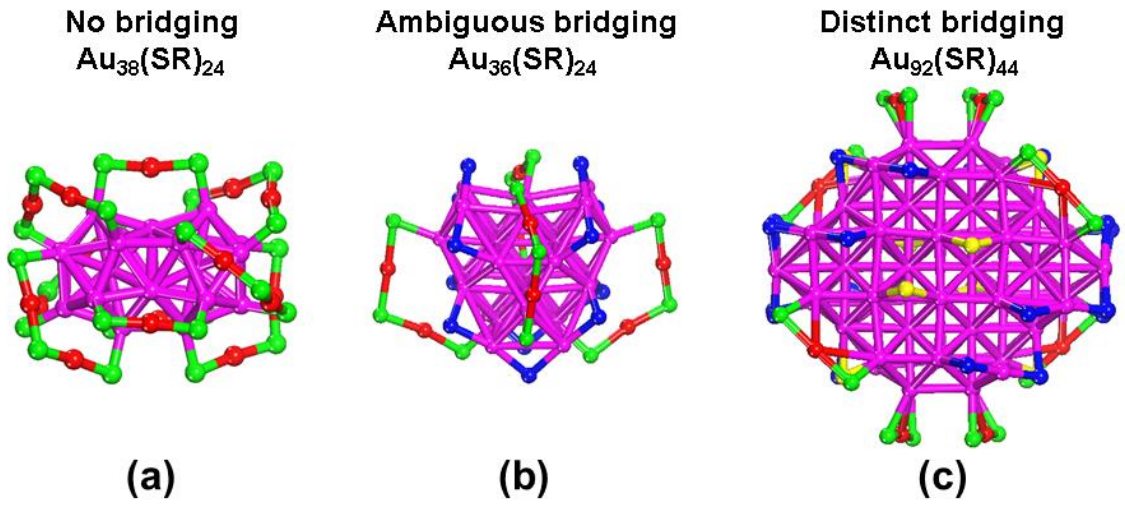

Figure 5.7. Typical structures for the three types of $Au_n(SR)_m$ clusters: (a) "no bridging": $Au_{38}(SR)_{24}$, isomer Q; (b) "ambiguous bridging": $Au_{36}(SR)_{24}$; (c) "distinct bridging": $Au_{92}(SR)_{44}$. Carbon tails are omitted for clarity. Au (kernel), magenta; Au (staple), red; S (staple), green; S (ambiguous bridging), blue; S (distinct bridging), yellow.

5.3 Implications for structure predictions based on the surface sensitivity

Based on the facet sensitivity, we predict the protecting motifs of fcc gold nanoparticles smaller than 3 nm. "Geometrically ideal" shapes of fcc nanoparticles include cube (terminated completely by {100} surfaces), truncated cube, cuboctahedron, truncated octahedron, and octahedron (terminated completely by {111} surfaces). Here we choose five fcc gold nanoparticles with different shapes, namely, cubic Au_{108}, truncated cubic Au_{171}, cuboctahedral Au_{147}, truncated octahedral Au_{140}, and octahedral Au_{146},[51] and predict their protecting motifs with the facet sensitivity. As shown in Figure 5.8, we predict that cores such as cubic Au_{108}, truncated cubic Au_{171}, and cuboctahedral Au_{147} cores will have distinct bridging motifs on their surfaces.

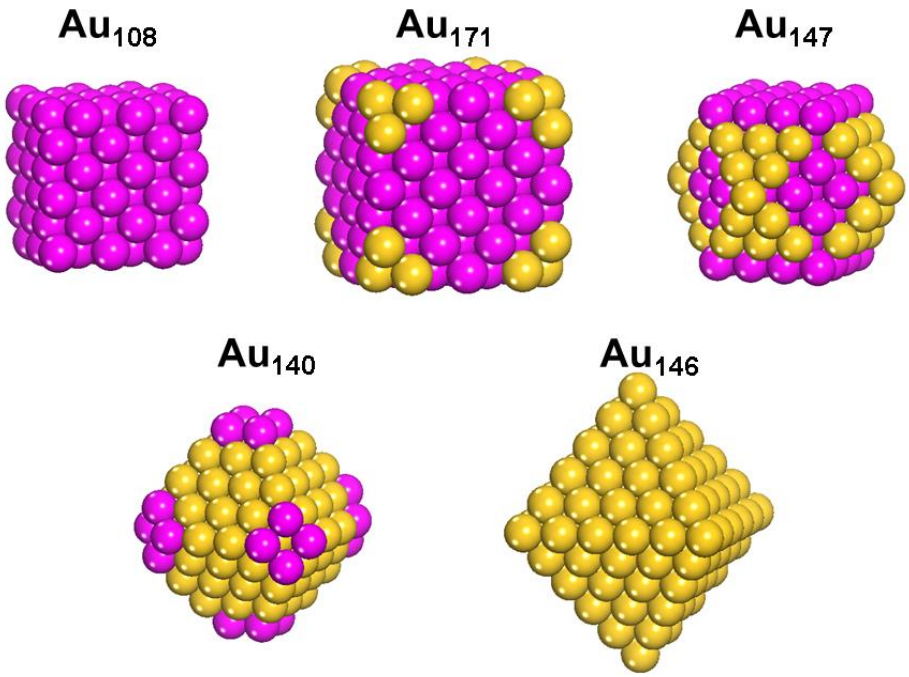

Figure 5.8. Five fcc gold nanoparticles with different shapes, namely, cubic Au_{108}, truncated cubic Au_{171}, cuboctahedral Au_{147}, truncated octahedral Au_{140}, and octahedral Au_{146}. The exposing (100) facets are colored with magenta, while the exposing (111) facets are colored with yellow.

The surface sensitivity we found also has an important implication for a recently proposed structure of $Au_{144}(SR)_{60}$. From their pair-distribution function (PDF) experiment and analysis, Ackerson et al. found that the $Au_{144}(SR)_{60}$ cluster can exist in two different polymorphs; they proposed a decahedral Au_{114} core (Figure 5.9) that is different from the popular model of the icosahedral Au_{114} core.[52-53] The proposed Au_{114} core of $Au_{144}(SR)_{60}$ exhibit five (111) facets at the top and another five at the bottom, as well as five (100) facets on the waist. Our finding of the facet sensitivity of the thiolate-gold interface suggests that the planar (100) facets should be protected by the bridging motifs instead of the staple motifs. Therefore, structure prediction of the new $Au_{144}(SR)_{60}$

polymorph based on the decahedral Au_{114} core needs to take into account both the bridging thiolates in addition to the staple motifs.

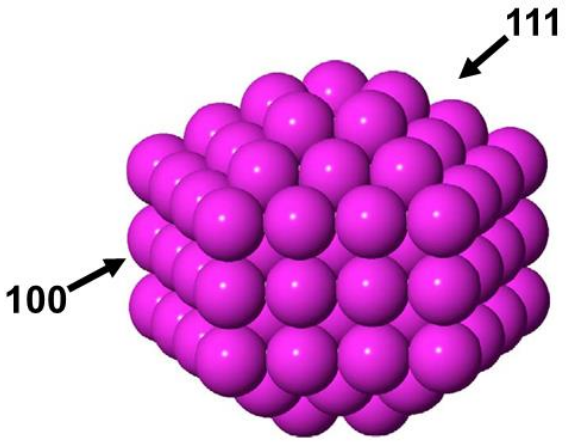

Figure 5.9. The proposed Au_{114} kernel of $Au_{144}(SR)_{60}$.

5.4 Conclusions

To shed light on the bridging motifs at the interface of the thiolate-protected gold nanoclusters, we have studied the facet or surface sensitivity of the thiolate-gold interface with three low-Miller-index surfaces of gold, including Au(111), Au(100), and Au(110), by using periodic DFT. We find that the interfacial structures of thiolates on gold are surface sensitive: while the staple motif (-RS-Au-SR-) is preferred on Au(111), the bridging motif (-RS-) is preferred on Au(100) and Au(110). This surface sensitivity is closely related to the coordination number of the surface Au atom on the different surfaces. With this surface sensitivity, we categorize the structure-known $Au_n(SR)_m$ clusters into three groups: (1) no bridging; (2) ambiguous bridging; (3) distinct bridging. We further employ the surface sensitivity of the thiolate-Au interface to predict the protecting motifs of face-centered cubic (fcc) gold nanoparticles (smaller than 3 nm) of

different shapes. Our study provide a unifying view of the $Au_n(SR)_m$ structures and guidelines for structure predictions of the larger thiolate-protected gold nanoclusters of a fcc core.

References

1. Alvarez, M. M.; Khoury, J. T.; Schaaff, T. G.; Shafigullin, M. N.; Vezmar, I.; Whetten, R. L., Optical Absorption Spectra of Nanocrystal Gold Molecules. *J. Phys. Chem. B* **1997**, *101*, 3706-3712.

2. Chen, S.; Ingram, R. S.; Hostetler, M. J.; Pietron, J. J.; Murray, R. W.; Schaaff, T. G.; Khoury, J. T.; Alvarez, M. M.; Whetten, R. L., Gold Nanoelectrodes of Varied Size: Transition to Molecule-Like Charging. *Science* **1998**, *280*, 2098-2101.

3. Negishi, Y.; Nobusada, K.; Tsukuda, T., Glutathione-Protected Gold Clusters Revisited: Bridging the Gap between Gold (I)-Thiolate Complexes and Thiolate-Protected Gold Nanocrystals. *J. Am. Chem. Soc.* **2005**, *127*, 5261-5270.

4. Hashmi, A. S. K.; Hutchings, G. J., Gold Catalysis. *Angew. Chem. Int. Ed.* **2006**, *45*, 7896-7936.

5. Hakkinen, H., The Gold-Sulfur Interface at the Nanoscale. *Nat. Chem.* **2012**, *4*, 443-455.

6. Tsukuda, T., Toward an Atomic-Level Understanding of Size-Specific Properties of Protected and Stabilized Gold Clusters. *Bull. Chem. Soc. Jpn.* **2012**, *85*, 151-168.

7. Pei, Y.; Zeng, X. C., Investigating the Structural Evolution of Thiolate Protected Gold Clusters from First-Principles. *Nanoscale* **2012**, *4*, 4054-4072.

8. Qian, H.; Zhu, M.; Wu, Z.; Jin, R., Quantum Sized Gold Nanoclusters with Atomic Precision. *Acc. Chem. Res.* **2012**, *45*, 1470-1479.

9. Bürgi, T., Properties of the Gold–Sulphur Interface: From Self-Assembled Monolayers to Clusters. *Nanoscale* **2015**, *7*, 15553-15567.

10. Jin, R.; Zeng, C.; Zhou, M.; Chen, Y., Atomically Precise Colloidal Metal Nanoclusters and Nanoparticles: Fundamentals and Opportunities. *Chem. Rev.* **2016**, *116*, 10346-10413.

11. Murray, R. W., Nanoelectrochemistry: Metal Nanoparticles, Nanoelectrodes, and Nanopores. *Chem. Rev.* **2008**, *108*, 2688-2720.

12. Jin, R., Quantum Sized, Thiolate-Protected Gold Nanoclusters. *Nanoscale* **2010**, *2*, 343-362.

13. Ackerson, C. J.; Powell, R. D.; Hainfeld, J. F., Site-Specific Biomolecule Labeling with Gold Clusters. *Methods enzymol.* **2010**, *481*, 195-230.

14. Maity, P.; Xie, S.; Yamauchi, M.; Tsukuda, T., Stabilized Gold Clusters: From Isolation toward Controlled Synthesis. *Nanoscale* **2012**, *4*, 4027-4037.

15. Li, G.; Jin, R., Atomically Precise Gold Nanoclusters as New Model Catalysts. *Acc. Chem. Res.* **2013**, *46*, 1749-1758.

16. Jin, R., Atomically Precise Metal Nanoclusters: Stable Sizes and Optical Properties. *Nanoscale* **2015**, *7*, 1549-1565.

17. Das, A.; Liu, C.; Byun, H. Y.; Nobusada, K.; Zhao, S.; Rosi, N.; Jin, R., Structure Determination of $[Au_{18}(SR)_{14}]$. *Angew. Chem. Int. Ed.* **2015**, *54*, 3140-3144.

18. Zeng, C.; Liu, C.; Chen, Y.; Rosi, N. L.; Jin, R., Gold-Thiolate Ring as a Protecting Motif in the $Au_{20}(SR)_{16}$ Nanocluster and Implications. *J. Am. Chem. Soc.* **2014**, *136*, 11922-11925.

19. Das, A.; Li, T.; Nobusada, K.; Zeng, C.; Rosi, N. L.; Jin, R., Nonsuperatomic $[Au_{23}(SC_6H_{11})_{16}]^-$ Nanocluster Featuring Bipyramidal Au_{15} Kernel and Trimeric $Au_3(SR)_4$ Motif. *J. Am. Chem. Soc.* **2013**, *135*, 18264-18267.

20. Crasto, D.; Barcaro, G.; Stener, M.; Sementa, L.; Fortunelli, A.; Dass, A., $Au_{24}(Sadm)_{16}$ Nanomolecules: X-Ray Crystal Structure, Theoretical Analysis, Adaptability of Adamantane Ligands to Form $Au_{23}(SAdm)_{16}$ and $Au_{25}(SAdm)_{16}$, and Its Relation to $Au_{25}(SR)_{18}$. *J. Am. Chem. Soc.* **2014**, *136*, 14933-14940.

21. Das, A.; Li, T.; Li, G.; Nobusada, K.; Zeng, C.; Rosi, N. L.; Jin, R., Crystal Structure and Electronic Properties of a Thiolate-Protected Au_{24} Nanocluster. *Nanoscale* **2014**, *6*, 6458-6462.

22. Zhu, M.; Aikens, C. M.; Hollander, F. J.; Schatz, G. C.; Jin, R., Correlating the Crystal Structure of a Thiol-Protected Au_{25} Cluster and Optical Properties. *J. Am. Chem. Soc.* **2008**, *130*, 5883-5885.

23. Heaven, M. W.; Dass, A.; White, P. S.; Holt, K. M.; Murray, R. W., Crystal Structure of the Gold Nanoparticle $[N(C_8H_{17})_4][Au_{25}(SCH_2CH_2Ph)_{18}]$. *J. Am. Chem. Soc.* **2008**, *130*, 3754-3755.

24. Zeng, C.; Li, T.; Das, A.; Rosi, N. L.; Jin, R., Chiral Structure of Thiolate-Protected 28-Gold-Atom Nanocluster Determined by X-Ray Crystallography. *J. Am. Chem. Soc.* **2013**, *135*, 10011-10013.

25. Chen, Y.; Liu, C.; Tang, Q.; Zeng, C.; Higaki, T.; Das, A.; Jiang, D. E.; Rosi, N. L.; Jin, R., Isomerism in $Au_{28}(SR)_{20}$ Nanocluster and Stable Structures. *J. Am. Chem. Soc.* **2016**, *138*, 1482-1485.

26. Crasto, D.; Malola, S.; Brosofsky, G.; Dass, A.; Hakkinen, H., Single Crystal Xrd Structure and Theoretical Analysis of the Chiral $Au_{30}s(S\text{-}t\text{-}Bu)_{18}$ Cluster. *J. Am. Chem. Soc.* **2014**, *136*, 5000-5005.

27. Higaki, T.; Liu, C.; Zeng, C.; Jin, R.; Chen, Y.; Rosi, N. L.; Jin, R., Controlling the Atomic Structure of Au_{30} Nanoclusters by a Ligand-Based Strategy. *Angew. Chem. Int. Ed.* **2016**, *55*, 6694-6697.

28. Zeng, C.; Qian, H.; Li, T.; Li, G.; Rosi, N. L.; Yoon, B.; Barnett, R. N.; Whetten, R. L.; Landman, U.; Jin, R., Total Structure and Electronic Properties of the Gold Nanocrystal $Au_{36}(SR)_{24}$. *Angew. Chem. Int. Ed.* **2012**, *124*, 13291-13295.

29. Das, A.; Liu, C.; Zeng, C.; Li, G.; Li, T.; Rosi, N. L.; Jin, R., Cyclopentanethiolato-Protected $Au_{36}(SC_5H_9)_{24}$ Nanocluster: Crystal Structure and Implications for the Steric and Electronic Effects of Ligand. *J. Phys. Chem. A* **2014**, *118*, 8264-8269.

30. Nimmala, P. R.; Knoppe, S.; Jupally, V. R.; Delcamp, J. H.; Aikens, C. M.; Dass, A., $Au_{36}(SPh)_{24}$ Nanomolecules: X-Ray Crystal Structure, Optical Spectroscopy, Electrochemistry, and Theoretical Analysis. *J. Phys. Chem. B* **2014**, *118*, 14157-14167.

31. Qian, H.; Eckenhoff, W. T.; Zhu, Y.; Pintauer, T.; Jin, R., Total Structure Determination of Thiolate-Protected Au_{38} Nanoparticles. *J. Am. Chem. Soc.* **2010**, *132*, 8280-8281.

32. Tian, S.; Li, Y. Z.; Li, M. B.; Yuan, J.; Yang, J.; Wu, Z.; Jin, R., Structural Isomerism in Gold Nanoparticles Revealed by X-Ray Crystallography. *Nat. Commun.* **2015**, *6*, 8667.

33. Zeng, C.; Chen, Y.; Liu, C.; Nobusada, K.; Rosi, N. L.; Jin, R., Gold Tetrahedra Coil Up: Kekulé-Like and Double Helical Superstructures. *Sci. Adv.* **2015**, *1*, e1500425.

34. Zeng, C.; Liu, C.; Chen, Y.; Rosi, N. L.; Jin, R., Atomic Structure of Self-Assembled Monolayer of Thiolates on a Tetragonal Au_{92} Nanocrystal. *J. Am. Chem. Soc.* **2016**, *138*, 8710-8713.

35. Jadzinsky, P. D.; Calero, G.; Ackerson, C. J.; Bushnell, D. A.; Kornberg, R. D., Structure of a Thiol Monolayer-Protected Gold Nanoparticle at 1.1 Å Resolution. *Science* **2007**, *318*, 430-433.

36. Chen, Y.; Zeng, C.; Liu, C.; Kirschbaum, K.; Gayathri, C.; Gil, R. R.; Rosi, N. L.; Jin, R., Crystal Structure of Barrel-Shaped Chiral Au_{130}(*p*-MBT)$_{50}$ Nanocluster. *J. Am. Chem. Soc.* **2015**, *137*, 10076-10079.

37. Dass, A.; Theivendran, S.; Nimmala, P. R.; Kumara, C.; Jupally, V. R.; Fortunelli, A.; Sementa, L.; Barcaro, G.; Zuo, X.; Noll, B. C., Au_{133}(SPh-*t*Bu)$_{52}$ Nanomolecules: X-Ray Crystallography, Optical, Electrochemical, and Theoretical Analysis. *J. Am. Chem. Soc.* **2015**, *137*, 4610-4613.

38. Zeng, C.; Chen, Y.; Kirschbaum, K.; Appavoo, K.; Sfeir, M. Y.; Jin, R., Structural Patterns at All Scales in a Nonmetallic Chiral $Au_{133}(SR)_{52}$ Nanoparticle. *Sci. Adv.* **2015**, *1*, e1500045.

39. Maksymovych, P.; Sorescu, D. C.; Yates, J. T., Jr., Gold-Adatom-Mediated Bonding in Self-Assembled Short-Chain Alkanethiolate Species on the Au(111) Surface. *Phys. Rev. Lett.* **2006**, *97*, 146103.

40. Cossaro, A.; Mazzarello, R.; Rousseau, R.; Casalis, L.; Verdini, A.; Kohlmeyer, A.; Floreano, L.; Scandolo, S.; Morgante, A.; Klein, M., X-Ray Diffraction and Computation Yield the Structure of Alkanethiols on Gold (111). *Science* **2008**, *321*, 943-946.

41. Grönbeck, H.; Häkkinen, H.; Whetten, R. L., Gold− Thiolate Complexes Form a Unique C (4× 2) Structure on Au (111). *J. Phys. Chem. C* **2008**, *112*, 15940-15942.

42. Jiang, D. E.; Tiago, M. L.; Luo, W.; Dai, S., The "Staple" Motif: A Key to Stability of Thiolate-Protected Gold Nanoclusters. *J. Am. Chem. Soc.* **2008**, *130*, 2777-2779.

43. Akola, J.; Walter, M.; Whetten, R. L.; Häkkinen, H.; Grönbeck, H., On the Structure of Thiolate-Protected Au_{25}. *J. Am. Chem. Soc.* **2008**, *130*, 3756-3757.

44. Pei, Y.; Gao, Y.; Zeng, X. C., Structural Prediction of Thiolate-Protected Au_{38}: A Face-Fused Bi-Icosahedral Au Core. *J. Am. Chem. Soc.* **2008**, *130*, 7830-7832.

45. Lopez-Acevedo, O.; Tsunoyama, H.; Tsukuda, T.; Aikens, C. M., Chirality and Electronic Structure of the Thiolate-Protected Au_{38} Nanocluster. *J. Am. Chem. Soc.* **2010**, *132*, 8210-8218.

46. Jiang, D. E., The Expanding Universe of Thiolated Gold Nanoclusters and Beyond. *Nanoscale* **2013**, *5*, 7149-7160.

47. Knoppe, S.; Malola, S.; Lehtovaara, L.; Burgi, T.; Hakkinen, H., Electronic Structure and Optical Properties of the Thiolate-Protected $Au_{28}(SMe)_{20}$ Cluster. *J. Phys. Chem. A* **2013**, *117*, 10526-10533.

48. Demir, F.; Kirczenow, G., Communication: Identification of the Molecule–Metal Bonding Geometries of Molecular Nanowires. *J. Chem. Phys.* **2011**, *134*, 121103.

49. Demir, F.; Kirczenow, G., Identification of the Atomic Scale Structures of the Gold-Thiol Interfaces of Molecular Nanowires by Inelastic Tunneling Spectroscopy. *J. Chem. Phys.* **2012**, *136*, 014703.

50. Zeng, C.; Chen, Y.; Iida, K.; Nobusada, K.; Kirschbaum, K.; Lambright, K. J.; Jin, R., Gold Quantum Boxes: On the Periodicities and the Quantum Confinement in the Au_{28}, Au_{36}, Au_{44}, and Au_{52} Magic Series. *J. Am. Chem. Soc.* **2016**, *138*, 3950-3953.

51. Barnard, A. S.; Curtiss, L. A., Predicting the Shape and Structure of Face-Centered Cubic Gold Nanocrystals Smaller Than 3 nm. *ChemPhysChem* **2006**, *7*, 1544-1553.

52. Jensen, K. M.; Juhas, P.; Tofanelli, M. A.; Heinecke, C. L.; Vaughan, G.; Ackerson, C. J.; Billinge, S. J., Polymorphism in Magic-Sized $Au_{144}(SR)_{60}$ Clusters. *Nat. Commun.* **2016**, *7*, 11859.

53. Lopez-Acevedo, O.; Akola, J.; Whetten, R. L.; Grönbeck, H.; Häkkinen, H., Structure and Bonding in the Ubiquitous Icosahedral Metallic Gold Cluster $Au_{144}(SR)_{60}$. *J. Phys. Chem. C* **2009**, *113*, 5035-5038.

Chapter 6

Metallic Hydrogen in Atomically Precise Gold Nanoclusters

Abstract

Hydrogen-metal interaction is the foundation of many technologies and processes. But it remains unknown how hydrogen behaves in atomically precise gold nanoclusters even though they have been used in hydrogenation catalysis and water splitting. Herein we investigate how hydrogen interacts with $[Au_{25}(SR)_{18}]^q$ clusters and monoatom-doped bimetallic $[M_1Au_{24}(SR)_{18}]^q$ clusters (M=Pt, Pd, Ag, Cu, Hg, Cd) from first principles. We find that hydrogen behaves as a metal in these clusters and contributes its 1s electron to the superatomic free-electron count. This opposite behavior to the hydride in Cu and Ag clusters allows the small-sized hydrogen to interstitially dope the gold clusters and tune their superatomic electronic structure. The doping energetics shows that when an 8-electron superatom is formed after H doping, the binding energy of H is much stronger, while binding of H with an already 8-electron superatom is much weaker. Indeed, frontier orbitals and the HOMO-LUMO gaps of $[Au_{25}H_1(SR)_{18}]^0$, $[Au_{25}H_2(SR)_{18}]^+$, $[PtAu_{24}H_2(SR)_{18}]^0$, $[PdAu_{24}H_2(SR)_{18}]^0$, $[AgAu_{24}H(SR)_{18}]^0$, and $[CuAu_{24}H_1(SR)_{18}]^0$ all have very similar features, because they are all 8-electron superatoms. By calculating the Gibbs free energies of hydrogen adsorption, we predict that $PtAu_{24}(SR)_{18}$, $PdAu_{24}(SR)_{18}$, and center-doped $CuAu_{24}(SR)_{18}$ can be good electrocatalysts for hydrogen-evolution reaction.

6.1 Introduction

The behavior of hydrogen in metals has been of great interest for many decades.[1-4] Metal-hydrogen systems are widely utilized in energy-storage systems, sensor applications, as well as catalysis.[5] The small size of hydrogen atom permits dense hydrogen packing in metal hosts that have a high affinity for hydrogen storage. The high diffusivity of hydrogen in metals also endows nanoscaled metal-hydrogen systems interesting possibilities for sensor applications.[6-7] Moreover, reactions with hydrogen on metals are important in catalysis, particularly in hydrogenation, water splitting, and hydrogen fuel cells.[8-10]

In contrast with bulk metal hydrides, the structures of H-metal nanoclusters can provide insight from a molecular perspective of how hydrogen interacts with metals and how the magic sizes or superatoms evolve.[11] The hydride ligand (H^-) has been used in the synthesis of ligand-protected copper or silver nanoclusters.[12-22] Especially for the copper clusters, a series of air- and moisture-stable copper hydride clusters ranging from Cu_7H to $Cu_{32}H_{20}$ were successfully synthesized and structure-determined.[23] In 2015, Hayton et al. reported the isolation and structural characterization of $[Cu_{25}H_{22}(PPh_3)_{12}]Cl$, the first copper hydride nanocluster with partial Cu(0) character.[18] By controlled growth from this Cu_{25} hydride nanocluster, they then reported the synthesis and identification of $[Cu_{29}Cl_4H_{22}(Ph_2phen)_{12}]Cl$, which is the largest copper superatom known to date (superatomic electron count = 2).[22] In addition to the many successes of copper hydride clusters, Bakr et al. recently successfully synthesized a new class of hydride-rich,

atomically precise sliver nanoclusters, including Ag_{18}, Ag_{25}, and Ag_{26}, with phosphine as co-ligands.[21]

In contrast to Cu and Ag, hydrogen has not been observed in the ligand-protected gold nanoclusters. Among the reported ligand-protected gold nanoclusters, $Au_{25}(SR)_{18}$ is one of the most extensively studied systems.[24-35] Tsukuda and coworkers first identified $Au_{25}(SR)_{18}$ in 2005;[36] then, Murray and Jin groups solved its structure.[25-26] The stability of the anionic $[Au_{25}(SR)_{18}]^{-}$ cluster can be explained by the superatom complex concept: its eight free electrons occupy a complete electron shell of the $(1S)^2(1P)^6$ configuration.[11] Considerable efforts have also been pursued to dope $Au_{25}(SR)_{18}$ with other atoms such as Pt, Pd, Ag, Cu, Hg, and Cd.[37-50]

Recently, it has been showed that both $Au_{25}(SR)_{18}$ and $PtAu_{24}(SR)_{18}$ exhibit high hydrogen-evolution-reaction (HER) activity; more interestingly, the latter's activity is much higher than the former and is among the most active molecular catalysts for HER.[51] Given the tremendous progress in ligand-protected gold nanoclusters and the potential of using them as electrocatalysts for water splitting, it is of great interest to investigate the behavior of hydrogen in ligand-protected gold nanoclusters systematically in terms of cluster charge states, different dopants, and superatomic electronic structure. To this end we study hydrogen adsorption on $[Au_{25}(SR)_{18}]^q$ clusters (q=-1, 0, +1) and mono-doped bimetallic $[MAu_{24}(SR)_{18}]^q$ clusters (M=Pt, Pd, Ag, Cu, Hg, Cd, and q=-2, -1, 0) by first-principles density functional theory (DFT). We especially focus on the binding sites and energetics of H in the clusters and the changes to their superatomic free-electron count.

We further evaluate the Gibbs free energies of H adsorption to predict the HER activities of these clusters.

6.2 Results and discussion

6.2.1 Hydrogen in $[Au_{25}(SR)_{18}]^q$ clusters (q=-1, 0, +1).

We first start with the $[Au_{25}(SR)_{18}]^q$ clusters, the most studied atomically precise, ligand-protected metal clusters. Table 6.1 lists the adsorption energies of sequential adsorption of hydrogen atoms on $[Au_{25}(SR)_{18}]^q$ clusters (q=-1, 0, +1) relative to atomic hydrogen. One can see that $[Au_{25}(SR)_{18}]^-$ has an adsorption energy of -1.18 eV, while $[Au_{25}(SR)_{18}]^0$ and $[Au_{25}(SR)_{18}]^+$ have adsorption energies of -2.04 eV and -1.81 eV, respectively. In other words, H binds strongest in $[Au_{25}(SR)_{18}]^0$, followed by $[Au_{25}(SR)_{18}]^+$. H binding is the weakest with $[Au_{25}(SR)_{18}]^-$. Figure 6.1 shows the optimized structures of $[Au_{25}H(SR)_{18}]^-$, $[Au_{25}H(SR)_{18}]^0$, and $[Au_{25}H(SR)_{18}]^+$, which have optimized H-Au_{Center} distance at 3.049 Å, 1.979 Å, and 1.967 Å, respectively. Therefore, the charge state is a very important factor in affecting energetics and structure of hydrogen adsorption on gold nanoclusters.

Table 6.1. Free-electron count (n) of $[Au_{25}(SR)_{18}]^-$, $[Au_{25}(SR)_{18}]^0$, and $[Au_{25}(SR)_{18}]^+$ and their sequential adsorption energy (eV) for hydrogen: first, ΔE_{H1}; second, ΔE_{H2}; third, ΔE_{H3}. R=CH_3.

Cluster	n	ΔE_{H1}	ΔE_{H2}	ΔE_{H3}
$[Au_{25}(SR)_{18}]^-$	8	-1.18	--	--
$[Au_{25}(SR)_{18}]^0$	7	-2.04	-1.25	--
$[Au_{25}(SR)_{18}]^+$	6	-1.81	-1.98	-1.46

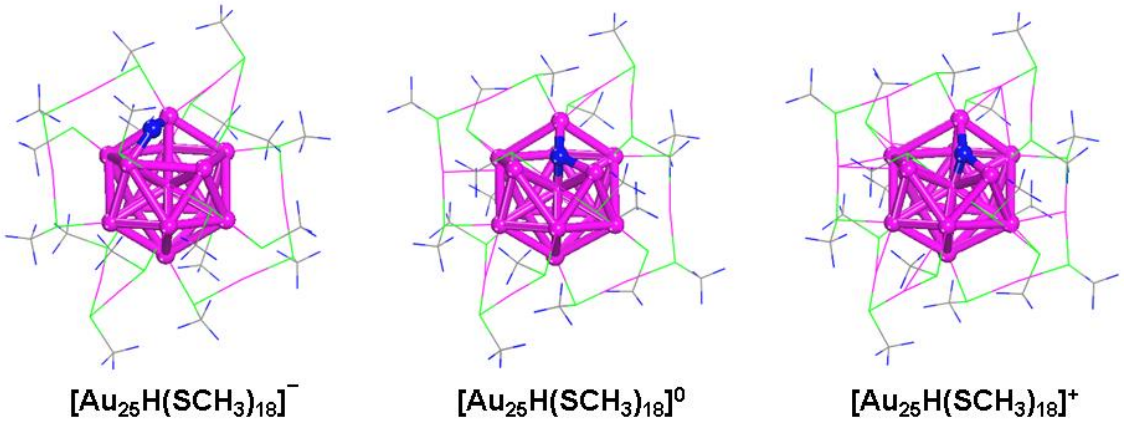

Figure 6.1. Optimized structures of $[Au_{25}H(SR)_{18}]^{-}$, $[Au_{25}H(SR)_{18}]^{0}$, and $[Au_{25}H(SR)_{18}]^{+}$. Protecting motifs are showed in line mode. R=CH_3. Au, magenta; H, blue; S, green; C, grey.

Adding more H to $[Au_{25}(SR)_{18}]^{0}$ and $[Au_{25}(SR)_{18}]^{+}$, we find that adsorption energy of the second H on $[Au_{25}(SR)_{18}]^{0}$ becomes weaker (-1.25 eV), close to that of the first H on $[Au_{25}H(SR)_{18}]^{-}$. However, for $[Au_{25}(SR)_{18}]^{+}$, one more H can be strongly adsorbed with an energy of -1.98 eV, but the adsorption energy of the third H becomes much weaker (-1.46 eV). To understand the significant differences in hydrogen adsorption energies on $[Au_{25}(SR)_{18}]^{q}$ clusters (q=-1, 0, +1), we calculated Bader charges on the adsorbed H. We find that Bader charges on H are close to zero (ranging from +0.034 to -0.004 |e|). This is in contrast with H in silver or copper nanoclusters, where charges on H are negative, for example, -0.51 ~ -0.67 |e| on hydrides in $[Cu_{20}H_{11}(S_2PH_2)_9]$.[15] This can be explained by the fact that H's electronegativity (2.2) is smaller than that of Au (2.54) but larger than that of Ag (1.93) or Cu (1.9). Therefore, H in ligand-protected gold clusters behaves like a metal, while H in ligand-protected sliver or copper clusters behaves like H^{-} or a ligand. In other words, H atoms in ligand-

protected gold clusters do not withdraw electrons from the metal core, but donate their electrons to the cluster. This insight has important implications in how hydrogen impacts the free-electron count and hence the superatomic electronic structure.

$[Au_{25}(SR)_{18}]^{-}$ is an 8-electron (8-e) system, and its electronic configuration can be written as $(1S)^2(1P)^6$, $[Au_{25}(SR)_{18}]^0$ is a 7-e system $[(1S)^2(1P)^5]$ and $[Au_{25}(SR)_{18}]^+$ is a 6-e system $[(1S)^2(1P)^4]$. Table 6.2 shows that $[Au_{25}(SR)_{18}]^{-}$, $[Au_{25}H(SR)_{18}]^0$, and $[Au_{25}H_2(SR)_{18}]^+$ have essentially the same HOMO-LUMO gap, indicating that $[Au_{25}H(SR)_{18}]^0$ and $[Au_{25}H_2(SR)_{18}]^+$ are also 8-electron systems just like $[Au_{25}(SR)_{18}]^{-}$. To further confirm this, Figure 6.2 shows the frontier orbitals of $[Au_{25}(SR)_{18}]^{-}$, $[Au_{25}H(SR)_{18}]^0$, and $[Au_{25}H_2(SR)_{18}]^+$. One can see that the three clusters all have very similar features: P-type HOMOs and D-type LUMOs. These results show that H in ligand-protected gold clusters behaves as a metal and each H atom contributes one electron to the free-electron account just like Au. Therefore, hydrogen doping can be a powerful means to fine-tune the superatomic structures of atomically precise gold nanoclusters.

Table 6.2. HOMO-LUMO gaps of $[Au_{25}(SR)_{18}]^{-}$, $[Au_{25}H(SR)_{18}]^0$, and $[Au_{25}H_2(SR)_{18}]^+$. R=CH_3.

Cluster	**$[Au_{25}(SR)_{18}]^{-}$**	**$[Au_{25}H(SR)_{18}]^0$**	**$[Au_{25}H_2(SR)_{18}]^+$**
Gap (eV)	1.26	1.27	1.25

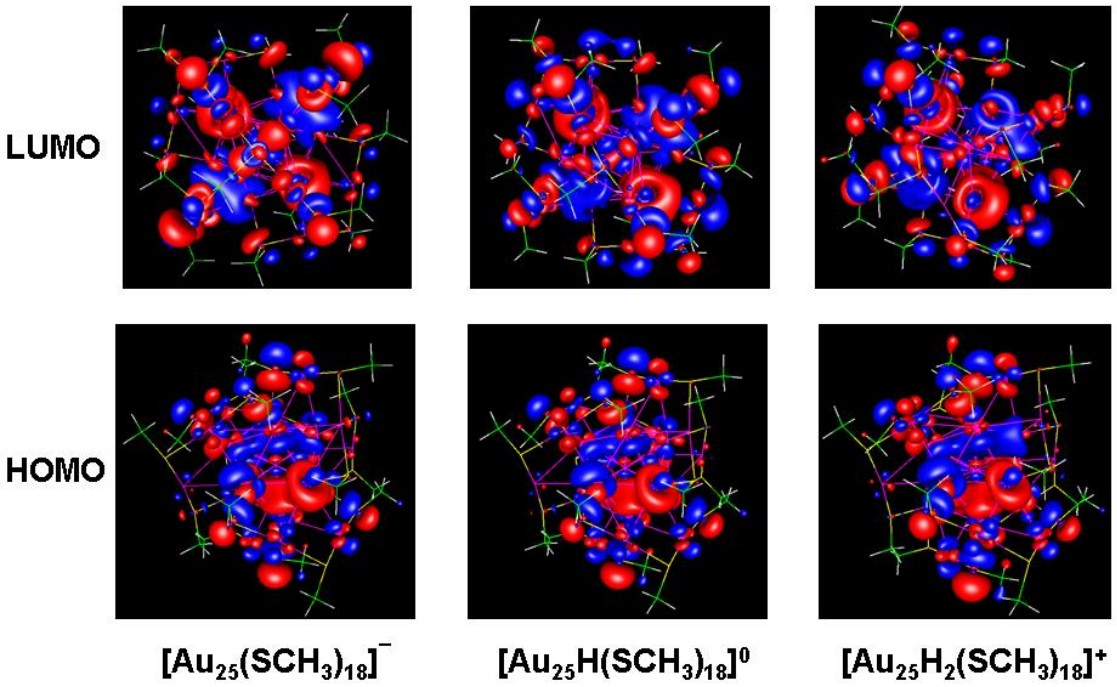

Figure 6.2. Frontier orbitals of $[Au_{25}(SR)_{18}]^{-}$, $[Au_{25}H(SR)_{18}]^{0}$, and $[Au_{25}H_2(SR)_{18}]^{+}$; only one HOMO and one LUMO are shown for each cluster.

6.2.2 Hydrogen in monoatom-doped bimetallic $[MAu_{24}(SR)_{18}]^{q}$ (M=Pt, Pd, and q=-2, 0) clusters.

Bimetallic $[M_xAu_{25-x}(SR)_{18}]^{q}$ clusters have attracted huge research interest and further diversified the chemical space that can be built upon $Au_{25}(SR)_{18}$. Pt and Pd are the first two foreign atoms that have been successfully introduced into the center of $Au_{25}(SR)_{18}$ cluster.[37, 39, 41] Especially, a recent experiment showed that $Pt_1Au_{24}(SR)_{18}$ is one of the best HER catalyst compared with other molecular catalysts.[51] We studied hydrogen adsorption on monoatom-doped bimetallic $[M_1Au_{24}(SR)_{18}]^{q}$ clusters (M=Pt, Pd, and q=-2, 0). As can be seen from Table 6.3, adsorption energies of the first H on the neutral clusters are much stronger than the anionic clusters. By adding more H on the neural

clusters, we find that the second H can also be strongly adsorbed, but the adsorption energies of the third H become much weaker. Figure 6.3 shows the optimized structures of $[PtAu_{24}(SR)_{18}]^0$ with one, two, and three H atoms. We explored different configurations of hydrogen adsorption. For two H, we found that the distorted metal core of $[PtAu_{24}(SR)_{18}]^0$ favors adsorptions of H on the opposite sides of the Pt center (Figure 6.3b).

Table 6.3. Free-electron count (n) of $[MAu_{24}(SR)_{18}]^q$ clusters (M=Pt, Pd, and q=-2, 0) and their sequential adsorption energy (eV) for hydrogen: first, ΔE_{H1}; second, ΔE_{H2}; third, ΔE_{H3}. R=CH_3.

Cluster	n	ΔE_{H1}	ΔE_{H2}	ΔE_{H3}
$\mathbf{[PtAu_{24}(SR)_{18}]^{2-}}$	8	-1.21	--	--
$\mathbf{[PtAu_{24}(SR)_{18}]^{0}}$	6	-2.20	-2.22	-1.14
$\mathbf{[PdAu_{24}(SR)_{18}]^{2-}}$	8	-1.35	--	--
$\mathbf{[PdAu_{24}(SR)_{18}]^{0}}$	6	-2.15	-2.16	-1.24

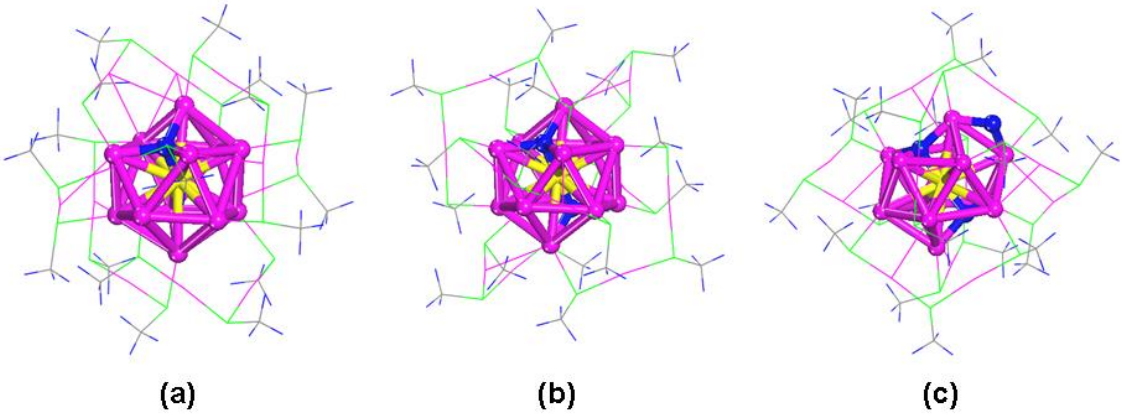

Figure 6.3. Optimized structures of $[PtAu_{24}(SR)_{18}]^0$ with one (a), two (b), and three (c) hydrogen atoms. Protecting motifs are showed in line mode for clarity. Au, magenta; Pt, yellow; H, blue; S, green; C, grey.

The calculated Bader charges on the adsorbed H in the $[MAu_{24}(SR)_{18}]^q$ clusters (M=Pt, Pd, and q=-2, 0) are close to zero (ranging from +0.022 to -0.006 |e|), indicating that H in these bimetallic gold clusters also behaves as a metal. $[PtAu_{24}(SR)_{18}]^0$ and $[PdAu_{24}(SR)_{18}]^0$ are 6-e systems with a configuration of $(1S)^2(1P)^4$, while $[PtAu_{24}(SR)_{18}]^{2-}$ and $[PdAu_{24}(SR)_{18}]^{2-}$ are 8-e systems of the $(1S)^2(1P)^6$ configuration. This explains why $[PtAu_{24}(SR)_{18}]^0$ and $[PdAu_{24}(SR)_{18}]^0$ readily adsorb two H atoms to become an 8-e superatom, while $[PtAu_{24}(SR)_{18}]^{2-}$ and $[PdAu_{24}(SR)_{18}]^{2-}$ tend not to. In other words, $[PtAu_{24}H_2(SR)_{18}]^0$ and $[PdAu_{24}H_2(SR)_{18}]^0$ are also 8-e systems, being isoelectronic to $[PtAu_{24}(SR)_{18}]^{2-}$ and $[PdAu_{24}(SR)_{18}]^{2-}$. This is why the HOMO-LUMO gaps of $[MAu_{24}(SR)_{18}]^{2-}$ and $[MAu_{24}H_2(SR)_{18}]^0$ are very close (Table 6.4). Frontier orbitals of $[PtAu_{24}H_2(SR)_{18}]^0$ and $[PdAu_{24}H_2(SR)_{18}]^0$ (Figure 6.4) further confirm their superatomic nature: P-type HOMO and D-type LUMO.

Table 6.4. HOMO-LUMO gap (eV) of $[MAu_{24}(SR)_{18}]^{2-}$ and $[MAu_{24}H_2(SR)_{18}]^0$ clusters (M=Pt, Pd). R=CH_3.

M	**$[MAu_{24}(SR)_{18}]^{2-}$**	**$[MAu_{24}H_2(SR)_{18}]^0$**
Pt	1.49	1.45
Pd	1.30	1.29

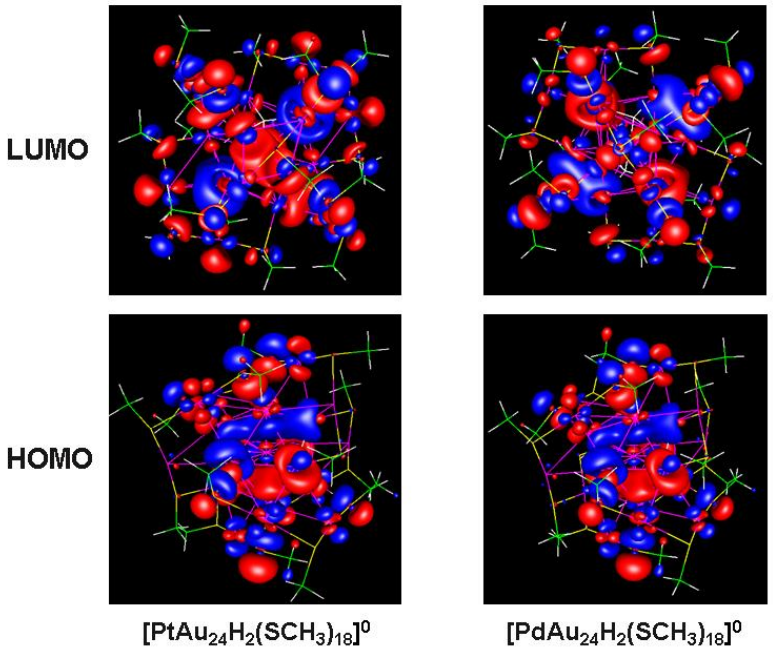

Figure 6.4. Frontier orbitals of $[PtAu_{24}H_2(SR)_{18}]^0$ and $[PdAu_{24}H_2(SR)_{18}]^0$; only one HOMO and one LUMO are shown for each cluster.

6.2.3 Hydrogen in monoatom-doped bimetallic $[MAu_{24}(SR)_{18}]^q$ clusters (M=Ag, Cu; q=0, -1).

Since Ag and Cu are in the same group as Au, doping of $Au_{25}(SR)_{18}$ by Ag or Cu offers additional complexity. For example, more than one Ag or Cu atom can be doped into the $Au_{25}(SR)_{18}$.[40, 43, 49-50] Although Pt and Pd prefer to be at the center, Cu or Ag can be doped into three different positions: the center of the Au_{13} core, the surface of the Au_{13} core, and the –SR-Au-SR-Au-SR- staple motif. Theoretical studies have demonstrated that surface-doped isomers are the most stable for $AgAu_{24}(SR)_{18}$ and $CuAu_{24}(SR)_{18}$.[42-44] However, experiments found surface-doped $AgAu_{24}(SR)_{18}$ but center-doped and staple-doped $CuAu_{24}(SR)_{18}$ clusters.[43-44] Table 6.5 lists the adsorption energies of H in $MAu_{24}(SR)_{18}$ (M=Cu, Ag) at different charge states and doping positions. As one can see,

they follow the same trend as those of $[Au_{25}(SR)_{18}]^q$ clusters: hydrogen adsorption on the neutral clusters is much stronger than on the anionic clusters, because the neutral bimetallic $[MAu_{24}(SR)_{18}]^0$ clusters (M=Ag, Cu) are 7-e systems, readily accepting one more electron from H to form the more stable 8-e configuration, the anionic clusters are already 8-e systems and less likely to add more electrons.

Table 6.5. Hydrogen adsorption energy (eV) on three $[MAu_{24}(SR)_{18}]^q$ (q=-1, 0) isomers (M=Cu, Ag)

M	**q**	**Doping position**		
		Center	Surface	Staple
Cu	q = -1	-1.36	-1.28	-1.21
	q = 0	-2.13	-2.09	-2.02
Ag	q = -1	-1.35	-1.14	-1.16
	q = 0	-2.07	-2.03	-2.05

Figure 6.5 shows the optimized structures of the three isomers of $[CuAu_{24}(SR)_{18}]^0$ with one adsorbed H. We found that for the center doping (Figure 6.5a), H has a Bader charge of -0.040 |e| and binds with the center Cu (r_{Cu-H} = 1.777 Å) and three surface Au atoms (r_{Au-H} = 1.931 Å); for the surface doping (Figure 6.5b), H has a Bader charge of -0.054 |e| and binds with the center Au (r_{Au-H} = 1.987 Å), the surface Cu (r_{Cu-H} = 1.774 Å) and two other surface Au atoms (r_{Au-H} = 1.951 Å); for the staple doping (Figure 6.5c), H has a Bader charge of +0.037 |e| and prefers to bond with the center Au (r_{Au-H} = 1.971 Å) and two surface Au atoms (r_{Au-H} = 1.844 Å). Remarkably, despite the three different interaction positions for H shown in Figure 6.5, the adsorption energies of H on the Cu-

doped neutral clusters are very similar. We found that the optimized structures of the three isomers of $[AgAu_{24}(SR)_{18}]^0$ with one adsorbed H are very similar to those of $[CuAu_{24}(SR)_{18}]^0$.

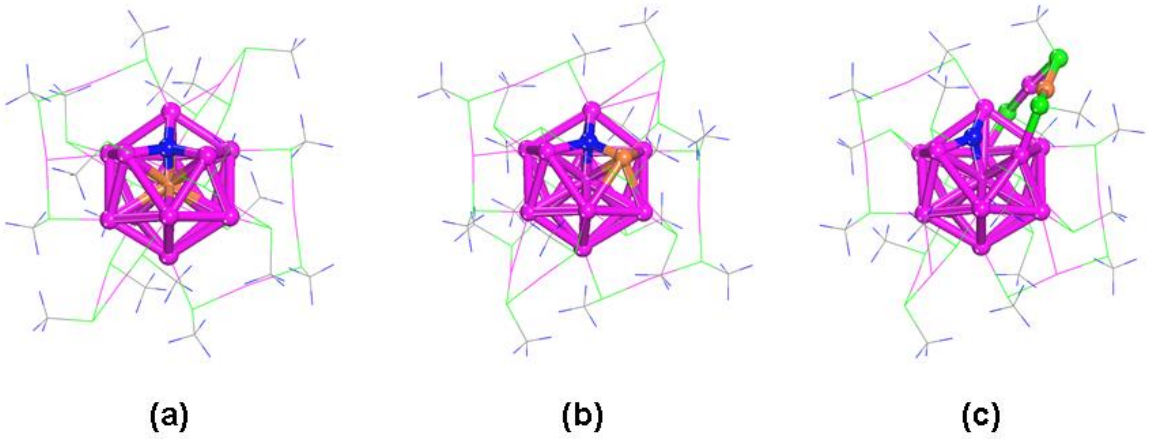

Figure 6.5. Optimized structures of the three isomers of $[CuAu_{24}(SR)_{18}]^0$ with one adsorbed H. (a) center-doped; (b) surface-doped; (c) staple-doped. Protecting motifs are showed in line mode for clarity. Au, magenta; Cu, orange; H, blue; S, green; C, grey.

Table 6.6 listed the HOMO-LUMO gaps of $[MAu_{24}(SR)_{18}]^-$ and $[MAu_{24}H(SR)_{18}]^0$ (M=Cu, Ag). As one can see, the HOMO-LUMO gaps of $[MAu_{24}(SR)_{18}]^-$ and the corresponding $[MAu_{24}H(SR)_{18}]^0$ for the same doping position are very close, because both are also 8-e systems, even though the gap varies among different doping positions. Frontier orbitals of the center-doped $[CuAu_{24}(SR)_{18}]^-$ and $[CuAu_{24}H(SR)_{18}]^0$ (Figure 6.6) further confirm their similar superatomic nature.

Table 6.6. HOMO-LUMO gap (eV) of $[MAu_{24}(SR)_{18}]^{-}$ and $[MAu_{24}H(SR)_{18}]^{0}$ (M=Cu, Ag).

System	**Doping position**		
	Center	Surface	Staple
$[CuAu_{24}(SR)_{18}]^{-}$	1.08	1.26	1.18
$[CuAu_{24}H(SR)_{18}]^{0}$	1.09	1.29	1.21
$[AgAu_{24}(SR)_{18}]^{-}$	1.09	1.23	1.21
$[AgAu_{24}H(SR)_{18}]^{0}$	1.12	1.23	1.24

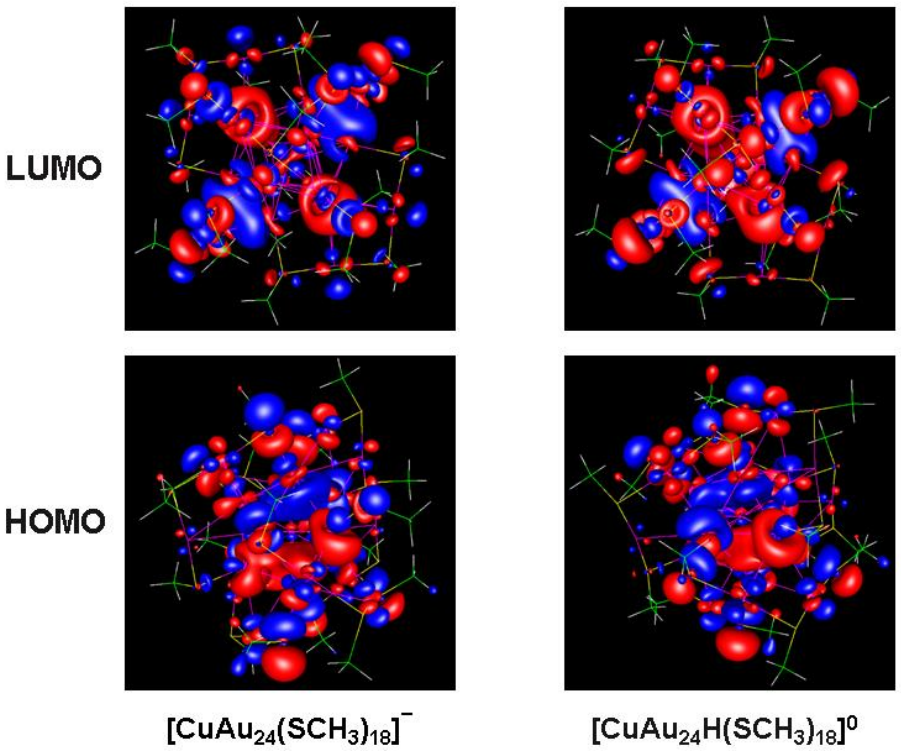

Figure 6.6. Frontier orbitals of center-doped $[CuAu_{24}(SR)_{18}]^{-}$ and $[CuAu_{24}H(SR)_{18}]^{0}$; only one HOMO and one LUMO are shown for each cluster.

6.2.4 Potential for hydrogen evolution reaction (HER).

Our results of hydrogen adsorption on $Au_{25}(SR)_{18}$ and monoatom-doped bimetallic $MAu_{24}(SR)_{18}$ clusters have important implications for electrocatalytic hydrogen evolution. First, our results suggest that hydrogen-adsorbed gold clusters can be a stable intermediate. Second, these intermediate may play important roles in electrocatalytic water splitting, especially for HER. To evaluate this stability and the clusters' potential for HER, we computed their hydrogen adsorption free energy (ΔG_H) using a computational reversed hydrogen electrode ($H^+ + e^- \rightarrow ½\ H_2$). As shown previously, a nearly neutral ΔG_H would suggest a good HER catalyst.[52] Figure 6.7 shows the calculated ΔG_H for hydrogen evolution on $Au_{25}(SR)_{18}$ cluster and monoatom-doped bimetallic $MAu_{24}(SR)_{18}$ clusters (M= Pt, Pd, Ag, Cu, Hg, Cd). The 8-e $HgAu_{24}(SR)_{18}$ and $CdAu_{24}(SR)_{18}$ clusters have been successfully sythesized,[45-47] so we also examined their H adsorption energetics; Figure 6.7 shows that they have high positive ΔG_H, so they cannot be good electrocatalysts for HER. But the 7-electron and 6-electron systems have much closer-to-zero ΔG_H. As clearly shown in the figure, $PtAu_{24}(SR)_{18}$ has the lowest ΔG_H, so we predict that $PtAu_{24}(SR)_{18}$ is the best candidate for HER among the clusters studied here. $PdAu_{24}(SR)_{18}$ and center-doped $CuAu_{24}(SR)_{18}$ also have reasonably close-to-zero ΔG_H. The calculated ΔG_H for the surface-doped and staple-doped $CuAu_{24}(SR)_{18}$ are slightly higher than the center-doped one. Thus, it is expected that $PdAu_{24}(SR)_{18}$ and center-doped $CuAu_{24}(SR)_{18}$ also have good catalytic activities for HER, followed by $Au_{25}(SR)_{18}$ and surface-doped $AgAu_{24}(SR)_{18}$. Our prediction is consistent with the experimental observation of $PtAu_{24}(SR)_{18}$'s higher HER activity than $Au_{25}(SR)_{18}$.[51] The

predicted HER activity for $PdAu_{24}(SR)_{18}$, $CuAu_{24}(SR)_{18}$, and $AgAu_{24}(SR)_{18}$ needs experimental verification.

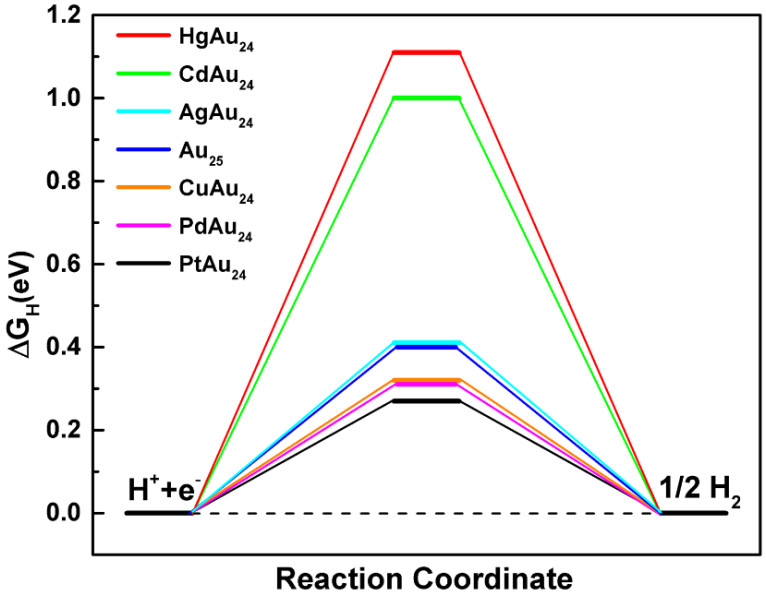

Figure 6.7. The calculated free energy diagram for hydrogen evolution of $Au_{25}(SR)_{18}$ and bimetallic $MAu_{24}(SR)_{18}$ clusters (M= Pt, Pd, Ag, Cu, Hg, Cd). The doping positions for Hg, Cd, and Cu are center; for Ag, it is surface.

6.2.5 Detecting interstitial H in ligand-protected gold nanoclusters.

Although there was no experimental attempt to characterize adsorbed hydrogen in ligand-protected gold nanoclusters, there have many recent advances in experimental study of H-Au interactions in both homogeneous Au(I) complexes and heterogeneous CeO_2-supported gold nanoparticles via H-NMR,[53] FT-IR,[54] and inelastic neutron scattering (INS).[55] In the H-Au(I) complex, H behaves as a hydride ligand, therefore very different from the metallic behavior that we found here in gold nanoclusters. But using the similar experimental techniques in these recent studies,[53-55] we think that hydrogen species in ligand-protected gold and bimetallic nanoclusters can be spectroscopically identified. INS

is especially powerful as it permits to distinguish both surface and bulk hydrogen species in metal particles.[56-59] *In situ* INS study of the gold nanoclusters during the HER process could shed important light on the nature of hydrogen species during the reaction.

6.3 Conclusions

We have investigated how hydrogen interacts with $[Au_{25}(SR)_{18}]^q$ clusters and monoatom-doped bimetallic $[MAu_{24}(SR)_{18}]^q$ clusters (M=Pt, Pd, Ag, Cu, Hg, Cd) by DFT calculations. We find that hydrogen behaves as a metal in these clusters and contributes its 1s electron to the superatomic free-electron count. This opposite behavior to the hydride in copper and silver clusters allows the small-sized hydrogen to interstitially dope the $[Au_{25}(SR)_{18}]^q$ and $[M_1Au_{24}(SR)_{18}]^q$ clusters and tune their superatomic electronic structure. The energetics shows that when an 8-e superatom is formed after H doping, the binding energy of H is much stronger, while binding of H with an already 8-e superatom is much weaker. Indeed, the HOMO-LUMO gaps and frontier orbitals of $[Au_{25}H(SR)_{18}]^0$, $[Au_{25}H_2(SR)_{18}]^+$, $[PtAu_{24}H_2(SR)_{18}]^0$, $[PdAu_{24}H_2(SR)_{18}]^0$, $[AgAu_{24}H(SR)_{18}]^0$, and $[CuAu_{24}H(SR)_{18}]^0$ all have very similar features, because they are all 8-e superatoms. This insight has important implications in using $Au_{25}(SR)_{18}$ and other gold and bimetallic clusters as electrocatalysts for HER. By calculating ΔG_H, we predict that $PtAu_{24}(SR)_{18}$, $PdAu_{24}(SR)_{18}$ and center-doped $CuAu_{24}(SR)_{18}$ can be very good electrocatalysts for HER. Our results hence demonstrate the unique behavior of hydrogen in atomically precise gold clusters and invite experimental detection of hydrogen in these clusters.

References

1. Mohtadi, R.; Orimo, S., The Renaissance of Hydrides as Energy Materials. *Nat. Rev. Mater.* **2016**, *2*, 16091.

2. Rusman, N.; Dahari, M., A Review on the Current Progress of Metal Hydrides Material for Solid-State Hydrogen Storage Applications. *Int. J. Hydrogen Energy* **2016**, *41*, 12108-12126.

3. Perutz, R. N.; Procacci, B., Photochemistry of Transition Metal Hydrides. *Chem. Rev.* **2016**, *116*, 8506-8544.

4. Jordan, A. J.; Lalic, G.; Sadighi, J. P., Coinage Metal Hydrides: Synthesis, Characterization, and Reactivity. *Chem. Rev.* **2016**, *116*, 8318-8372.

5. Pundt, A.; Kirchheim, R., Hydrogen in Metals: Microstructural Aspects. *Annu. Rev. Mater. Res.* **2006**, *36*, 555-608.

6. Chiu, C. Y.; Huang, M. H., Polyhedral Au–Pd Core–Shell Nanocrystals as Highly Spectrally Responsive and Reusable Hydrogen Sensors in Aqueous Solution. *Angew. Chem. Int. Ed.* **2013**, *52*, 12709-12713.

7. Wadell, C.; Nugroho, F. A. A.; Lidström, E.; Iandolo, B.; Wagner, J. B.; Langhammer, C., Hysteresis-Free Nanoplasmonic Pd–Au Alloy Hydrogen Sensors. *Nano Lett.* **2015**, *15*, 3563-3570.

8. Hadlington, T. J.; Hermann, M.; Frenking, G.; Jones, C., Low Coordinate Germanium (Ii) and Tin (Ii) Hydride Complexes: Efficient Catalysts for the Hydroboration of Carbonyl Compounds. *J. Am. Chem. Soc.* **2014**, *136*, 3028-3031.

9. Bourrez, M.; Steinmetz, R.; Ott, S.; Gloaguen, F.; Hammarström, L., Concerted Proton-Coupled Electron Transfer from a Metal-Hydride Complex. *Nat. Chem.* **2015**, *7*, 140-145.

10. Kato, S.; Matam, S. K.; Kerger, P.; Bernard, L.; Battaglia, C.; Vogel, D.; Rohwerder, M.; Züttel, A., The Origin of the Catalytic Activity of a Metal Hydride in Co_2 Reduction. *Angew. Chem. Int. Ed.* **2016**, *128*, 6132-6136.

11. Walter, M.; Akola, J.; Lopez-Acevedo, O.; Jadzinsky, P. D.; Calero, G.; Ackerson, C. J.; Whetten, R. L.; Grönbeck, H.; Häkkinen, H., A Unified View of Ligand-Protected Gold Clusters as Superatom Complexes. *Proc. Natl. Acad. Sci.* **2008**, *105*, 9157-9162.

12. Bezman, S. A.; Churchill, M. R.; Osborn, J. A.; Wormald, J., Preparation and Crystallographic Characterization of a Hexameric Triphenylphosphinecopper Hydride Cluster. *J. Am. Chem. Soc* **1971**, *93*, 2063-2065.

13. Lemmen, T. H.; Folting, K.; Huffman, J. C.; Caulton, K. G., Copper Polyhydrides. *J. Am. Chem. Soc* **1985**, *107*, 7774-7775.

14. Liu, C.; Sarkar, B.; Huang, Y.-J.; Liao, P.-K.; Wang, J.-C.; Saillard, J.-Y.; Kahlal, S., Octanuclear Copper (I) Clusters Inscribed in a Se_{12} Icosahedron: Anion-Induced Modulation of the Core Size and Symmetry. *J. Am. Chem. Soc* **2009**, *131*, 11222-11233.

15. Dhayal, R. S.; Liao, J.-H.; Lin, Y.-R.; Liao, P.-K.; Kahlal, S.; Saillard, J.-Y.; Liu, C., A Nanospheric Polyhydrido Copper Cluster of Elongated Triangular Orthobicupola Array: Liberation of H_2 from Solar Energy. *J. Am. Chem. Soc* **2013**, *135*, 4704-4707.

16. Zavras, A.; Khairallah, G. N.; Connell, T. U.; White, J. M.; Edwards, A. J.; Donnelly, P. S.; O'Hair, R. A., Synthesis, Structure and Gas-Phase Reactivity of a Silver Hydride Complex $[Ag_3\{(Pph_2)_2ch_2\}_3(M_3\text{-}H)(M_3\text{-}Cl)]Bf_4$. *Angew. Chem. Int. Ed.* **2013**, *52*, 8391-8394.

17. Edwards, A. J.; Dhayal, R. S.; Liao, P. K.; Liao, J. H.; Chiang, M. H.; Piltz, R. O.; Kahlal, S.; Saillard, J. Y.; Liu, C., Chinese Puzzle Molecule: A 15 Hydride, 28 Copper Atom Nanoball. *Angew. Chem. Int. Ed.* **2014**, *53*, 7214-7218.

18. Nguyen, T.-A. D.; Jones, Z. R.; Goldsmith, B. R.; Buratto, W. R.; Wu, G.; Scott, S. L.; Hayton, T. W., A Cu25 Nanocluster with Partial Cu (0) Character. *J. Am. Chem. Soc.* **2015**, *137*, 13319-13324.

19. Dhayal, R. S.; Liao, J. H.; Wang, X.; Liu, Y. C.; Chiang, M. H.; Kahlal, S.; Saillard, J. Y.; Liu, C., Diselenophosphate-Induced Conversion of an Achiral $[Cu_{20}h_{11}\{S_2p(Oipr)_2\}_9]$ into a Chiral $[Cu_{20}H_{11}\{Se_2P(Oipr)_2\}_9]$ Polyhydrido Nanocluster. *Angew. Chem. Int. Ed.* **2015**, *54*, 13604-13608.

20. Daly, S.; Krstić, M.; Giuliani, A.; Antoine, R.; Nahon, L.; Zavras, A.; Khairallah, G. N.; Bonačić-Koutecký, V.; Dugourd, P.; Richard, A., Gas-Phase Vuv Photoionisation and Photofragmentation of the Silver Deuteride Nanocluster $[Ag_{10}d_8l_6]^{2+}$(L= Bis (Diphenylphosphino) Methane). A Joint Experimental and Theoretical Study. *Phys. Chem. Chem. Phys.* **2015**, *17*, 25772-25777.

21. Bootharaju, M. S.; Dey, R.; Gevers, L. E.; Hedhili, M. N.; Basset, J.-M.; Bakr, O. M., A New Class of Atomically Precise, Hydride-Rich Silver Nanoclusters Co-Protected by Phosphines. *J. Am. Chem. Soc.* **2016**, *138*, 13770-13773.

22. Nguyen, T.-A. D.; Jones, Z. R.; Leto, D. F.; Wu, G.; Scott, S. L.; Hayton, T. W., Ligand-Exchange-Induced Growth of an Atomically Precise Cu_{29} Nanocluster from a Smaller Cluster. *Chem. Mater.* **2016**, *28*, 8385-8390.

23. Dhayal, R. S.; van Zyl, W. E.; Liu, C., Polyhydrido Copper Clusters: Synthetic Advances, Structural Diversity, and Nanocluster-to-Nanoparticle Conversion. *Acc. Chem. Res.* **2015**, *49*, 86-95.

24. Akola, J.; Walter, M.; Whetten, R. L.; Häkkinen, H.; Grönbeck, H., On the Structure of Thiolate-Protected Au_{25}. *J. Am. Chem. Soc.* **2008**, *130*, 3756-3757.

25. Zhu, M.; Aikens, C. M.; Hollander, F. J.; Schatz, G. C.; Jin, R., Correlating the Crystal Structure of a Thiol-Protected Au_{25} Cluster and Optical Properties. *J. Am. Chem. Soc.* **2008**, *130*, 5883-5885.

26. Heaven, M. W.; Dass, A.; White, P. S.; Holt, K. M.; Murray, R. W., Crystal Structure of the Gold Nanoparticle $[N(C_8h_{17})_4][Au_{25}(Sch_2ch_2ph)_{18}]$. *J. Am. Chem. Soc.* **2008**, *130*, 3754-3755.

27. Jupally, V. R.; Kota, R.; Dornshuld, E. V.; Mattern, D. L.; Tschumper, G. S.; Jiang, D.-e.; Dass, A., Interstaple Dithiol Cross-Linking in $Au_{25}(Sr)_{18}$ Nanomolecules: A Combined Mass Spectrometric and Computational Study. *J. Am. Chem. Soc* **2011**, *133*, 20258-20266.

28. Tofanelli, M. A.; Ackerson, C. J., Superatom Electron Configuration Predicts Thermal Stability of $Au_{25}(Sr)_{18}$ Nanoclusters. *J. Am. Chem. Soc.* **2012**, *134*, 16937-16940.

29. Kauffman, D. R.; Alfonso, D.; Matranga, C.; Qian, H.; Jin, R., Experimental and Computational Investigation of Au_{25} Clusters and Co_2: A Unique Interaction and Enhanced Electrocatalytic Activity. *J. Am. Chem. Soc* **2012**, *134*, 10237-10243.

30. Antonello, S.; Perera, N. V.; Ruzzi, M.; Gascón, J. A.; Maran, F., Interplay of Charge State, Lability, and Magnetism in the Molecule-Like $Au_{25}(Sr)_{18}$ Cluster. *J. Am. Chem. Soc* **2013**, *135*, 15585-15594.

31. De Nardi, M.; Antonello, S.; Jiang, D. E.; Pan, F.; Rissanen, K.; Ruzzi, M.; Venzo, A.; Zoleo, A.; Maran, F., Gold Nanowired: A Linear $(Au_{25})N$ Polymer from Au_{25} Molecular Clusters. *ACS nano* **2014**, *8*, 8505-8512.

32. Luo, Z.; Nachammai, V.; Zhang, B.; Yan, N.; Leong, D. T.; Jiang, D.-e.; Xie, J., Toward Understanding the Growth Mechanism: Tracing All Stable Intermediate Species from Reduction of Au (I)–Thiolate Complexes to Evolution of Au_{25} Nanoclusters. *J. Am. Chem. Soc* **2014**, *136*, 10577-10580.

33. Wu, Z.; Jiang, D.-e.; Mann, A. K.; Mullins, D. R.; Qiao, Z.-A.; Allard, L. F.; Zeng, C.; Jin, R.; Overbury, S. H., Thiolate Ligands as a Double-Edged Sword for Co Oxidation on Ceo_2 Supported $Au_{25}(Sch_2ch_2ph)_{18}$ Nanoclusters. *J. Am. Chem. Soc* **2014**, *136*, 6111-6122.

34. Ouyang, R.; Jiang, D.-e., Understanding Selective Hydrogenation of A, B-Unsaturated Ketones to Unsaturated Alcohols on the $Au_{25}(Sr)_{18}$ Cluster. *ACS Catal.* **2015**, *5*, 6624-6629.

35. Jin, R.; Zeng, C.; Zhou, M.; Chen, Y., Atomically Precise Colloidal Metal Nanoclusters and Nanoparticles: Fundamentals and Opportunities. *Chem. Rev.* **2016**, *116*, 10346-10413.

36. Negishi, Y.; Nobusada, K.; Tsukuda, T., Glutathione-Protected Gold Clusters Revisited: Bridging the Gap between Gold (I)− Thiolate Complexes and Thiolate-Protected Gold Nanocrystals. *J. Am. Chem. Soc* **2005**, *127*, 5261-5270.

37. Fields-Zinna, C. A.; Crowe, M. C.; Dass, A.; Weaver, J. E.; Murray, R. W., Mass Spectrometry of Small Bimetal Monolayer-Protected Clusters. *Langmuir* **2009**, *25*, 7704-7710.

38. Jiang, D. E.; Dai, S., From Superatomic $Au_{25}(Sr)_{18}^{-}$ to Superatomic $M@Au_{24}(Sr)_{18}^{Q}$ Core− Shell Clusters. *Inorg. Chem.* **2009**, *48*, 2720-2722.

39. Negishi, Y.; Kurashige, W.; Niihori, Y.; Iwasa, T.; Nobusada, K., Isolation, Structure, and Stability of a Dodecanethiolate-Protected Pd_1au_{24} Cluster. *Phys. Chem. Chem. Phys.* **2010**, *12*, 6219-6225.

40. Negishi, Y.; Iwai, T.; Ide, M., Continuous Modulation of Electronic Structure of Stable Thiolate-Protected Au_{25} Cluster by Ag Doping. *Chem. Commun.* **2010**, *46*, 4713-4715.

41. Qian, H.; Jiang, D. E.; Li, G.; Gayathri, C.; Das, A.; Gil, R. R.; Jin, R., Monoplatinum Doping of Gold Nanoclusters and Catalytic Application. *J. Am. Chem. Soc* **2012**, *134*, 16159-16162.

42. Guidez, E. B.; Mäkinen, V.; Häkkinen, H.; Aikens, C. M., Effects of Silver Doping on the Geometric and Electronic Structure and Optical Absorption Spectra of the $Au_{25-N}ag_n(Sh)_{18}^{-}$(N= 1, 2, 4, 6, 8, 10, 12) Bimetallic Nanoclusters. *J. Phys. Chem. C* **2012**, *116*, 20617-20624.

43. Negishi, Y.; Munakata, K.; Ohgake, W.; Nobusada, K., Effect of Copper Doping on Electronic Structure, Geometric Structure, and Stability of Thiolate-Protected Au_{25} Nanoclusters. *J. Phys. Chem. Lett.* **2012**, *3*, 2209-2214.

44. Yamazoe, S.; Kurashige, W.; Nobusada, K.; Negishi, Y.; Tsukuda, T., Preferential Location of Coinage Metal Dopants (M= Ag or Cu) in $[Au_{25-X}m_x(Sc_2h_4ph)_{18}]^-(X\sim 1)$ as Determined by Extended X-Ray Absorption Fine Structure and Density Functional Theory Calculations. *J. Phys. Chem. C* **2014**, *118*, 25284-25290.

45. Wang, S.; Song, Y.; Jin, S.; Liu, X.; Zhang, J.; Pei, Y.; Meng, X.; Chen, M.; Li, P.; Zhu, M., Metal Exchange Method Using Au25 Nanoclusters as Templates for Alloy Nanoclusters with Atomic Precision. *J. Am. Chem. Soc.* **2015**, *137*, 4018-4021.

46. Liao, L.; Zhou, S.; Dai, Y.; Liu, L.; Yao, C.; Fu, C.; Yang, J.; Wu, Z., Mono-Mercury Doping of Au25 and the Homo/Lumo Energies Evaluation Employing Differential Pulse Voltammetry. *J. Am. Chem. Soc.* **2015**, *137*, 9511-9514.

47. Yao, C.; Lin, Y.-j.; Yuan, J.; Liao, L.; Zhu, M.; Weng, L.-h.; Yang, J.; Wu, Z., Mono-Cadmium Vs Mono-Mercury Doping of Au_{25} Nanoclusters. *J. Am. Chem. Soc.* **2015**, *137*, 15350-15353.

48. Kwak, K.; Tang, Q.; Kim, M.; Jiang, D.-e.; Lee, D., Interconversion between Superatomic 6-Electron and 8-Electron Configurations of $M@Au_{24}(Sr)_{18}$ Clusters (M= Pd, Pt). *J. Am. Chem. Soc* **2015**, *137*, 10833-10840.

49. Joshi, C. P.; Bootharaju, M. S.; Alhilaly, M. J.; Bakr, O. M., $[Ag_{25}(Sr)_{18}]^-$: The "Golden" Silver Nanoparticle. *J. Am. Chem. Soc* **2015**, *137*, 11578-11581.

50. Krishnadas, K.; Baksi, A.; Ghosh, A.; Natarajan, G.; Pradeep, T., Structure-Conserving Spontaneous Transformations between Nanoparticles. *Nat. Commun.* **2016**, *7*.

51. Kwak, K.; Choi, W.; Tang, Q.; Kim, M.; Lee, Y.; Jiang, D. E.; Lee, D., A Molecule-Like $Ptau_{24}(Sc_6h_{13})_{18}$ Nanocluster as an Electrocatalyst for Hydrogen Production. *Nat. Commun.* **2017**, *8*, 14723.

52. Nørskov, J. K.; Bligaard, T.; Logadottir, A.; Kitchin, J. R.; Chen, J. G.; Pandelov, S.; Stimming, U., Trends in the Exchange Current for Hydrogen Evolution. *J. Electrochem. Soc.* **2005**, *152*, J23-J26.

53. Roşca, D.-A.; Fernandez-Cestau, J.; Hughes, D. L.; Bochmann, M., Reactivity of Gold Hydrides: O_2 Insertion into the Au–H Bond. *Organometallics* **2014**, *34*, 2098-2101.

54. Juárez, R.; Parker, S. F.; Concepción, P.; Corma, A.; García, H., Heterolytic and Heterotopic Dissociation of Hydrogen on Ceria-Supported Gold Nanoparticles. Combined Inelastic Neutron Scattering and Ft-Ir Spectroscopic Study on the Nature and Reactivity of Surface Hydrogen Species. *Chem. Sci.* **2010**, *1*, 731-738.

55. Silverwood, I.; Rogers, S.; Callear, S.; Parker, S.; Catlow, C., Evidence for a Surface Gold Hydride on a Nanostructured Gold Catalyst. *Chem. Commun.* **2016**, *52*, 533-536.

56. Sköld, K.; Nelin, G., Diffusion of Hydrogen in the A-Phase of Pd-H Studied by Small Energy Transfer Neutron Scattering. *J. Phys. Chem. Solids* **1967**, *28*, 2369-2380.

57. Nicol, J. M.; Rush, J. J.; Kelley, R. D., Neutron Spectroscopic Evidence for Subsurface Hydrogen in Palladium. *Phys. Rev. B* **1987**, *36*, 9315.

58. Nicol, J. M., Chemisorbed Hydrogen and Hydrogenous Molecules. *Spectrochim. Acta Mol. Spectrosc.* **1992**, *48*, 313-327.

59. Albers, P. W.; Krauter, J. G.; Ross, D.; Heidenreich, R. G.; Köhler, K.; Parker, S. F., Identification of Surface States on Finely Divided Supported Palladium Catalysts by Means of Inelastic Incoherent Neutron Scattering. *Langmuir* **2004**, *20*, 8254-8260.

Chapter 7

Stronger-than-Pt Hydrogen Adsorption in a Au_{22} Nanocluster for Hydrogen Evolution Reaction

Abstract

Although structures of ligand-protected Cu-H and Ag-H nanoclusters have been reported, atomically precise Au-H nanoclusters have been elusive. From first-principles density functional theory (DFT), we show that the eight coordinatively unsaturated (*cus*) Au atoms in the $Au_{22}(L^8)_6$ cluster [L = 1,8-bis(diphenylphosphino) octane] can adsorb H stronger than Pt, thereby being a potentially promising catalyst for hydrogen evolution reaction (HER). We find that up to six H atoms can adsorb on the $Au_{22}(L^8)_6$ cluster and they all have close-to-zero Gibbs free adsorption energies (ΔG_H). From the HOMO-LUMO gaps, frontier orbitals, and Bader charge analysis, we conclude that H behaves as a hydride or electron-withdrawing ligand in the $Au_{22}(L^8)_6$ clusters, in contrast with the metallic H in thiolate-protected Au nanoclusters. Our study demonstrates that ligand-protected Au clusters with *cus* Au sites will be the most promising candidates for realizing Au-H nanoclusters and excellent electrocatalysts for HER.

7.1 Introduction

The behavior of H in metals has been of great interest for many decades.[1-3] Metal-hydrogen systems are widely utilized in energy-storage systems, sensor applications, as well as catalysis.[4] In contrast with bulk metal hydrides, the structures of H-metal nanoclusters can provide insight from a molecular perspective of how H interacts with metals and how the magic sizes or superatoms evolve.[5] The hydride ligand has been used in the synthesis of ligand-protected Cu or Ag nanoclusters.[6-13] Especially for the Cu clusters, a series of air- and moisture-stable Cu hydride clusters ranging from Cu_7H to $Cu_{32}H_{20}$ have been successfully synthesized and structure-determined.[14] More recently, three new hydride-rich Ag clusters, $[Ag_{18}H_{16}(TPP)_{10}]^{2+}$, $[Ag_{25}H_{22}(DPPE)_8]^{3+}$, and $[Ag_{26}H_{22}(TFPP)_{13}]^{2+}$, have been synthesized.[15]

Atomically precise Au nanoclusters have attracted intensive research interest over the past two decades due to their potential applications in catalysis, biology, and nanotechnology.[16-18] However, to the best of our knowledge, H has not been observed in ligand-protected Au nanoclusters, but some intermediate states of H adsorbed in thiolate-protected Au clusters have been proposed to explain their roles in hydrogen evolution reaction (HER).[19] It has been shown that both $Au_{25}(SR)_{18}$ and $PtAu_{24}(SR)_{18}$ exhibit high HER activity and the activity of $PtAu_{24}(SR)_{18}$ is much higher than that of $Au_{25}(SR)_{18}$. In fact, $PtAu_{24}(SR)_{18}$ is among the most active molecular catalysts for HER. To understand the underlying reason, the behavior of H in $[Au_{25}(SR)_{18}]^q$ and mono-atom-doped bimetallic $[M_1Au_{24}(SR)_{18}]^q$ clusters including $PtAu_{24}(SR)_{18}$ has been investigated.[20] It was found that H behaves as a metal in these clusters and contributes its 1s electron to the

superatomic free-electron count. But H adsorption is still uphill for at least 200 meV in free energy on these Au clusters, indicating their thermodynamic instability. One strategy to drive down the free energy is to create the coordinatively unsaturated (*cus*) or *in situ* uncoordinated sites in the Au clusters.

Unlike many other clusters where the surface Au atoms are fully coordinated by the protecting ligands,[21-24] the $Au_{22}(L^8)_6$ cluster (L = 1,8-bis(diphenylphosphino) octane) is unique in that it contains eight *cus* or so-called in situ uncoordinated Au atoms.[25] As shown in Figure 7.1, the rod-like Au_{22} core of the $Au_{22}(L^8)_6$ cluster consists of two Au_{11} units clipped together by four L^8 ligands (ball-and-stick ligands in Figure 7.1a), while the additional two ligands each coordinate to a Au_{11} unit in a bidentate fashion. Significantly, eight Au atoms (highlighted in red in Figure 7.1b) at the interface of the two Au_{11} units are not coordinated by any ligands. The presence of the *cus* Au atoms is promising for catalysis. For example, it was found that the intact $Au_{22}(L^8)_6$ nanoclusters readily catalyze CO oxidation at room temperature; DFT modeling of adsorption of CO and O_2 suggested that the *cus* Au atoms are the active sites.[26]

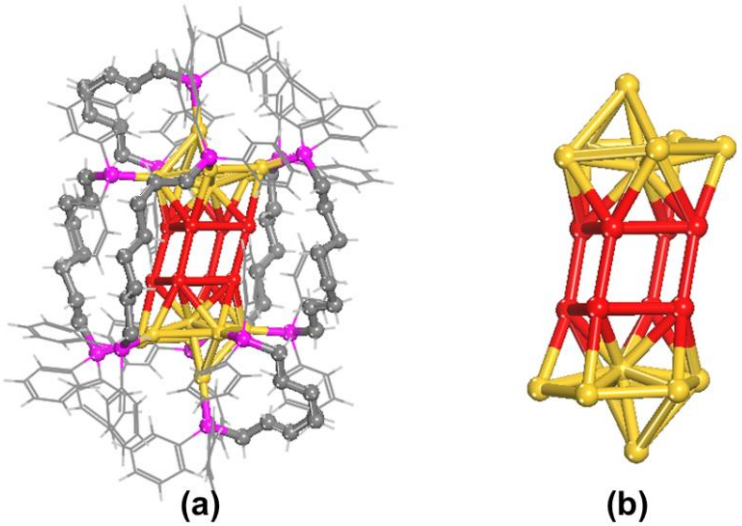

Figure 7.1. Total structure (a) and core structure (b) of the $Au_{22}(L^8)_6$ cluster. *Cus* Au, red; other Au, yellow; P, magenta; C, grey; H, light grey.

Due to its many cus Au sites, we hypothesize that $Au_{22}(L^8)_6$ offers a unique opportunity to observe H in Au nanoclusters and can be an excellent electrocatalyst for HER. To test this hypothesis, here we studied the structures and energetics of H adsorption on the $Au_{22}(L^8)_6$ cluster by first-principles density functional theory (DFT) and evaluated the Gibbs free energies of H adsorption (ΔG_H) to predict the HER activity. In addition, the HOMO-LUMO gaps, frontier orbitals, and partial atomic charges of the H-adsorbed $Au_{22}(L^8)_6$ clusters were analyzed to better understand the behavior of H in the cluster.

7.2 Results and discussion

7.2.1 Energetics and structures of H adsorption on the $Au_{22}(L^8)_6$ cluster.

Figure 7.2 shows the calculated differential H adsorption energy (ΔE_H; blue) and free energy (ΔG_H; red) on the $Au_{22}(L^8)_6$ cluster relative to ½ H_2. One can see that up to six H

atoms can be favorably adsorbed on the cluster, while the second H binds strongest. ΔG_H has been considered as a good descriptor for HER and a close-to-zero ΔG_H would suggest a good HER catalyst.[27] One can see that ΔG_H on the $Au_{22}(L^8)_6$ cluster is close-to-zero for the first six H atoms, except the second one. This result has two important implications: (i) the two-H state or $Au_{22}H_2(L^8)_6$ cluster is highly favorable and probably can be detected experimentally; (ii) the $Au_{22}(L^8)_6$ cluster should be a highly active HER catalyst since it offers so many sites that have close-to-zero ΔG_H. For comparison, we have also calculated ΔG_H on the Pt(111) surface (at the same level of theory and with the same approach) and found it to be −0.14 eV. Hence, the second H adsorption on the $Au_{22}(L^8)_6$ cluster (ΔG_H = −0.41 eV) is much stronger than H adsorption on the Pt(111) surface, indicating the high stability of the $Au_{22}H_2(L^8)_6$ cluster.

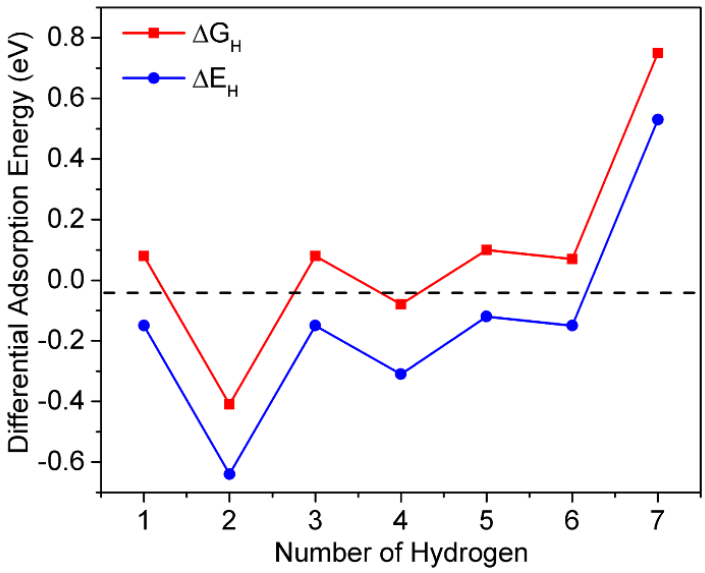

Figure 7.2. Differential adsorption energy ΔE_H (blue) and adsorption free energy ΔG_H (red) as a function of number of hydrogen adsorbed on the $Au_{22}(L^8)_6$ cluster.

H adsorption on the $Au_{22}(L^8)_6$ cluster shown in Figure 7.2 is drastically different from previously studied $[Au_{25}(SR)_{18}]^q$and mono-atom-doped bimetallic $[M_1Au_{24}(SR)_{18}]^q$ clusters. For the thiolate-protected Au clusters, all the surface gold atoms are already protected by thiolate ligands, so there is no *cus* Au site. As a result, the bonding of H in thiolate-protected Au clusters is generally weaker (ΔG_H > 0.200 eV) than that in the $Au_{22}(L^8)_6$ cluster ($\Delta G_H \sim -0.40$ to 0.10 eV).

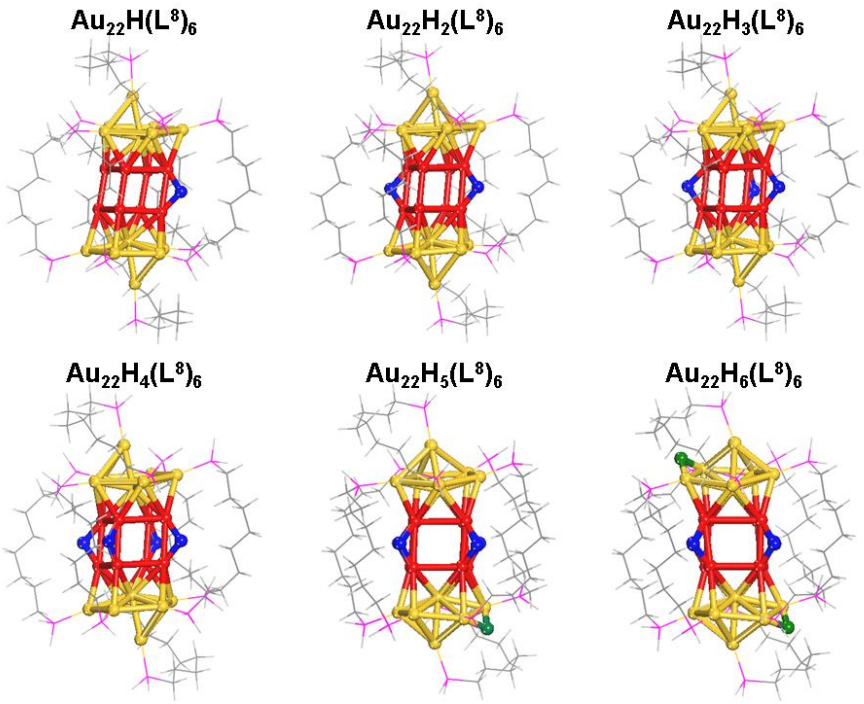

Figure 7.3. Optimized structures of the $Au_{22}H_n(L^8)_6$ clusters, n=1~6. Protecting ligands are shown in line mode. *Cus* Au, red; other Au, yellow; H at the *cus* Au sites, blue; H at the non-*cus* Au sites, green; other H, light grey; P, magenta; C, grey.

To understand the energetic pattern of H adsorption on the $Au_{22}(L^8)_6$ cluster, we now examine the optimized structures. One can see from Figure 7.3 that the first H atom adsorbs at the long-bridge site formed by two *cus* Au atoms, while the second H atom

also adsorbs at the long-bridge site on the opposite side of the Au_8 cube. Then the third and the fourth H atoms occupy the other two long-bridge sites subsequently. Interestingly, the fifth and the sixth H atoms adsorb at the bridge sites at the opposite ends of the cluster where the Au atoms are not *cus* sites but protected by phosphine ligands. If the first H atom directly adsorbs at the non-*cus*-Au bridge site, ΔG_H is 0.87 eV. In other words, H adsorption at the cus Au sites can activate the non-*cus* Au sites; the interaction between H atoms and non-*cus* Au atoms becomes stronger after four H atoms adsorb at the cus Au sites. What's more intriguing is that each end with its non-*cus* Au atoms can accommodate only one H atom, because the adsorption of the seventh H atom at the non-*cus* Au bridge site is highly unfavorable (Figure 7.2). These observations strongly indicate some magic-number nature with compositions of $Au_{22}H_2(L^8)_6$ and $Au_{22}H_6(L^8)_6$ which should correlate with their electronic structures.

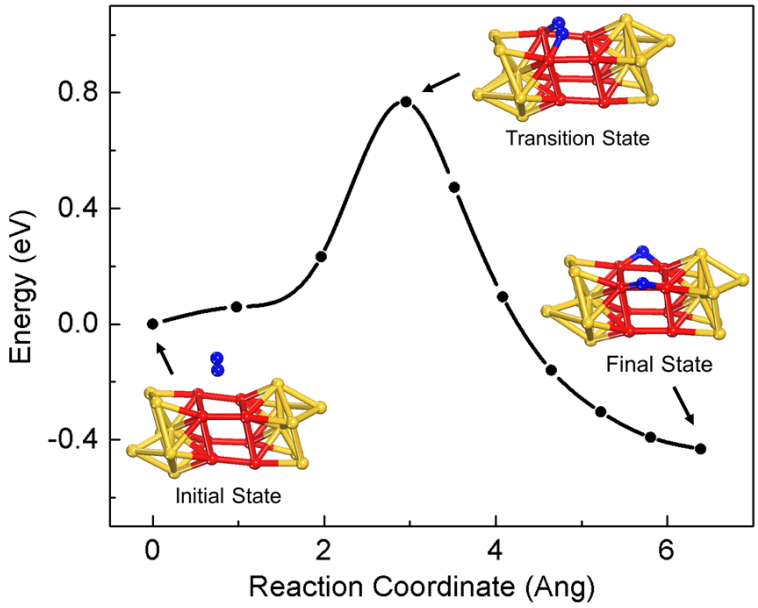

Figure 7.4. Minimum-energy path of H_2 dissociation on the $Au_{22}(L^8)_6$ cluster. Structures for initial, transition, and final states are also shown. The protecting ligands are eliminated for clarity. *Cus* Au, red; other Au, yellow; H, blue.

Another interesting implication from the highly stable $Au_{22}H_2(L^8)_6$ cluster is that $Au_{22}(L^8)_6$ can be a good catalyst for H_2 activation. To test this idea, we located the minimum-energy path for H_2 dissociation on the $Au_{22}(L^8)_6$ cluster (Figure 7.4) and the barrier was found to be 0.76 eV with a reaction energy of −0.43 eV. One can see that the H_2 molecule dissociates at the short-bridge site of the cus Au_8 center. After dissociation, H atoms adsorb at two adjacent long-bridge sites. We further calculated the barrier of H diffusion from a long-bridge site to the next to form the configuration in Figure 7.3 for $Au_{22}H_2(L^8)_6$. This barrier was found to be 0.54 eV (ΔE = −0.19 eV). These low barriers indicate that the $Au_{22}(L^8)_6$ cluster should be able to activate H_2 at room temperature.

7.2.2 Partial atomic charges of H in the $Au_{22}(L^8)_6$ clusters.

To understand the electronic structure of these clusters, we need to determine their free-electron count. Here a key question is whether H behaves as a hydride or a metal. To solve this issue, we performed Bader charge analysis. We found that charges on H in the phosphine-protected $Au_{22}(L^8)_6$ cluster are all negative (ranging from -0.17 to -0.10 |e|), like a hydride. In contract, H in thiolate-protected Au_{25} behaves as a metal with close-to-zero charges.[20] So the behavior of H in Au nanoclusters is ligand-dependent. Due to the electron-donating phosphines, charges on Au are negative (ranging from -0.23 to -0.11 |e|) for the $Au_{22}(L^8)_6$ cluster. Figure 7.5 shows the isosurface plot of charge density difference for the $Au_{22}(L^8)_6$ cluster with two adsorbed H. As one can see, electrons accumulate on the adsorbed H, while deplete on the Au atoms bonded to H. Our results of the charge analysis clearly show that H in the phosphine-protected Au nanoclusters behaves as a hydride, different from the metallic H in the thiolate-protected Au nanoclusters.

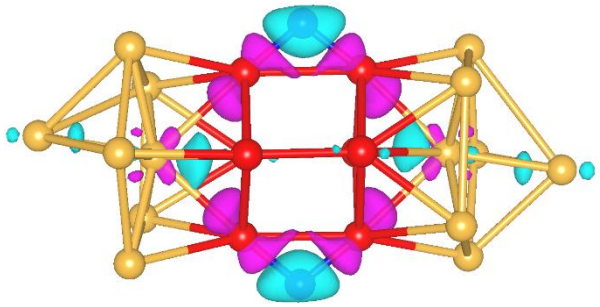

Figure 7.5. Charge density difference for the $Au_{22}(L^8)_6$ cluster with two adsorbed H at the contour level of 0.003 eV/Å^3. The charge accumulation region is in light blue and the charge depletion region is in magenta. The protecting ligands are eliminated for clarity. *Cus* Au, red; other Au, yellow; H, blue.

7.2.3 HOMO-LUMO gaps and frontier orbitals of the H-adsorbed $Au_{22}(L^8)_6$ clusters.

Since H behaves as a hydride, it can localize an electron from the core. By the electron-counting rule from the superatom complex model,[5] the free-electrons of the $Au_{22}H_n(L^8)_6$ clusters (n=0, 2, 4, 6) are shown in Table 7.1 together with the calculated HOMO-LUMO gaps. Compared with $Au_{22}(L^8)_6$ and $Au_{22}H_2(L^8)_6$, $Au_{22}H_4(L^8)_6$ has a smaller gap. This explained why the second H rather than the fourth H gave the strongest H adsorption (Figure 7.2). The $Au_{22}(L^8)_6$ cluster has 22 electrons, which does not correspond to a spherical shell closing. Instead, one can consider that each of two Au_{11} units contributes three electrons for the bonding between them. The HOMO of $Au_{22}(L^8)_6$ shows significant distribution at the interface between the two Au_{11} units (Figure 7.6). $Au_{22}H_2(L^8)_6$ has a more delocalized HOMO, but still with large densities at the interface. However, in the case of $Au_{22}H_4(L^8)_6$, the Au_{11} units do not contribute electrons to the interface. It can be viewed as a "8e +10e" system instead of "9e+9e", because the triplet state is 0.17 eV higher than the singlet state. Accordingly, the HOMO of $Au_{22}H_4(L^8)_6$ is mainly localized on the two Au_{11} units, in the absence of any interactions between them. In addition, the HOMO diagrams also indicate the electron-rich sites that would attract (additional) H atoms.

Table 7.1. Free-electron counts (N) and HOMO-LUMO gaps of the $Au_{22}H_n(L^8)_6$ clusters, n=0, 2, 4, 6.

Clusters	**$Au_{22}(L^8)_6$**	**$Au_{22}H_2(L^8)_6$**	**$Au_{22}H_4(L^8)_6$**	**$Au_{22}H_6(L^8)_6$**
N	22	20	18	16
Gap /eV	0.716	0.667	0.520	1.185

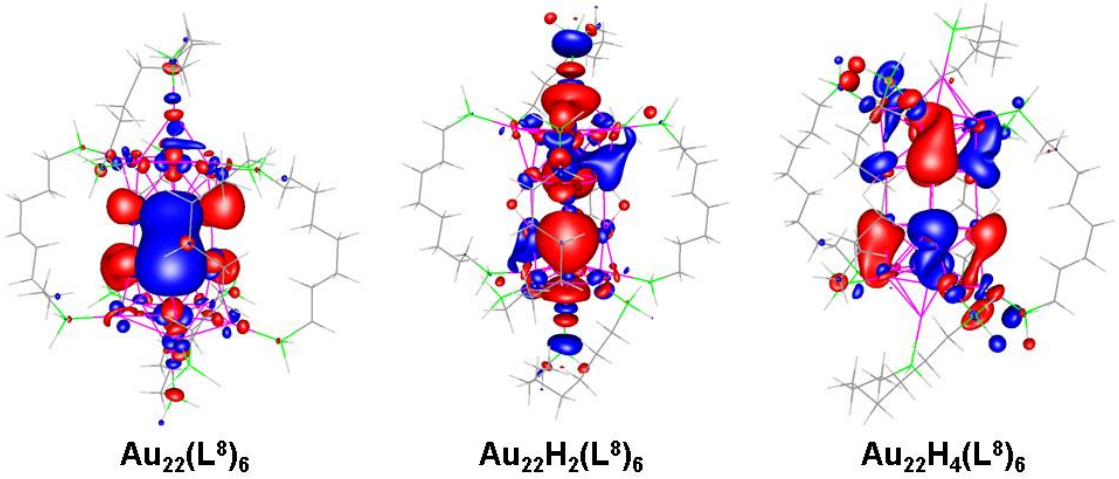

Figure 7.6. The HOMO diagrams of $Au_{22}(L^8)_6$, $Au_{22}H_2(L^8)_6$, and $Au_{22}H_4(L^8)_6$ clusters.

The $Au_{22}H_6(L^8)_6$ cluster has a much larger gap (1.185 eV). Moreover, the nondegenerate, doubly occupied HOMO of $Au_{22}H_6(L^8)_6$ resembles two spatially separated P-type orbitals, while the LUMO resembles two D-type orbitals (Figure 7.7). This suggests that $Au_{22}H_6(L^8)_6$ can be viewed as an "8*e* + 8*e*" superatom because of its 16 free electrons. We also checked the frontier orbitals of another 16-electron system, $[Au_{22}H_4(L^8)_6]^{2+}$. We found that its frontier orbitals have very similar features to those of $Au_{22}H_6(L^8)_6$ and it also has a very large gap of 1.399 eV. This "8*e* + 8*e*" superatomic shell-closing is the main reason that the $Au_{22}(L^8)_6$ cluster can absorb up to six H atoms to form the $Au_{22}H_6(L^8)_6$ cluster, even though the last two H atoms have to go to phosphine-protected gold atoms where the HOMO has more distribution (Figure 7.6).

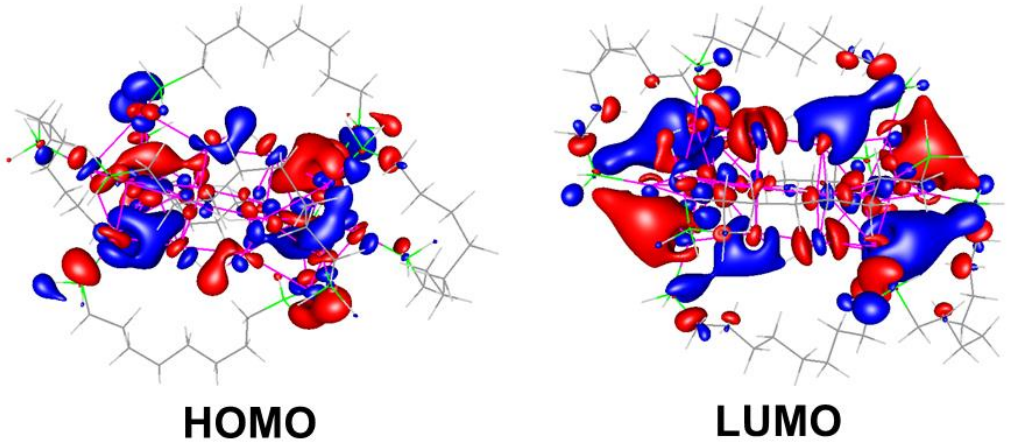

Figure 7.7. Frontier orbitals of the $Au_{22}H_6(L^8)_6$ cluster. Only one HOMO and one LUMO are shown.

To understand the difference between H-adsorbed $Au_{25}(SR)_{18}$ and $Au_{22}(L^8)_6$ clusters, the eigenvalue spectra of $Au_{25}H(SR)_{18}$ and $Au_{22}H_2(L^8)_6$ are compared in Figure 7.8a and b. We found that the orbital levels in $Au_{22}H_2(L^8)_6$ have a much lower degeneracy than those in $Au_{25}H(SR)_{18}$, due to the former's lower symmetry. By analyzing the local density of states (Figure 7.8c and d), we showed that the 1s orbital of H is mainly involved in the HOMO-1 of $Au_{25}H(SR)_{18}$ (Figure 7.8e) and the HOMO-2 of $Au_{22}H_2(L^8)_6$ (Figure 7.8f). Moreover, the HOMO-1 of $Au_{25}H(SR)_{18}$ is very delocalized, representing a superatomic P-type orbital, while the HOMO-2 of $Au_{22}H_2(L^8)_6$ is more localized to the *cus* Au atoms in the middle and the two adsorbed H atoms. This orbital picture confirms the difference of hydrogen interaction with $Au_{25}(SR)_{18}$ and $Au_{22}(L^8)_6$: the interaction with $Au_{25}(SR)_{18}$ is dictated by the superatomic electronic structure due to the lack of cus Au sites; the interaction with $Au_{22}(L^8)_6$ for the first four H atoms is rather local to and dictated by the eight cus Au atoms.

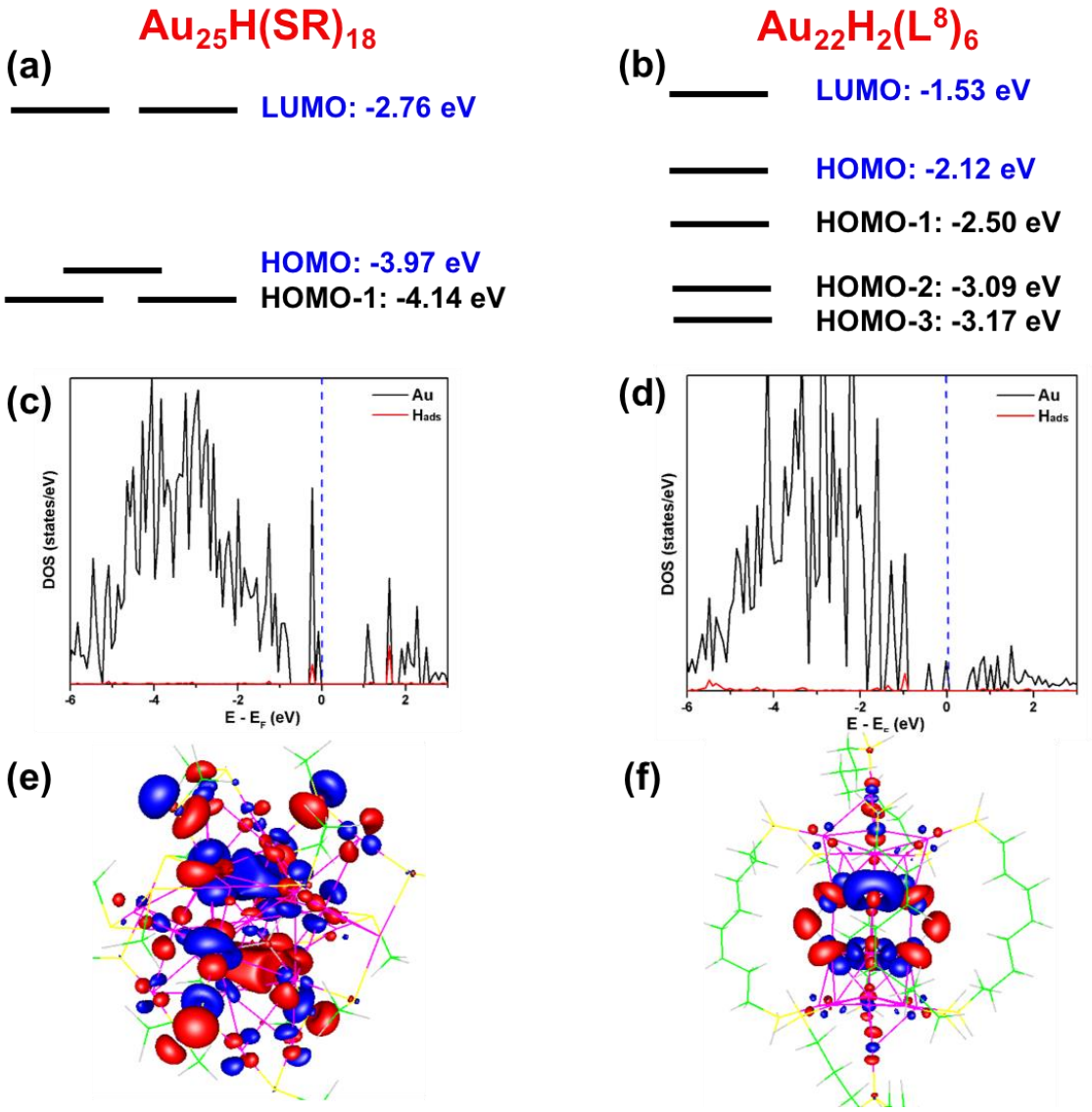

Figure 7.8. The eigenvalue spectra of $Au_{25}H(SR)_{18}$ and $Au_{22}H_2(L^8)_6$ (a and b); the local density of states (DOS) for $Au_{25}H(SR)_{18}$ and $Au_{22}H_2(L^8)_6$ (c and d) relative to their respective HOMO levels; the HOMO-1 of $Au_{25}H(SR)_{18}$ (e), and the HOMO-2 of $Au_{22}H_2(L^8)_6$ (f).

7.3 Implications of H adsorption on the $Au_{22}(L^8)_6$ cluster.

Our study of H adsorption on the $Au_{22}(L^8)_6$ cluster has important implications. First, our results show that the $Au_{22}H_2(L^8)_6$ state is thermodynamically very favorable, suggesting that it may be realized experimentally. This can in principle be realized by just bubbling

H_2 gas through a solution of the $Au_{22}H_2(L^8)_6$ cluster. Spectroscopic tools including H-NMR,[28] FT-IR,[29] and inelastic neutron scattering (INS)[30] have been demonstrated the ability in detecting hydride species in both homogeneous gold complexes and heterogeneous gold nanoparticles and can thus be utilized to experimentally verify the ability of $Au_{22}(L^8)_6$ cluster in forming stable hydride species.

Second, the four *cus*-Au and two non-*cus*-Au bridge sites are potentially active sites for the HER. The present work focuses on the thermodynamics of H adsorption on the $Au_{22}(L^8)_6$ cluster and its implication for the HER. The viability of the cluster for the HER will of course depend on the barriers of the Volmer, Heyrovsky, and Tafel steps, which warrant further studies.

7.4 Conclusions

In summary, we have investigated how H interacts with the $Au_{22}(L^8)_6$ clusters by DFT calculations. We find that six H can adsorb on the $Au_{22}(L^8)_6$ cluster: four H at the *cus* Au sites, while two H at the non-*cus* sites. More interestingly, most of the adsorbed H possess close-to-zero ΔG_H, indicating that $Au_{22}(L^8)_6$ can be a very good electrocatalyst for HER. In addition, we find that H behaves as a hydride or electron-withdrawing ligand in the $Au_{22}(L^8)_6$ cluster. This is different from the metallic H in thiolate-protected Au nanoclusters, so we conclude that the behavior of H in ligand-protected Au nanoclusters is ligand-dependent. Our study demonstrates the unique behavior of H in atomically precise Au nanoclusters and invite experimental detection of H in these clusters and test of the $Au_{22}(L^8)_6$ cluster for water splitting.

References

1. Mohtadi, R.; Orimo, S., The Renaissance of Hydrides as Energy Materials. *Nat. Rev. Mater.* **2016**, *2*, 16091.

2. Jordan, A. J.; Lalic, G.; Sadighi, J. P., Coinage Metal Hydrides: Synthesis, Characterization, and Reactivity. *Chem. Rev.* **2016**, *116*, 8318-8372.

3. Perutz, R. N.; Procacci, B., Photochemistry of Transition Metal Hydrides. *Chem. Rev.* **2016**, *116*, 8506-8544.

4. Pundt, A.; Kirchheim, R., Hydrogen in Metals: Microstructural Aspects. *Annu. Rev. Mater. Res.* **2006**, *36*, 555-608.

5. Walter, M.; Akola, J.; Lopez-Acevedo, O.; Jadzinsky, P. D.; Calero, G.; Ackerson, C. J.; Whetten, R. L.; Grönbeck, H.; Häkkinen, H., A Unified View of Ligand-Protected Gold Clusters as Superatom Complexes. *Proc. Natl. Acad. Sci.* **2008**, *105*, 9157-9162.

6. Bezman, S. A.; Churchill, M. R.; Osborn, J. A.; Wormald, J., Preparation and Crystallographic Characterization of a Hexameric Triphenylphosphinecopper Hydride Cluster. *J. Am. Chem. Soc.* **1971**, *93*, 2063-2065.

7. Lemmen, T. H.; Folting, K.; Huffman, J. C.; Caulton, K. G., Copper Polyhydrides. *J. Am. Chem. Soc.* **1985**, *107*, 7774-7775.

8. Liu, C.; Sarkar, B.; Huang, Y.-J.; Liao, P.-K.; Wang, J.-C.; Saillard, J.-Y.; Kahlal, S., Octanuclear Copper (I) Clusters Inscribed in a Se12 Icosahedron: Anion-Induced Modulation of the Core Size and Symmetry. *J. Am. Chem. Soc.* **2009**, *131*, 11222-11233.

9. Dhayal, R. S.; Liao, J.-H.; Lin, Y.-R.; Liao, P.-K.; Kahlal, S.; Saillard, J.-Y.; Liu, C., A Nanospheric Polyhydrido Copper Cluster of Elongated Triangular Orthobicupola Array: Liberation of H_2 from Solar Energy. *J. Am. Chem. Soc.* **2013**, *135*, 4704-4707.

10. Zavras, A.; Khairallah, G. N.; Connell, T. U.; White, J. M.; Edwards, A. J.; Donnelly, P. S.; O'Hair, R. A., Synthesis, Structure and Gas-Phase Reactivity of a Silver Hydride Complex $[Ag_3\{(Pph_2)_2ch_2\}_3(M_3\text{-}H)(M_3\text{-}Cl)]Bf_4$. *Angew. Chem. Int. Ed.* **2013**, *52*, 8391-8394.

11. Edwards, A. J.; Dhayal, R. S.; Liao, P. K.; Liao, J. H.; Chiang, M. H.; Piltz, R. O.; Kahlal, S.; Saillard, J. Y.; Liu, C., Chinese Puzzle Molecule: A 15 Hydride, 28 Copper Atom Nanoball. *Angew. Chem. Int. Ed.* **2014**, *53*, 7214-7218.

12. Nguyen, T.-A. D.; Jones, Z. R.; Goldsmith, B. R.; Buratto, W. R.; Wu, G.; Scott, S. L.; Hayton, T. W., A Cu25 Nanocluster with Partial Cu (0) Character. *J. Am. Chem. Soc.* **2015**, *137*, 13319-13324.

13. Daly, S.; Krstić, M.; Giuliani, A.; Antoine, R.; Nahon, L.; Zavras, A.; Khairallah, G. N.; Bonačić-Koutecký, V.; Dugourd, P.; Richard, A., Gas-Phase Vuv Photoionisation and Photofragmentation of the Silver Deuteride Nanocluster $[Ag_{10}d_8l_6]^{2+}$(L= Bis (Diphenylphosphino) Methane). A Joint Experimental and Theoretical Study. *Phys. Chem. Chem. Phys.* **2015**, *17*, 25772-25777.

14. Dhayal, R. S.; van Zyl, W. E.; Liu, C., Polyhydrido Copper Clusters: Synthetic Advances, Structural Diversity, and Nanocluster-to-Nanoparticle Conversion. *Acc. Chem. Res.* **2015**, *49*, 86-95.

15. Bootharaju, M. S.; Dey, R.; Gevers, L. E.; Hedhili, M. N.; Basset, J.-M.; Bakr, O. M., A New Class of Atomically Precise, Hydride-Rich Silver Nanoclusters Co-Protected by Phosphines. *J. Am. Chem. Soc.* **2016**, *138*, 13770-13773.

16. Jin, R.; Zeng, C.; Zhou, M.; Chen, Y., Atomically Precise Colloidal Metal Nanoclusters and Nanoparticles: Fundamentals and Opportunities. *Chem. Rev.* **2016**, *116*, 10346-10413.

17. Fang, J.; Zhang, B.; Yao, Q.; Yang, Y.; Xie, J.; Yan, N., Recent Advances in the Synthesis and Catalytic Applications of Ligand-Protected, Atomically Precise Metal Nanoclusters. *Coord. Chem. Rev.* **2016**, *322*, 1-29.

18. Chakraborty, I.; Pradeep, T., Atomically Precise Clusters of Noble Metals: Emerging Link between Atoms and Nanoparticles. *Chem. Rev.* **2017**, *117*, 8208-8271.

19. Kwak, K.; Choi, W.; Tang, Q.; Kim, M.; Lee, Y.; Jiang, D. E.; Lee, D., A Molecule-Like $PtAu_{24}(SC_6H_{13})_{18}$ Nanocluster as an Electrocatalyst for Hydrogen Production. *Nat. Commun.* **2017**, *8*, 14723.

20. Hu, G.; Tang, Q.; Lee, D.; Wu, Z.; Jiang, D. E., Metallic Hydrogen in Atomically Precise Gold Nanoclusters. *Chem. Mater.* **2017**, *29*, 4840-4847.

21. Jadzinsky, P. D.; Calero, G.; Ackerson, C. J.; Bushnell, D. A.; Kornberg, R. D., Structure of a Thiol Monolayer-Protected Gold Nanoparticle at 1.1 Å Resolution. *Science* **2007**, *318*, 430-433.

22. Heaven, M. W.; Dass, A.; White, P. S.; Holt, K. M.; Murray, R. W., Crystal Structure of the Gold Nanoparticle $[N(C_8h_{17})_4][Au_{25}(Sch_2ch_2ph)_{18}]$. *J. Am. Chem. Soc.* **2008**, *130*, 3754-3755.

23. Zhu, M.; Aikens, C. M.; Hollander, F. J.; Schatz, G. C.; Jin, R., Correlating the Crystal Structure of a Thiol-Protected Au_{25} Cluster and Optical Properties. *J. Am. Chem. Soc.* **2008**, *130*, 5883-5885.

24. Qian, H.; Eckenhoff, W. T.; Zhu, Y.; Pintauer, T.; Jin, R., Total Structure Determination of Thiolate-Protected Au38 Nanoparticles. *J. Am. Chem. Soc.* **2010**, *132*, 8280-8281.

25. Chen, J.; Zhang, Q.-F.; Bonaccorso, T. A.; Williard, P. G.; Wang, L.-S., Controlling Gold Nanoclusters by Diphospine Ligands. *J. Am. Chem. Soc.* **2013**, *136*, 92-95.

26. Wu, Z.; Hu, G.; Jiang, D.-e.; Mullins, D. R.; Zhang, Q.-F.; Allard Jr, L. F.; Wang, L.-S.; Overbury, S. H., Diphosphine-Protected Au_{22} Nanoclusters on Oxide Supports Are Active for Gas-Phase Catalysis without Ligand Removal. *Nano Lett.* **2016**, *16*, 6560-6567.

27. Nørskov, J. K.; Bligaard, T.; Logadottir, A.; Kitchin, J. R.; Chen, J. G.; Pandelov, S.; Stimming, U., Trends in the Exchange Current for Hydrogen Evolution. *J. Electrochem. Soc.* **2005**, *152*, J23-J26.

28. Roşca, D.-A.; Fernandez-Cestau, J.; Hughes, D. L.; Bochmann, M., Reactivity of Gold Hydrides: O_2 Insertion into the Au–H Bond. *Organometallics* **2014**, *34*, 2098-2101.

29. Juárez, R.; Parker, S. F.; Concepción, P.; Corma, A.; García, H., Heterolytic and Heterotopic Dissociation of Hydrogen on Ceria-Supported Gold Nanoparticles. Combined Inelastic Neutron Scattering and Ft-Ir Spectroscopic Study on the Nature and Reactivity of Surface Hydrogen Species. *Chem. Sci.* **2010**, *1*, 731-738.

30. Silverwood, I.; Rogers, S.; Callear, S.; Parker, S.; Catlow, C., Evidence for a Surface Gold Hydride on a Nanostructured Gold Catalyst. *Chem. Commun.* **2016**, *52*, 533-536.

Chapter 8

Electrocatalysis by atomically precise metal nanoclusters

Abstract

Metal nanoparticles such as gold often show high catalytic activities, but their non-uniform size distributions make it very difficult to correlate the catalytic performance with the active sites and the electronic structure of the nanoparticles. In contrast, atomically precise metal nanoclusters with their well-defined structures are a promising class of model catalysts to establish structure-activity correlations, especially for electrocatalysis where the reactions take place in ambient conditions. These metal nanoclusters can be either used as homogeneous catalysts in solutions or loaded onto solid supports as heterogeneous catalysts. This mini review highlights recent advances in electrocatalysis by atomically precise metal nanoclusters for water splitting, CO_2 reduction, and some other reactions.

8.1 Introduction

Due to their high surface-to-volume ratio, low-coordination surface atoms, and unique electronic properties, transition-metal nanoparticles have been used to catalyze many important reactions.[1-5] However, metal nanoparticles made from conventional impregnation or deposition-precipitation methods usually have non-uniform size distributions. This makes it very difficult to correlate the nanoparticle's catalytic performance to the active-site structure. Beyond being monodisperse, molecularly pure nanoparticles with atomic precision in both composition and structure would greatly facilitate establishing structure-activity relationships for nanocatalysts. Atomically precise metal nanoclusters now make this dream a reality. These clusters are made via wet-chemistry synthesis from a metal salt, ligands, and a reducing agent and have a monolayer of ligands protecting the metallic core, therefore also called monolayer protected clusters (MPCs).[6]

Great advances have been made in the past ten years in synthesis, crystallization, and structure determination of atomically precise Au, Ag, and Cu nanoclusters with tens to hundreds of metal atoms protected by ligands such as thiolates, alkynyls, phosphines and hydrides.[7-10] They have attracted great interest due to their potential applications in catalysis, biology, and nanotechnology.[9-13] Among the reported atomically precise metal nanoclusters, $Au_{25}(SR)_{18}$ is one of the most extensively studied systems, first identified in 2005[14] and later yielded to structure prediction and determination in 2008.[15-17] Great efforts have followed to dope $Au_{25}(SR)_{18}$ with other atoms such as Pt, Pd, Ag, Cu, Hg, and Cd.[18-23]

The superatom-complex model is a useful starting point to understand the electronic structure of atomically precise Au, Ag, and Cu nanoclusters.[24] The central idea is that the number of the valence electrons of the whole cluster follows the electron-shell filling of the superatomic orbitals, resulting in a series of shell-closing electron counts (or magic numbers), namely, 2, 8, 18, 20, 34, 58, etc. For example, the stability of the anionic $[Au_{25}(SR)_{18}]^-$ cluster can be explained by the superatom complex concept: its eight free electrons occupy a complete electron shell of the $(1S)^2(1P)^6$ configuration.[25] The electronic structure of the nanoclusters plays important roles in their electrocatalytic activities.

This mini review aims to highlight recent advances in electrocatalysis by using atomically precise Au and Cu nanoclusters, leveraging their well-defined geometry and unique electronic structure. We will mainly discuss water splitting by Au nanoclusters and CO_2 reduction by Cu-hydride nanocluster, followed by a brief survey of other reactions.

8.2 Hydrogen evolution reaction (HER)

Doping $Au_{25}(SR)_{18}$ with Pt changes the cluster's electronic structure and hence redox properties (Figure 8.1a and 8.1b).[23, 26] The cyclic voltammetry curves (Figure 8.1b) showed that it is much easier for the $PtAu_{24}(SR)_{18}$ nanocluster (simplified as $PtAu_{24}$) to reversibly receive and then donate two electrons than $[Au_{25}(SR)_{18}]^-$ (simplified as Au_{25}). This is because $[Au_{25}(SR)_{18}]^-$ being a magic 8-electron system has a large HOMO-LUMO gap, while the neutral $PtAu_{24}(SR)_{18}$ nanocluster is a 6-electron system that has a

low-lying LUMO (Figure 8.1a). The ease of gaining and losing two electrons suggests that $PtAu_{24}(SR)_{18}$ could be a much better catalyst than $[Au_{25}(SR)_{18}]^-$ for HER, a two-electron process. Indeed, as shown in Figure 8.1c, $PtAu_{24}$ (blue) has both a lower overpotential and a higher current for HER than Au_{25} (red).[26] The $PtAu_{24}$ cluster operated efficiently in both homogeneous and heterogeneous conditions. It generated H_2 with turnover frequencies (TOFs) of 4.8 mol H_2 (mol cat)$^{-1}$ s^{-1} in tetrahydrofuran (THF) homogeneously and 34 mol H_2 (molcat)$^{-1}$ s^{-1} in water heterogeneously, at a moderate overpotential (η=0.6 V). This activity is among the best in molecular HER catalysts.

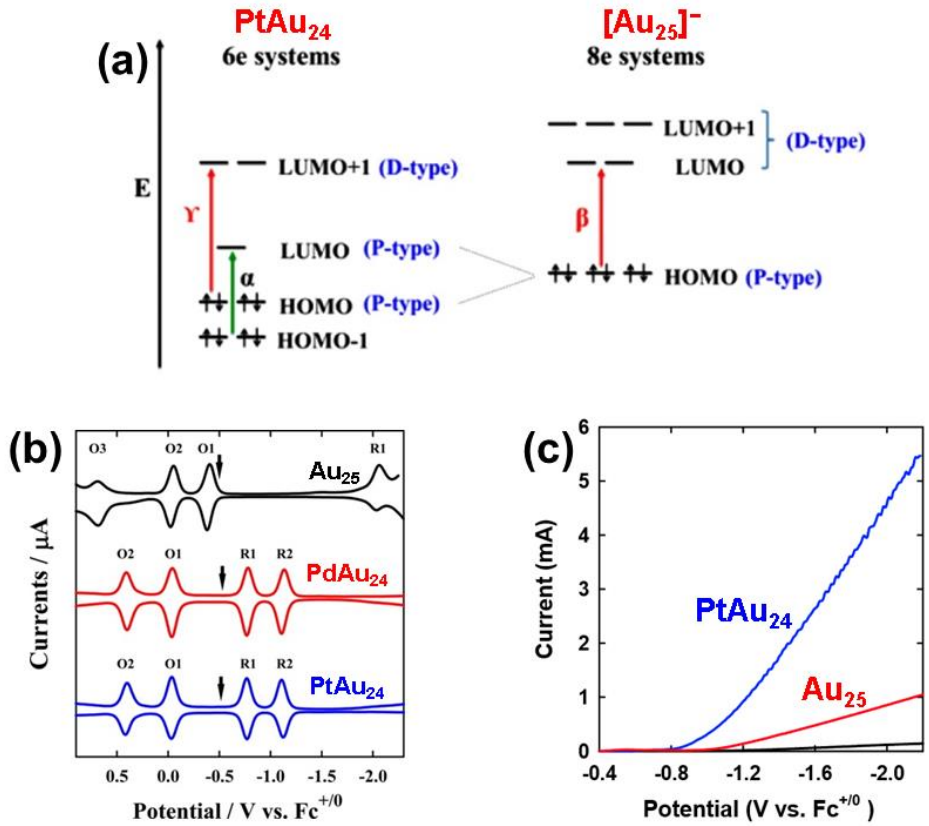

Figure 8.1. (a) Electronic energy levels of $PtAu_{24}(SR)_{18}$ (6-electron) and $[Au_{25}(SR)_{18}]^-$ (8-electron) systems. (b) Square-wave voltammetry of $Au_{25}(SR)_{18}$ (black), $PdAu_{24}(SR)_{18}$ (red), and $PtAu_{24}(SR)_{18}$ (blue). The arrows indicate solution open-circuit potentials. (c) Linear sweep voltammograms in THF (0.1 M Bu_4NPF_6) solution containing 1.0 M TFA in the absence (black) and presence of 1 mM $Au_{25}(SR)_{18}$ (red) and 1 mM $PtAu_{24}(SR)_{18}$ (blue) at 50 mVs^{-1}. (a) and (b): reprinted with permission from ref. 23. Copyright © 2015 American Chemical Society. (c): reprinted with permission from ref. 26. Copyright © 2017, Nature Publishing Group.

Mechanistic studies indicate that $PtAu_{24}$ was first reduced to $[PtAu_{24}]^{2-}$ which then reacted with one H^+ to form $[H\text{-}PtAu_{24}]^-$. This negatively charged intermediate preferably reacted with another H^+ from the electrolyte to evolve H_2. Density functional theory (DFT) calculations revealed that formation of $[H\text{-}PtAu_{24}]^-$ is thermodynamically neutral (Figure 8.2). In contrast, formation of the $H\text{-}Au_{25}$ intermediate is uphill by about 0.5 eV. In step 1, a solvated proton is transferred from THF molecules to $[PtAu_{24}]^{2-}$ to form [H-

$PtAu_{24}]^{-}$. The middle picture in Figure 8.2 shows that the H atom (green) directly interacts with the central Pt (the Pt-H distance is 1.788 Å) in $[H\text{-}PtAu_{24}]^{-}$. In step 2a, a second solvated proton is transferred from THF molecules to $[H\text{-}PtAu_{24}]^{-}$ to form [2H-$PtAu_{24}$], which then evolves H2 via the Tafel mechanism; in step 2b, a second solvated proton reacts with H in $[H\text{-}PtAu_{24}]^{-}$ to form H_2 via the Heyrovsky mechanism, which is the preferred pathway in this case. This work clearly demonstrates that doping a foreign metal into atomically precise Au nanoclusters can be a very powerful method to tune their electronic properties for HER.

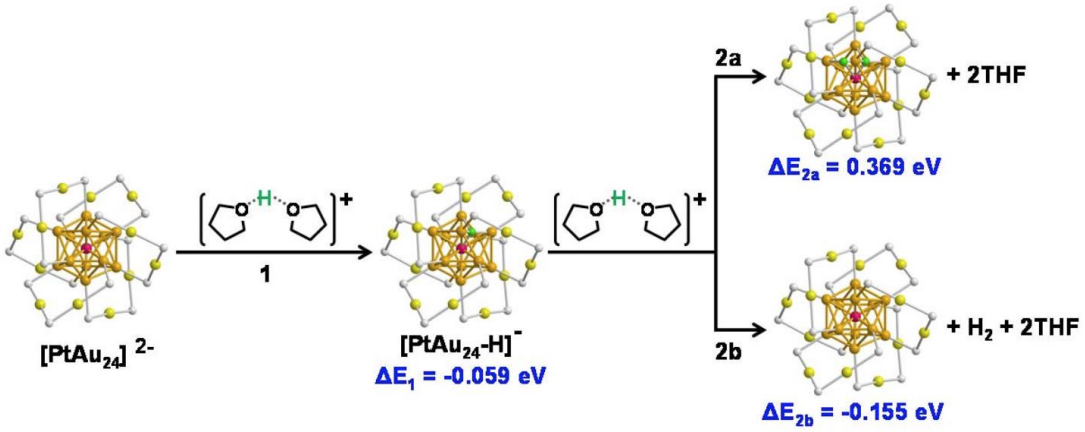

Figure 8.2. DFT reaction energies for H_2 evolution on $PtAu_{24}$. Color code: orange, Au atoms of the core; olive, Au atoms of the shell; purple, Pt; green, adsorbed H from the liquid medium; grey, S (the rest of ligand is omitted for clarity). Adapted with permission from ref. 26. Copyright © 2017, Nature Publishing Group.

Inspired by the H-Pt interaction in the $[H\text{-}PtAu_{24}]^{-}$ structure, Hu et al. systematically studied how H interacts with $[Au_{25}(SR)_{18}]^{q}$ clusters (q = -1, 0, +1) and mono-atom-doped bimetallic $[M_1Au_{24}(SR)_{18}]^{q}$ clusters (M = Pt, Pd, Ag, Cu, Hg, or Cd, q = -2, -1, 0, +1) from first-principles DFT.[27] It was found that H behaves as a metal in these clusters and contributes its 1s electron to the superatomic free-electron count. For example,

$[PtAu_{24}H_2(SR)_{18}]^0$ was found to be an 8-e system with P-type HOMO and D-type LUMO, being isoelectronic to $[Au_{25}(SR)_{18}]^-$ (Figure 8.3). The metallic nature of H in ligand-protected Au nanoclusters is in contrast with the hydride in Cu or Ag nanoclusters. This can be explained by the fact that H's electronegativity (2.2) is smaller than that of Au (2.54) but larger than that of Ag (1.93) or Cu (1.90). The calculated Gibbs free energy of H adsorption (ΔG_H), a good descriptor for HER,[28] further confirmed that $PtAu_{24}$ is the most active HER catalyst among the doped Au clusters.

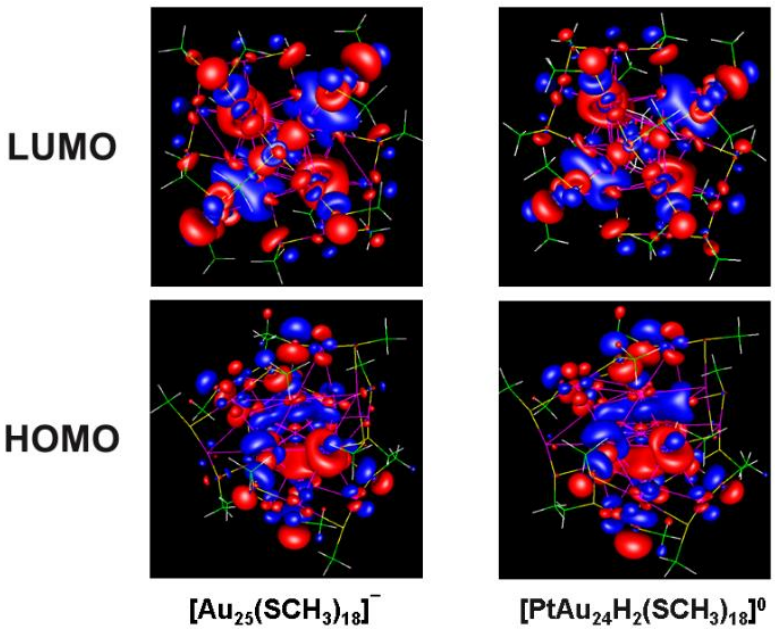

Figure 8.3. Frontier orbitals of $[Au_{25}(SR)_{18}]^-$ and $[PtAu_{24}H_2(SR)_{18}]^0$. Only one HOMO and one LUMO are shown for each cluster. Adapted with permission from ref. 27. Copyright © 2017 American Chemical Society.

Very recently, a novel composite of Au_{25} nanoclusters and MoS_2 nanosheets (Au_{25}/MoS_2) was reported to be a good electrocatalyst for HER.[29] Compared with the plain MoS_2 nanosheets, Au_{25}/MoS_2 exhibited enhanced HER activity in acidic solutions.

Moreover, it was found that not only the interface between Au nanoclusters and MoS_2 nanosheets, but also the interface between the Au cores and protecting ligands, affected the overall catalytic performance of the composite. It would be interesting to utilize DFT calculations to further explore the active sites and HER mechanisms on Au_{25}/MoS_2.

8.3 Oxygen evolution reaction (OER)

OER has been considered as the bottleneck for the overall water splitting, since its kinetic is usually sluggish.[30-31] Jin et al. utilized atomically precise Au nanoclusters to construct $Au_n/CoSe_2$ composites for OER.[32] As shown in Figure 8.4a, $Au_{25}/CoSe_2$ exhibited the best OER activity with an early onset potential and a high OER current density among $Au_{25}/CoSe_2$, $CoSe_2$, Au_{25}/CB, and Pt/CB. Figure 8.4b showed that $Au_{25}/CoSe_2$ required a smaller overpotential (0.43 V) than that of $CoSe_2$ (0.52 V) for achieving 10 mA cm^{-2}. They further found that ligand-off $Au_{25}/CoSe_2$ showed better OER performance than ligand-on $Au_{25}/CoSe_2$ due to the better interaction between Au and $CoSe_2$, which was supported by X-ray photoelectron spectroscopy (XPS) analysis. The electronic interaction between Au nanoclusters and $CoSe_2$ nanosheets was found to be critical to the OER performance. To further understand the high OER activity, they performed periodic DFT calculations. To model the $Au/CoSe_2$ interaction, they replaced a Se atom on a $CoSe_2$ surface with Au and found that formation of O* intermediate and desorption of O_2 became more favorable on the model $Au/CoSe_2$ catalyst.

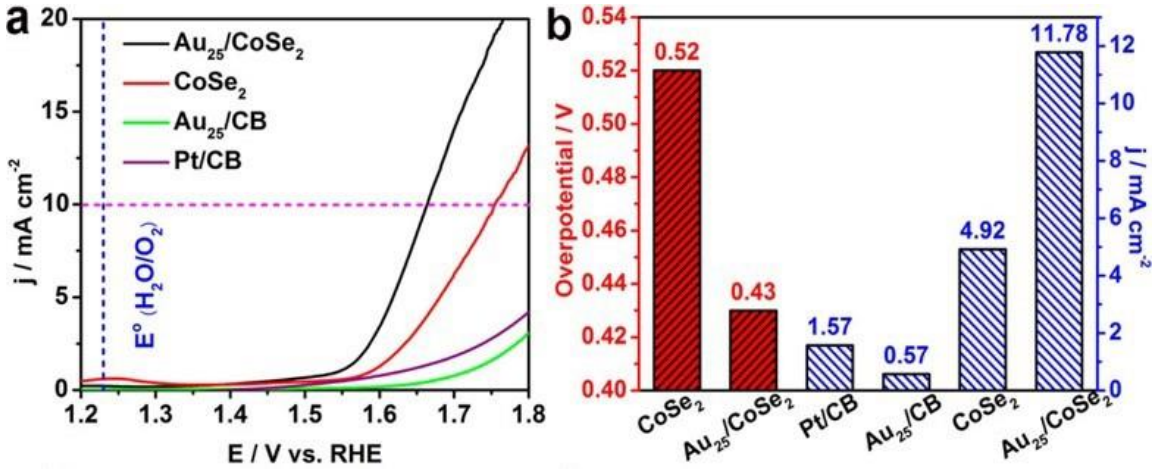

Figure 8.4. (a) OER polarization curves for $Au_{25}/CoSe_2$, $CoSe_2$, Au_{25}/CB, and Pt/CB. (b) Comparison of the overpotential required for achieving the current density of 10 mA cm^{-2}, and the current density at the overpotential of 0.45 V for $Au_{25}/CoSe_2$, $CoSe_2$, Au_{25}/CB, and Pt/CB catalysts. Reprinted with permission from ref. 32. Copyright © 2017 American Chemical Society.

8.4 Electrochemical reduction of CO_2

Electrochemical reduction of CO_2 to fuels and chemicals has gained great interest recently as a way to leverage renewable energy for CO_2 utilization.[33-34] It was found that Au_{25} exhibited excellent activity for electroreduction of CO_2 to CO within 90 mV of the thermodynamic limit.[35] On the other hand, Cu is a much better known electrocatalyst for converting CO_2 to hydrocarbons at high overpotentials, while producing H_2 at low overpotentials.[36] Although many nanostructured Cu catalysts have been used for CO_2 electroreduction, atomically precise Cu clusters have not been tried until Jiang, Lee, Liu, and their coworkers reported the first successful example from a joint theory-synthesis-electrocatalysis effort, based on the structurally precise Cu-hydride nanocluster $Cu_{32}H_{20}L_{12}$ (L is a dithiophosphate ligand) (Figure 8.5a).[37]

From the DFT calculations, they found that the lattice-hydride channel (CO_2 first reacting with the lattice hydrides) was more facile than the proton-reduction channel

(CO_2 first reacting with the proton from solution and electron from the electrode). By comparing HCOOH and CO formation on $Cu_{32}H_{20}L_{12}$ with the lattice-hydride mechanism, they predicted that HCOOH rather than CO would be the main product. Figure 8.5b showed the proposed overall mechanism of HCOOH formation from CO_2 reduction. As one can see, HCOOH formation proceeded through two steps of lattice-hydride reduction: CO_2 reacted directly with the capping hydride to form HCOO*, which then reacted with another interstitial hydride to form HCOOH. The reacted hydrides can be regenerated by proton reduction. Since HER is the major competing reaction for electrochemical CO_2 reduction at low overpotentials, the authors also evaluated HER on the $Cu_{32}H_{20}L_{12}$ cluster and found that at low overpotentials, HCOOH formation was kinetically preferred over HER.

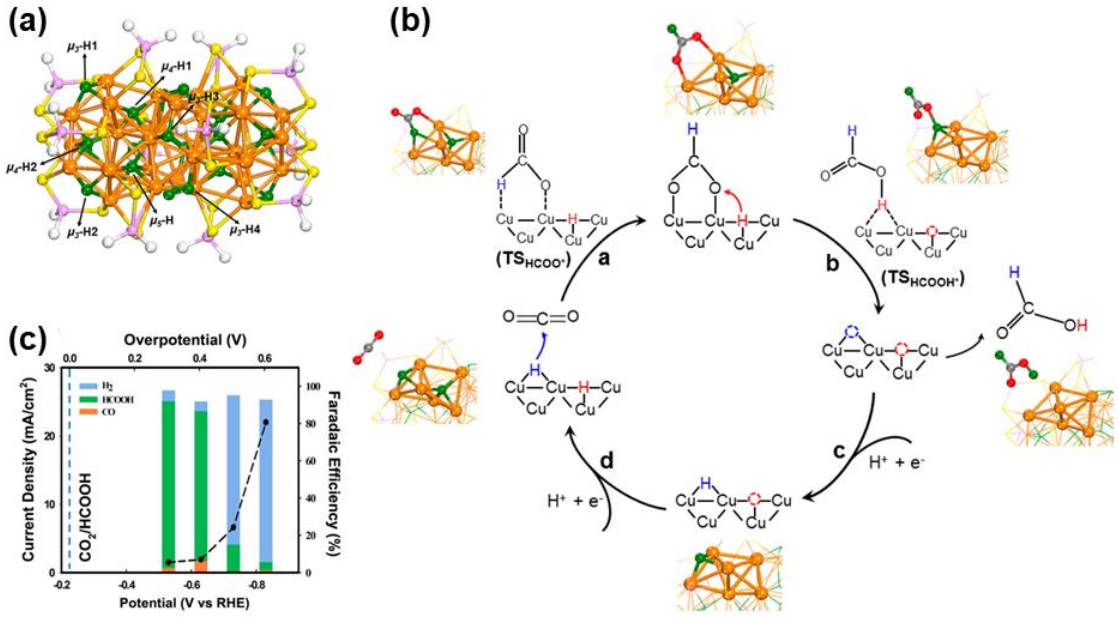

Figure 8.5. (a) Structure of the $Cu_{32}H_{20}L_{12}$ nanocluster (L = S_2PH_2). Color code: orange, Cu; green, hydride; yellow, S; purple, P; white, H on the dithiophosphate ligands. Different types of hydrides are indicated by the arrows. (b) Overall mechanism of HCOOH formation on $Cu_{32}H_{20}L_{12}$ via the lattice-hydride channel. (c) Average current densities (black circles) and cumulative Faradaic efficiencies for H_2, HCOOH, and CO (stacked bars) obtained at different overpotentials. Controlled potential electrolysis was conducted for 90 min in 0.1 M $KHCO_3$ and 0.4 M KCl (pH 6.8) on a Cu_{32}/C/GDL electrode (1 cm^2). Reprinted with permission from ref. 37. Copyright © 2017 American Chemical Society.

To verify the theoretical predictions, they synthesized the $Cu_{32}H_{20}L_{12}$ cluster and examined its catalytic activity for CO_2 reduction by controlled potential electrolysis. The experimental results (Figure 8.5c) showed that $Cu_{32}H_{20}L_{12}$ predominantly produced HCOOH at low overpotentials, with minor amounts of CO and H_2, in good agreement with the theoretical predictions. Unlike flat Cu surfaces or large Cu nanoparticles, where H_2 was the major product at low overpotentials,[38-39] the $Cu_{32}H_{20}L_{12}$ cluster produced HCOOH due to the presence of the negatively charged hydride. This is the first time that lattice-hydride mechanism has been proposed for electrochemical reduction of CO_2 on a

metal nanocluster. It is expected that the lattice-hydride mechanism can extend to other hydride-containing transition-metal nanoclusters, for example hydride-rich Ag clusters.[40]

8.5 Other electrochemical reactions

Oxygen reduction reaction (ORR) is a key reaction in the development of fuel cell technology, and atomically precise Au and Cu nanoclusters have received research attention as novel ORR catalysts. Chen et al. investigated Au_{11}, Au_{25}, Au_{55}, and Au_{140} nanoclusters for ORR and found that the activities of the Au nanoclusters exhibited a strong size dependence; the smaller nanocluster showed higher activity.[41] They also studied Cu_nL_4 nanoclusters ($n \leq 8$, L = $C_7H_9N_2S$) for ORR, and found that the onset potential of O_2 reduction was comparable to that of Au_{11}.[42] Recently, they loaded Au_{102}(p-MBA)$_{44}$ nanoclusters onto porous carbon nanosheets, and found that the ligand-off nanoclusters demonstrated excellent activity for ORR.[43] Lu and coworkers studied selective electrochemical reduction of O_2 to H_2O_2 by using Au_{25} nanocluster. The influence of the charge state of Au_{25} on the reactivity was observed; the maximum H_2O_2 production rate was obtained from the negatively charged $[Au_{25}]^-$.[44] Jin et al. recently evaluated the electrocatalytic performance of the heavily Ag-doped $[Ag_xAu_{25-x}(SR)_{18}]^-$ nanoclusters ($x \sim 21$) for ORR and found that the ligand-off nanoclusters possess a much higher mass activity than ligand-on nanoclusters.[45] Besides ORR, Lee et al. evaluated Au_{25} nanocluster as an electrocatalyst for the oxidation of ascorbic acid (AA) and dopamine (DA). They observed a pH-dependent electrocatalytic activity and developed an amperometric method for sensing AA and DA based on this feature.[46]

8.6 Future perspectives

The electrocatalytic applications of atomically precise metal nanoclusters are still in their infancy, but the few recent examples discussed above indicate their great promise. Looking ahead, we see several interesting directions to fully realize the potential of atomically precise nanoclusters in electrocatalysis. First, synthesis of doped bimetallic and trimetallic nanoclusters has advanced steadily in the past five years.[47-52] In several cases, their structures have even been solved. This provides a huge opportunity to correlate their geometry structure, electronic structure, and electrocatalytic activity by closely integrating theory and experiment. Second, the lattice hydride mechanism that has been proposed for CO_2 reduction needs further experimental characterization such as NMR and mechanistic investigation such as isotope labelling. Broadly speaking, the roles of hydrogen and its interaction with the metal catalyst during CO_2 reduction deserve more attention. Third, more Cu-H and Ag-H clusters that have been synthesized recently should be tested for CO_2 electroreduction given the recent success with $Cu_{32}H_{20}L_{12}$. To conclude, impressive progress has been made in the past few years in using atomically precise Au and Cu nanoclusters for electrocatalysis, like a sun just emerging from the horizon. We think that this is an area ready for accelerated growth, into a morning sun.

References

1. Hervés, P.; Pérez-Lorenzo, M.; Liz-Marzán, L. M.; Dzubiella, J.; Lu, Y.; Ballauff, M., Catalysis by Metallic Nanoparticles in Aqueous Solution: Model Reactions. *Chem. Soc. Rev.* **2012**, *41*, 5577-5587.

2. Campbell, C. T., The Energetics of Supported Metal Nanoparticles: Relationships to Sintering Rates and Catalytic Activity. *Acc. Chem. Res.* **2013**, *46*, 1712-1719.

3. Linic, S.; Christopher, P.; Xin, H.; Marimuthu, A., Catalytic and Photocatalytic Transformations on Metal Nanoparticles with Targeted Geometric and Plasmonic Properties. *Acc. Chem. Res.* **2013**, *46*, 1890-1899.

4. Zhao, P.; Feng, X.; Huang, D.; Yang, G.; Astruc, D., Basic Concepts and Recent Advances in Nitrophenol Reduction by Gold-and Other Transition Metal Nanoparticles. *Coord. Chem. Rev.* **2015**, *287*, 114-136.

5. Navalon, S.; Dhakshinamoorthy, A.; Alvaro, M.; Garcia, H., Metal Nanoparticles Supported on Two-Dimensional Graphenes as Heterogeneous Catalysts. *Coord. Chem. Rev.* **2016**, *312*, 99-148.

6. Templeton, A. C.; Wuelfing, W. P.; Murray, R. W., Monolayer-Protected Cluster Molecules. *Acc. Chem. Res.* **2000**, *33*, 27-36.

7. Dhayal, R. S.; van Zyl, W. E.; Liu, C., Polyhydrido Copper Clusters: Synthetic Advances, Structural Diversity, and Nanocluster-to-Nanoparticle Conversion. *Acc. Chem. Res.* **2015**, *49*, 86-95.

8. Fang, J.; Zhang, B.; Yao, Q.; Yang, Y.; Xie, J.; Yan, N., Recent Advances in the Synthesis and Catalytic Applications of Ligand-Protected, Atomically Precise Metal Nanoclusters. *Coord. Chem. Rev.* **2016**, *322*, 1-29.

9. Jin, R.; Zeng, C.; Zhou, M.; Chen, Y., Atomically Precise Colloidal Metal Nanoclusters and Nanoparticles: Fundamentals and Opportunities. *Chem. Rev.* **2016**, *116*, 10346-10413.

10. Chakraborty, I.; Pradeep, T., Atomically Precise Clusters of Noble Metals: Emerging Link between Atoms and Nanoparticles. *Chem. Rev.* **2017**, *117*, 8208-8271.

11. Li, G.; Jin, R., Atomically Precise Gold Nanoclusters as New Model Catalysts. *Acc. Chem. Res.* **2013**, *46*, 1749-1758.

12. Wu, Z.; Hu, G.; Jiang, D. E.; Mullins, D. R.; Zhang, Q. F.; Allard Jr, L. F.; Wang, L. S.; Overbury, S. H., Diphosphine-Protected Au_{22} Nanoclusters on Oxide Supports Are

Active for Gas-Phase Catalysis without Ligand Removal. *Nano Lett.* **2016**, *16*, 6560-6567.

13. Hu, G.; Jin, R.; Jiang, D. E., Beyond the Staple Motif: A New Order at the Thiolate–Gold Interface. *Nanoscale* **2016**, *8*, 20103-20110.

14. Negishi, Y.; Nobusada, K.; Tsukuda, T., Glutathione-Protected Gold Clusters Revisited: Bridging the Gap between Gold (I)− Thiolate Complexes and Thiolate-Protected Gold Nanocrystals. *J. Am. Chem. Soc* **2005**, *127*, 5261-5270.

15. Akola, J.; Walter, M.; Whetten, R. L.; Häkkinen, H.; Grönbeck, H., On the Structure of Thiolate-Protected Au_{25}. *J. Am. Chem. Soc.* **2008**, *130*, 3756-3757.

16. Heaven, M. W.; Dass, A.; White, P. S.; Holt, K. M.; Murray, R. W., Crystal Structure of the Gold Nanoparticle $[N(C_8h_{17})_4][Au_{25}(Sch_2ch_2ph)_{18}]$. *J. Am. Chem. Soc.* **2008**, *130*, 3754-3755.

17. Zhu, M.; Aikens, C. M.; Hollander, F. J.; Schatz, G. C.; Jin, R., Correlating the Crystal Structure of a Thiol-Protected Au_{25} Cluster and Optical Properties. *J. Am. Chem. Soc.* **2008**, *130*, 5883-5885.

18. Qian, H.; Jiang, D. E.; Li, G.; Gayathri, C.; Das, A.; Gil, R. R.; Jin, R., Monoplatinum Doping of Gold Nanoclusters and Catalytic Application. *J. Am. Chem. Soc* **2012**, *134*, 16159-16162.

19. Negishi, Y.; Munakata, K.; Ohgake, W.; Nobusada, K., Effect of Copper Doping on Electronic Structure, Geometric Structure, and Stability of Thiolate-Protected Au_{25} Nanoclusters. *J. Phys. Chem. Lett.* **2012**, *3*, 2209-2214.

20. Yamazoe, S.; Kurashige, W.; Nobusada, K.; Negishi, Y.; Tsukuda, T., Preferential Location of Coinage Metal Dopants (M= Ag or Cu) in $[Au_{25-X}m_x(Sc_2h_4ph)_{18}]^-(X\sim 1)$ as Determined by Extended X-Ray Absorption Fine Structure and Density Functional Theory Calculations. *J. Phys. Chem. C* **2014**, *118*, 25284-25290.

21. Wang, S.; Song, Y.; Jin, S.; Liu, X.; Zhang, J.; Pei, Y.; Meng, X.; Chen, M.; Li, P.; Zhu, M., Metal Exchange Method Using Au25 Nanoclusters as Templates for Alloy Nanoclusters with Atomic Precision. *J. Am. Chem. Soc.* **2015**, *137*, 4018-4021.

22. Yao, C.; Lin, Y. J.; Yuan, J.; Liao, L.; Zhu, M.; Weng, L. H.; Yang, J.; Wu, Z., Mono-Cadmium Vs Mono-Mercury Doping of Au_{25} Nanoclusters. *J. Am. Chem. Soc.* **2015**, *137*, 15350-15353.

23. Kwak, K.; Tang, Q.; Kim, M.; Jiang, D. E.; Lee, D., Interconversion between Superatomic 6-Electron and 8-Electron Configurations of $M@Au_{24}(Sr)_{18}$ Clusters (M= Pd, Pt). *J. Am. Chem. Soc* **2015**, *137*, 10833-10840.

24. Walter, M.; Akola, J.; Lopez-Acevedo, O.; Jadzinsky, P. D.; Calero, G.; Ackerson, C. J.; Whetten, R. L.; Grönbeck, H.; Häkkinen, H., A Unified View of Ligand-Protected Gold Clusters as Superatom Complexes. *Proc. Natl. Acad. Sci.* **2008**, *105*, 9157-9162.

25. Tofanelli, M. A.; Ackerson, C. J., Superatom Electron Configuration Predicts Thermal Stability of $Au_{25}(Sr)_{18}$ Nanoclusters. *J. Am. Chem. Soc.* **2012**, *134*, 16937-16940.
26. Kwak, K.; Choi, W.; Tang, Q.; Kim, M.; Lee, Y.; Jiang, D. E.; Lee, D., A Molecule-Like $PtAu_{24}(SC_6H_{13})_{18}$ Nanocluster as an Electrocatalyst for Hydrogen Production. *Nat. Commun.* **2017**, *8*, 14723.

27. Hu, G.; Tang, Q.; Lee, D.; Wu, Z.; Jiang, D. E., Metallic Hydrogen in Atomically Precise Gold Nanoclusters. *Chem. Mater.* **2017**, *29*, 4840-4847.

28. Nørskov, J. K.; Bligaard, T.; Logadottir, A.; Kitchin, J. R.; Chen, J. G.; Pandelov, S.; Stimming, U., Trends in the Exchange Current for Hydrogen Evolution. *J. Electrochem. Soc.* **2005**, *152*, J23-J26.

29. Zhao, S.; Jin, R.; Song, Y.; Zhang, H.; House, S. D.; Yang, J. C.; Jin, R., Atomically Precise Gold Nanoclusters Accelerate Hydrogen Evolution over Mos2 Nanosheets: The Dual Interfacial Effect. *Small* **2017**, *13*.

30. Kanan, M. W.; Nocera, D. G., In Situ Formation of an Oxygen-Evolving Catalyst in Neutral Water Containing Phosphate and Co^{2+}. *Science* **2008**, *321*, 1072-1075.

31. Suntivich, J.; May, K. J.; Gasteiger, H. A.; Goodenough, J. B.; Shao-Horn, Y., A Perovskite Oxide Optimized for Oxygen Evolution Catalysis from Molecular Orbital Principles. *Science* **2011**, *334*, 1383-1385.

32. Zhao, S.; Jin, R.; Abroshan, H.; Zeng, C.; Zhang, H.; House, S. D.; Gottlieb, E.; Kim, H. J.; Yang, J. C.; Jin, R., Gold Nanoclusters Promote Electrocatalytic Water Oxidation at the Nanocluster/Cose2 Interface. *J. Am. Chem. Soc* **2017**, *139*, 1077-1080.

33. Benson, E. E.; Kubiak, C. P.; Sathrum, A. J.; Smieja, J. M., Electrocatalytic and Homogeneous Approaches to Conversion of Co_2 to Liquid Fuels. *Chem. Soc. Rev.* **2009**, *38*, 89-99.

34. Whipple, D. T.; Kenis, P. J., Prospects of Co_2 Utilization Via Direct Heterogeneous Electrochemical Reduction. *J. Phys. Chem. Lett.* **2010**, *1*, 3451-3458.

35. Kauffman, D. R.; Alfonso, D.; Matranga, C.; Qian, H.; Jin, R., Experimental and Computational Investigation of Au_{25} Clusters and Co_2: A Unique Interaction and Enhanced Electrocatalytic Activity. *J. Am. Chem. Soc* **2012**, *134*, 10237-10243.

36. Gattrell, M.; Gupta, N.; Co, A., A Review of the Aqueous Electrochemical Reduction of Co_2 to Hydrocarbons at Copper. *J. Electroanal. Chem.* **2006**, *594*, 1-19.

37. Tang, Q.; Lee, Y.; Li, D. Y.; Choi, W.; Liu, C.; Lee, D.; Jiang, D. E., Lattice-Hydride Mechanism in Electrocatalytic CO_2 Reduction by Structurally Precise Copper-Hydride Nanoclusters. *J. Am. Chem. Soc.* **2017**, *139*, 9728-9736.

38. Hori, Y.; Murata, A.; Takahashi, R., Formation of Hydrocarbons in the Electrochemical Reduction of Carbon Dioxide at a Copper Electrode in Aqueous Solution. *J. Chem. Soc., Faraday Trans. 1* **1989**, *85*, 2309-2326.

39. Reske, R.; Mistry, H.; Behafarid, F.; Roldan Cuenya, B.; Strasser, P., Particle Size Effects in the Catalytic Electroreduction of CO_2 on Cu Nanoparticles. *J. Am. Chem. Soc.* **2014**, *136*, 6978-6986.

40. Bootharaju, M. S.; Dey, R.; Gevers, L. E.; Hedhili, M. N.; Basset, J.-M.; Bakr, O. M., A New Class of Atomically Precise, Hydride-Rich Silver Nanoclusters Co-Protected by Phosphines. *J. Am. Chem. Soc.* **2016**, *138*, 13770-13773.

41. Chen, W.; Chen, S., Oxygen Electroreduction Catalyzed by Gold Nanoclusters: Strong Core Size Effects. *Angew. Chem. Int. Ed.* **2009**, *48*, 4386-4389.

42. Wei, W.; Lu, Y.; Chen, W.; Chen, S., One-Pot Synthesis, Photoluminescence, and Electrocatalytic Properties of Subnanometer-Sized Copper Clusters. *J. Am. Chem. Soc.* **2011**, *133*, 2060-2063.

43. Wang, Q.; Wang, L.; Tang, Z.; Wang, F.; Yan, W.; Yang, H.; Zhou, W.; Li, L.; Kang, X.; Chen, S., Oxygen Reduction Catalyzed by Gold Nanoclusters Supported on Carbon Nanosheets. *Nanoscale* **2016**, *8*, 6629-6635.

44. Lu, Y.; Jiang, Y.; Gao, X.; Chen, W., Charge State-Dependent Catalytic Activity of $[Au_{25}(Sc_{12}h_{25})_{18}]$ Nanoclusters for the Two-Electron Reduction of Dioxygen to Hydrogen Peroxide. *Chem. Commun.* **2014**, *50*, 8464-8467.

45. Jin, R.; Jin, R.; Zhao, S.; Liu, C.; Zhou, M.; Panapitiya, G.; Xing, Y.; Rosi, N. L.; Lewis, J. P., Controlling Ag-Doping in [Agxau25-X (Sc6h11) 18]–Nanoclusters, Cryogenic Optical, Electronic and Electrocatalytic Properties. *Nanoscale* **2017**.

46. Kumar, S. S.; Kwak, K.; Lee, D., Amperometric Sensing Based on Glutathione Protected Au25 Nanoparticles and Their Ph Dependent Electrocatalytic Activity. *Electroanal.* **2011**, *23*, 2116-2124.

47. Jin, R.; Nobusada, K., Doping and Alloying in Atomically Precise Gold Nanoparticles. *Nano Res.* **2014**, *7*, 285.

48. Yang, H.; Wang, Y.; Yan, J.; Chen, X.; Zhang, X.; Häkkinen, H.; Zheng, N., Structural Evolution of Atomically Precise Thiolated Bimetallic $[Au_{12+N}cu_{32}(Sr)_{30+N}]^{4-}$ (N= 0, 2, 4, 6) Nanoclusters. *J. Am. Chem. Soc.* **2014**, *136*, 7197-7200.

49. Yang, S.; Wang, S.; Jin, S.; Chen, S.; Sheng, H.; Zhu, M., A Metal Exchange Method for Thiolate-Protected Tri-Metal $M_1ag_xau_{24-x}(Sr)_{18}^0$ (M= Cd/Hg) Nanoclusters. *Nanoscale* **2015**, *7*, 10005-10007.

50. Kang, X.; Xiong, L.; Wang, S.; Yu, H.; Jin, S.; Song, Y.; Chen, T.; Zheng, L.; Pan, C.; Pei, Y., Shape-Controlled Synthesis of Trimetallic Nanoclusters: Structure Elucidation and Properties Investigation. *Chem. Eur. J.* **2016**, *22*, 17145-17150.

51. Li, Q.; Lambright, K. J.; Taylor, M. G.; Kirschbaum, K.; Luo, T.-Y.; Zhao, J.; Mpourmpakis, G.; Mokashi-Punekar, S.; Rosi, N. L.; Jin, R., Reconstructing the Surface of Gold Nanocluster by Cadmium Doping. *J. Am. Chem. Soc.* **2017**.

52. Wan, X. K.; Cheng, X. L.; Tang, Q.; Han, Y. Z.; Hu, G.; Jiang, D. E.; Wang, Q. M., Atomically Precise Bimetallic $Au_{19}cu_{30}$ Nanocluster with an Icosidodecahedral Cu_{30} Shell and an Alkynyl–Cu Interface. *J. Am. Chem. Soc.* **2017**, *139*, 9451-9454.

Chapter 9

First Principles Insight into H_2 Activation on the Surfaces of Different TiO_2 Polymorphs

Abstract

Hydrogen interaction with the TiO_2 surfaces is important in many catalytic and photocatalytic reactions. However, the mechanisms of H_2 dissociation on TiO_2 surfaces remain unclear. Here, we study H_2 activation on the surfaces of different TiO_2 polymorphs, namely rutile TiO_2(110), anatase TiO_2(101), and brookite TiO_2(210), by first-principles density functional theory (DFT). We find that for all the three surfaces the heterolytic pathway is kinetically more favorable leading to a hydride and a hydroxyl, although the homolytic dissociation of H_2 is thermodynamically more favorable leading to two hydroxyls. For rutile TiO_2(110) and brookite TiO_2(210), the hydrides which are produced by the heterolytic dissociation of H_2 can easily transfer from Ti to O, yielding the homolytic products. However, for anatase TiO_2(101), the barrier of hydrogen transfer form Ti to O is very high. This indicates that hydrides on anatase TiO_2(101) can be kinetically stabilized. Thus, it is expected that hydrides on anatase TiO_2(101) can be detected experimentally. Our study sheds light on the mechanisms of H_2 dissociation on TiO_2 and provides rational for the existence of hydrides on TiO_2 or other reducible metal oxides which may facilitate hydrogenation reaction.

9.1 Introduction

Titanium dioxide (TiO_2) is one of the most extensively investigated metal oxide materials, due to its widespread use in many fields, e.g., catalysis, solar energy conversion, and biomaterials.[1-4] There are three main crystallographic forms for TiO_2, namely, rutile (tetragonal, $P4_2/mnm$), anatase (tetragonal, $I4_1/amd$), and brookite (orthorhombic, *Pbca*).[5] While rutile is thermodynamically the most stable bulk phase, most nanomaterials are in anatase form.[6] Moreover, the anatase phase appears to be more stable than rutile below a particle size of about 14 nm, which is due to the lower surface energy of anatase.[7-8] Among the three crystallographic forms of TiO_2, brookite has been rarely studied and is far less understood than rutile and anatase, mainly because of the difficulties in preparing significant quantities of good-quality brookite TiO_2.[9-10]

Hydrogen interaction with the TiO_2 surfaces is an important process in many phenomena and applications.[11-15] It has been shown that molecular hydrogen does not interact strongly with the rutile TiO_2(110) surface,[16-17] while atomic hydrogen readily sticks to the surface oxygen atoms.[18-20] Also, the hydrogenation of anatase TiO_2 surfaces has been reported theoretically.[21-23] However, the mechanisms of H_2 dissociation on TiO_2 surfaces haven't been systematically studied and keep unclear. Molecular hydrogen dissociation on metal oxides can go through homolytic or heterolytic pathway.[24] The homolytic (radicalary) dissociation of H_2 produces two H atoms at two O sites, leading to the formation of two O–H groups. The heterolytic (polar) dissociation of H_2 produces a hydride (H^-) adsorbed on metal, and a proton (H^+) adsorbed on O. So far, the mechanistic proposal for H_2 dissociation on metal oxides has been based on the infrared spectra. The

presence of both O–H and M–H bands indicates the heterolytic pathway, while the presence of only O–H bands indicates the homolytic pathway.[25-28]

Based on the infrared spectra of TiO_2, a homolytic pathway has been proposed for H_2 dissociation on TiO_2, since no IR signal can be attributed to the Ti−H bond.[29-30] However, both low-energy ion scattering (LEIS) and electronically stimulated desorption (ESD) indicated the presence of titanium hydride species.[31-32] In addition, recently by using magic angle spinning nuclear magnetic resonance (MAS–^{1}H NMR), attenuated total reflection Fourier transform infrared (ATR-FTIR), and electron-spin resonance (ESR), the accumulative formation of Ti–H species on the TiO_2 surface has been observed, and it is revealed to be the intrinsic cause of the power conversion efficiency (PCE) failure of TiO_2-based dye-sensitization devices.[4]

The great importance of hydrogen interaction with TiO_2 combined with the contradictory experimental results of hydrogen on TiO_2 surfaces motivate us to use computational methods to shed light on this issue. In this work, we report a density functional theory (DFT) study of H_2 activations on different TiO_2 polymorphs, namely, rutile TiO_2(110), anatase TiO_2(101) and brookite TiO_2(210). Our theoretical results reveal the mechanisms of H_2 dissociation on the TiO_2 surfaces, and have important implications for the detection of hydrides on TiO_2 or other reducible metal oxides and the use of metal oxide catalysts for hydrogenation reactions.

9.2 Results and discussion

As discussed in the introduction, TiO_2 exists in three polymorphs (rutile, anatase, and brookite) with different structural properties under ambient conditions. Rutile TiO_2(110), anatase TiO_2(101), and brookite TiO_2(210) surfaces are the most stable and usually most exposed surfaces for each crystallographic form.[33] Hence, in the present work, we examined H_2 dissociation on these three surfaces, and Figure 9.1 shows their geometry structures.

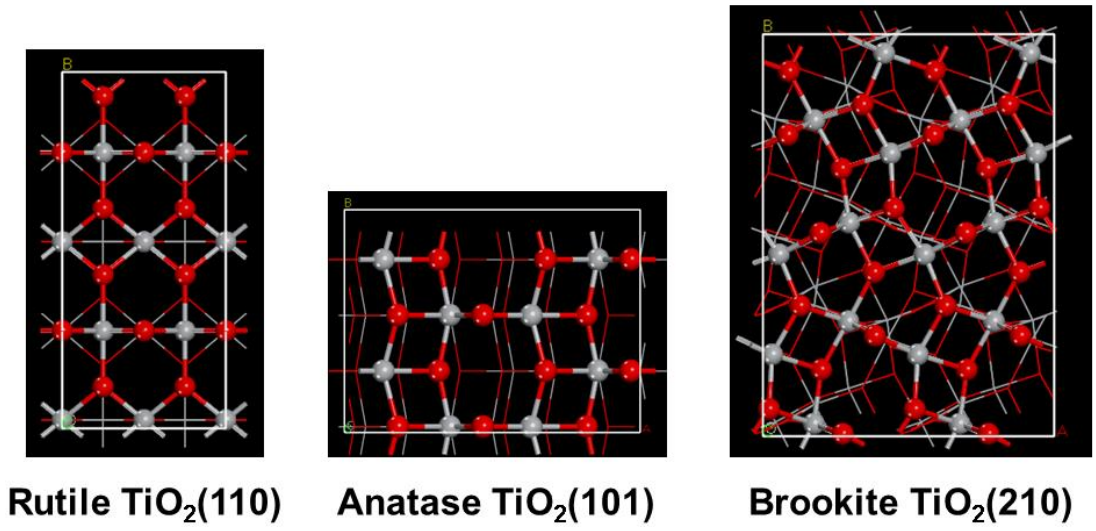

Figure 9.1. Top views of rutile TiO_2(110), anatase TiO_2(101), and brookite TiO_2(210) surfaces. Ti, grey; O, red.

9.2.1 H_2 dissociation on rutile TiO_2(110). We first examined the homolytic and heterolytic pathways on rutile TiO_2(110) surface. The homolytic dissociation of H_2 takes place on two contiguous surface oxygens, which gives rise to the formation of two O─H groups on the surface. The heterolytic dissociation of H_2 occurs on adjacent Ti and O sites, which leads to the formation of the corresponding Ti─H and O─H bonds (Figure

9.3 middle). The energy profiles are shown in Figure 9.2. As one can see, the homolytic dissociation is highly exothermic (ΔE = -1.33 eV), while has a very high energy barrier (Ea = 1.39 eV). The heterolytic dissociation, however, has a much lower energy barrier (Ea = 0.37 eV), but is more thermoneutral (ΔE = -0.10 eV). This means that the homolytic dissociation of H_2 is thermodynamically more favorable, while the heterolytic dissociation of H_2 is kinetically most likely. More interestingly, we find that the hydride (H^-) at the Ti site, which is produced by the heterolytic dissociation of H_2, can transfer to O easily with an energy barrier of 0.99 eV. The transition state associated with this step (TS3 in Figure 9.2) is 0.60 eV lower than the transition sate of the homolytic dissociation (TS2 in Figure 9.2). Thus, H_2 dissociation on rutile TiO_2(110) surface does not go through the homolytic pathway, but via a heterolytic pathway followed by the transfer of hydrogen from Ti to O, finally yielding the homolytic product. This kind of mechanism has also been proposed for CeO_2(111) previously.[34]

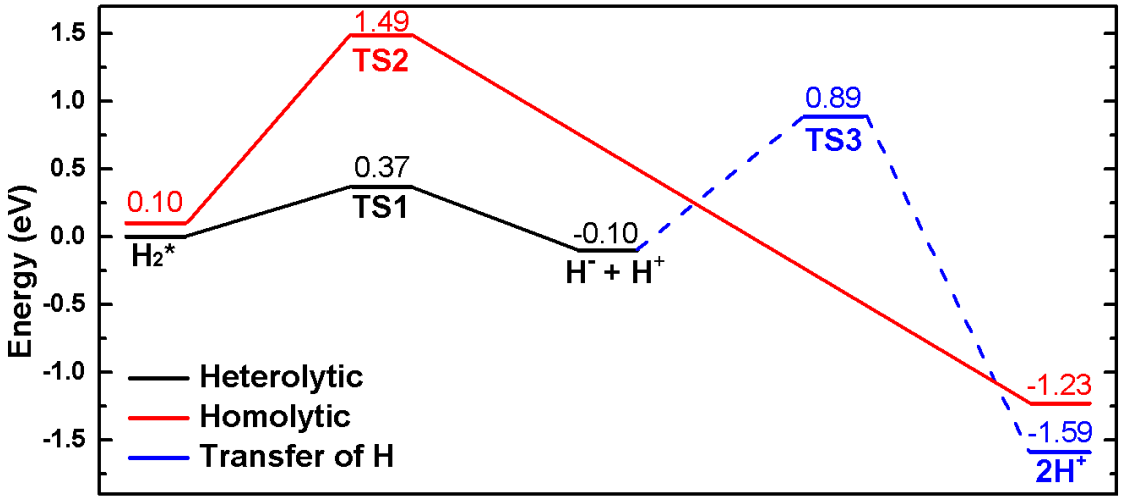

Figure 9.2. Heterolytic pathway (black line) combined with the transfer of H from Ti to O (blue line) and homolytic pathway (red line) for H_2 dissociation on rutile TiO_2(110) surface.

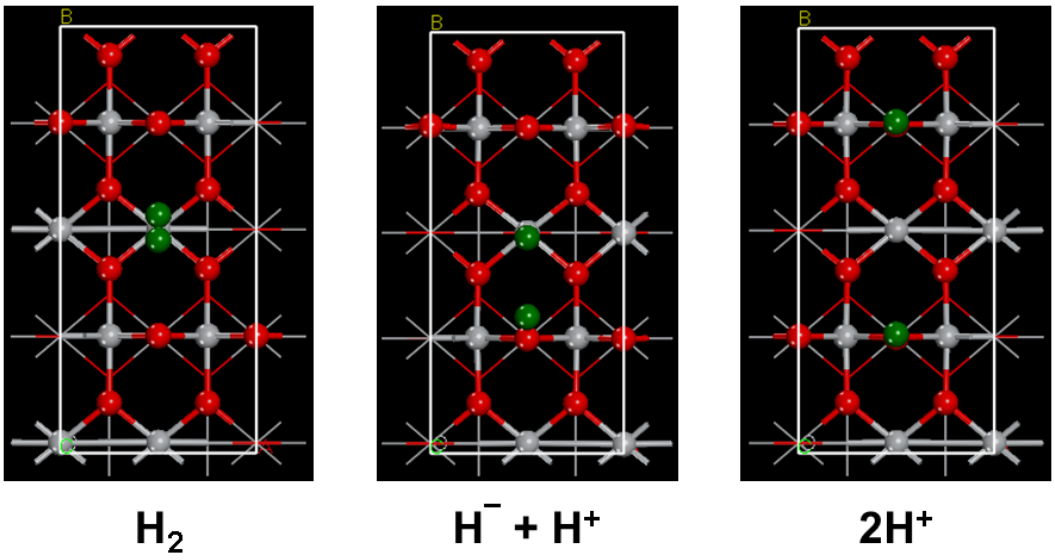

Figure 9.3. Optimized geometry structures of H_2, $H^- + H^+$, and $2H^+$ on rutile TiO_2(110) surface. Ti, grey; O, red; H, green.

Figure 9.3 shows the optimized geometry structures of H_2, $H^- + H^+$, and $2H^+$ on rutile TiO_2(110) surface. To understand the extremely low energy barrier (0.37 eV) of the heterolytic dissociation of H_2, as compared with the energy barrier (1.49 eV) of the

homolytic dissociation, we calculated the partial atomic charges on the surface Ti and O atoms of rutile TiO_2(110). It is found that the charges on surface Ti and O atoms are +2.012 |e| and -0.925 |e|, respectively. The oppositely charged Ti and O atoms can generate a strong electric field, and polarize the adsorbed H_2 molecule, eventually helping the heterolytic dissociation of H_2.[34] This is supported by the charges on the two H atoms of the adsorbed H_2 molecule: -0.032 |e| on one H, while +0.060 |e| on the other one. In addition, the H─H bond is slightly weakened after the adsorption on the surface, as is evident from its lengthening to 0.762 Å in comparison with the gas-phase value of 0.752 Å.

9.2.2 H_2 dissociation on anatase TiO_2(101). Then we studied H_2 dissociation on anatase(101) surface. As shown in Figure 9.4, the homolytic dissociation of H_2 is exothermic (ΔE = -0.56 eV), but has an extremely high energy barrier (Ea = 2.07 eV). The heterolytic dissociation of H_2 has a smaller barrier (Ea = 1.04 eV), but is endothermic (ΔE = 0.46 eV). This is in the same scenario as rutile TiO_2(110): the homolytic pathway is thermodynamically more favorable, while the heterolytic pathway is kinetically more favorable. However, the different thing is, the energy barrier for the transfer of hydrogen from Ti to O on anatase TiO_2(101) is very high (Ea = 1.68 eV). Moreover, the transition state associated with this step (TS3 in Figure 9.4) has the same energy as the transition sate of the homolytic dissociation (TS2 in Figure 9.4). This indicates that hydrides on anatase TiO_2(101) can be kinetically stabilized. Thus, it is expected that these hydrides can be detected experimentally by ^{1}H-NMR or inelastic

neutron scattering (INS). They can be also evolved in the hydrogenation reactions of C-C or C-O multiple bonds.

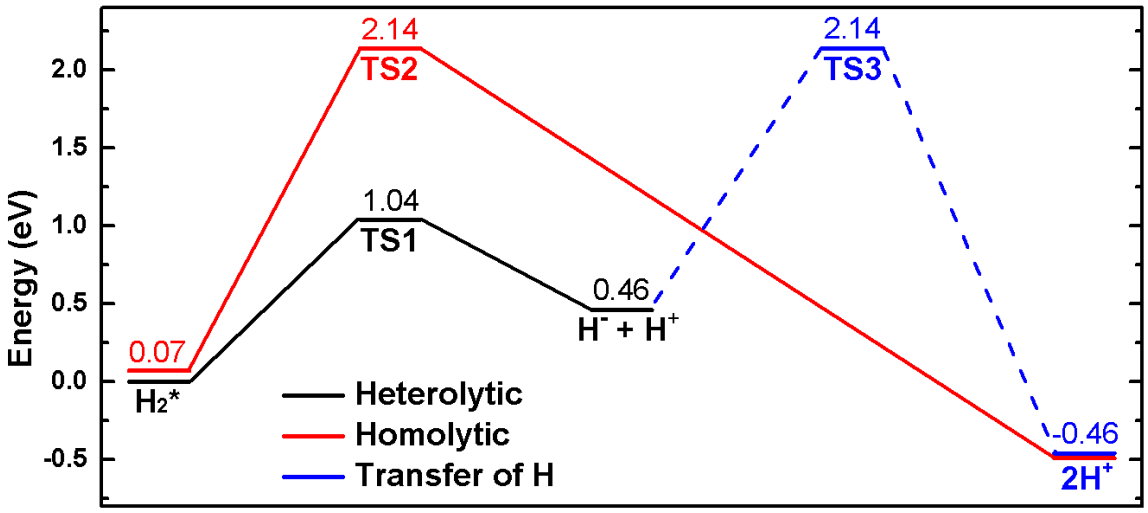

Figure 9.4. Heterolytic pathway (black line) combined with the transfer of H from Ti to O (blue line) and homolytic pathway (red line) for H_2 dissociation on anatase TiO_2(101) surface.

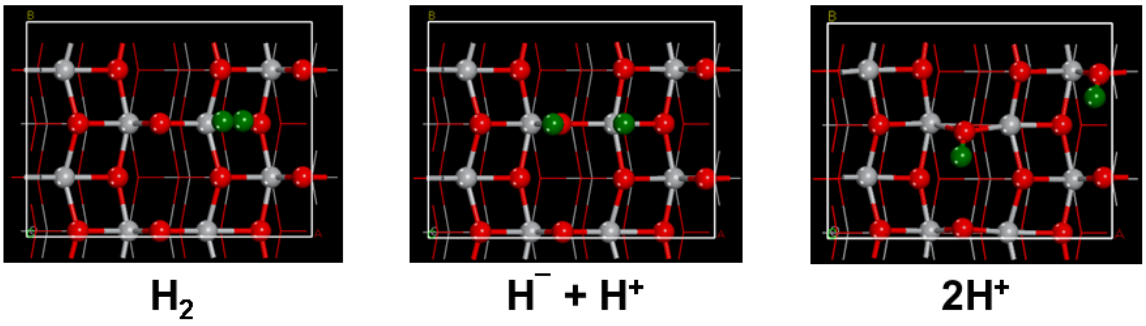

Figure 9.5. Optimized geometry structures of H_2, H^- + H^+, and $2H^+$ on anatase TiO_2(101) surface. Ti, grey; O, red; H, green.

Figure 9.5 shows the optimized geometry structures of H_2, H^- + H^+, and $2H^+$ on anatase TiO_2(101) surface. The partial atomic charges on surface Ti and O atoms of anatase TiO_2(101) are found to be +2.009 |e| and -0.903 |e|, respectively. Therefore, like

rutile TiO_2(110), the oppositely charged Ti and O atoms can generate an electric field and polarize the adsorbed H_2 molecule, benefitting the heterolytic dissociation of H_2.

9.2.3 H_2 dissociation on brookite TiO_2(210). At last, we compared the heterolytic and homolytic pathways on brookite TiO_2(210). As shown in Figure 9.6, just like rutile TiO_2(110) and anatase TiO_2(101), the homolytic pathway is thermodynamically more favorable, while the heterolytic pathway is kinetically more favorable. Specifically speaking, the homolytic H_2 dissociation is exothermic (ΔE = -0.75 eV), but has a very high barrier of 1.97 eV. The heterolytic H_2 dissociation has a much lower barrier of 0.98 eV, but is endothermic (ΔE = 0.33 eV). Furthermore, the barrier of hydrogen transfer from Ti to O on brookite TiO_2(210) is 1.48 eV. The transition state associated with this step (TS3 in Figure 9.6) is 0.27 eV lower than that of the homolytic dissociation (TS2 in Figure 9.6). This indicates that, similar as rutile TiO_2(110), H_2 dissociation on brookite TiO_2(210) surface is also via a heterolytic pathway followed by the transfer of hydrogen from Ti to O instead of the homolytic pathway.

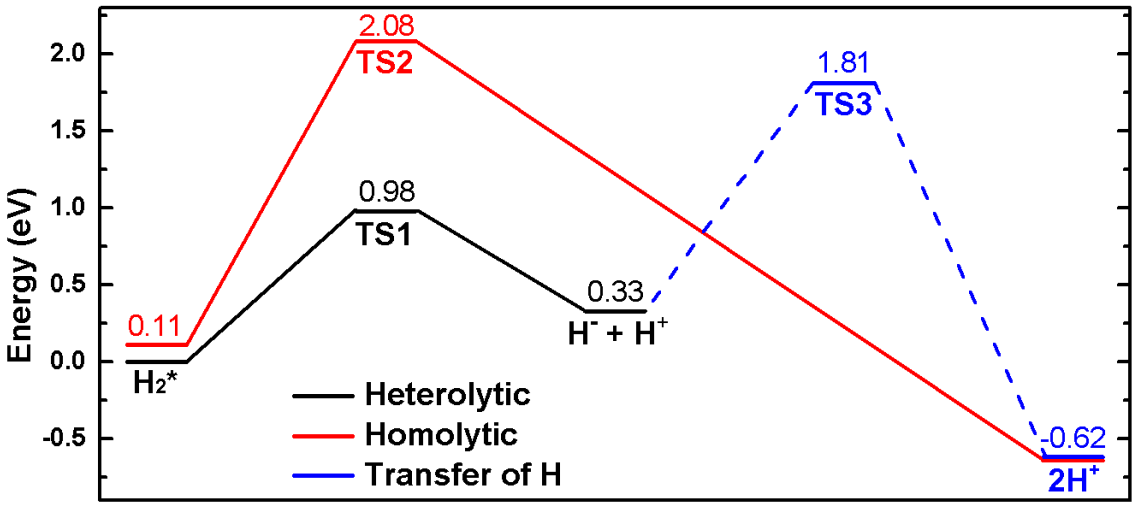

Figure 9.6. Heterolytic pathway (black line) combined with the transfer of H from Ti to O (blue line) and homolytic pathway (red line) for H_2 dissociation on brookite TiO_2(210) surface.

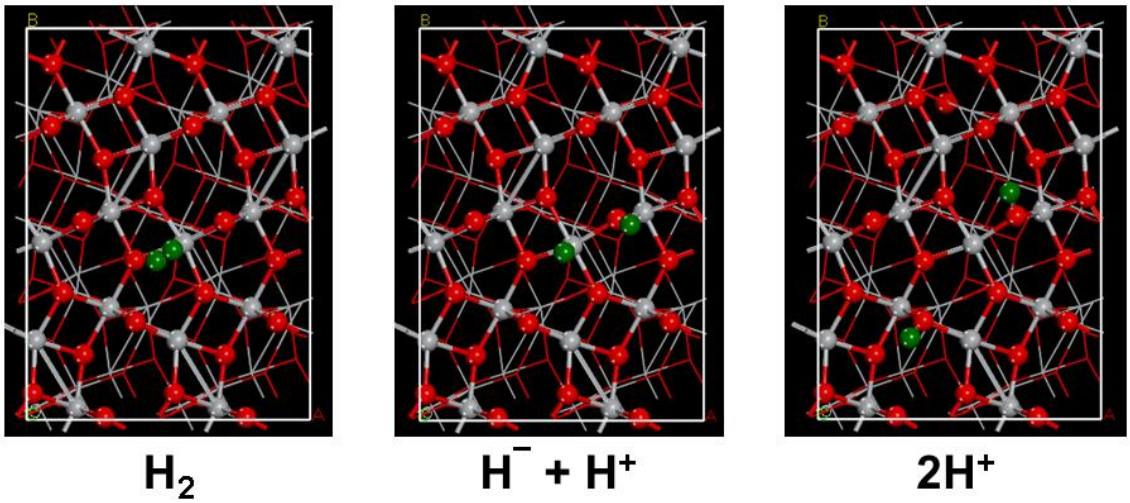

Figure 9.7 Optimized geometry structures of H_2, $H^- + H^+$, and $2H^+$ on brookite TiO_2(210) surface. Ti, grey; O, red; H, green.

Figure 9.7 shows the optimized geometry structures of H_2, $H^- + H^+$, and $2H^+$ on brookite TiO_2(210). We also calculated the partial atomic charges on surface Ti and O atoms of brookite TiO_2(210), and it is found to be +2.012 |e| on Ti and -0.891 |e| on O.

Similar as the above two surfaces, the oppositely charged Ti and O atoms can generate a strong electric field, which will help the breaking of H─H bond to produce H^- and H^+ on the surface.

9.2.4 Comparison of rutile TiO_2(110), anatase TiO_2(101), and brookite TiO_2(210). The barriers of heterolytic H_2 dissociation on the three TiO_2 surfaces follow the trend of anatase TiO_2(101) > brookite TiO_2(210) > rutile TiO_2(110). This can be explained by the polarization strength of the adsorbed H_2 molecules on the surfaces. We find that the polarization strength of the H_2 molecules on the three TiO_2 surfaces follows the opposite trend (anatase TiO_2(101) < brookite TiO_2(210) < rutile TiO_2(110)). This is evidenced by the charge difference between the two H atoms and the H─H bond length of the H_2 molecule (Table 9.1). The more polarized of the H_2 molecule, the easier of its heterolytic dissociation.

Table 9.1. Comparison of the heterolytic H_2 dissociation on rutile TiO_2(110), anatase TiO_2(101), and brookite TiO_2(210) surfaces. Energy barrier (Ea), Bader charge on H1 (P_{H1}), Bader charge on H2 (P_{H2}), charge difference between H1 and H2 (ΔP_H), and distance of H1-H2 bond (d_{H1-H2}).

	Rutile TiO_2(110)	**Anatase TiO_2(101)**	**Brookite TiO_2(210)**
Ea/eV	0.37	1.04	0.98
P_{H1} /|e|	-0.032	-0.001	-0.013
P_{H2} /|e|	+0.060	+0.013	+0.045
ΔP_H/|e|	0.092	0.014	0.058
d_{H1-H2} /Å	0.762	0.758	0.761
(free H_2 = 0.752 Å)			

The barriers of hydrogen transfer from Ti to O on the three TiO_2 surfaces follow the trend of anatase TiO_2(101) > brookite TiO_2(210) > rutile TiO_2(110). To understand the relatively low barriers of hydrogen transfer on rutile TiO_2(110) and brookite TiO_2(210) surfaces, we compared the transition states associated with this step on the three surfaces. As shown in Figure 9.8, we find that the Ti-O pentagons (highlight in yellow circle) on rutile TiO_2(110) and brookite TiO_2(210) helped the transfer of hydrogen from Ti to O. Due to the absence of this unique structure, hydrogen transfer on anatase TiO_2(101) is very hard. We also tested the transfer of hydrogen from Ti to the three coordinated O, then to the two coordinated O on anatase TiO_2(101). However, the barrier also turned to be high: the barrier of hydrogen transfer from Ti to the nearest three coordinated O is 1.67 eV.

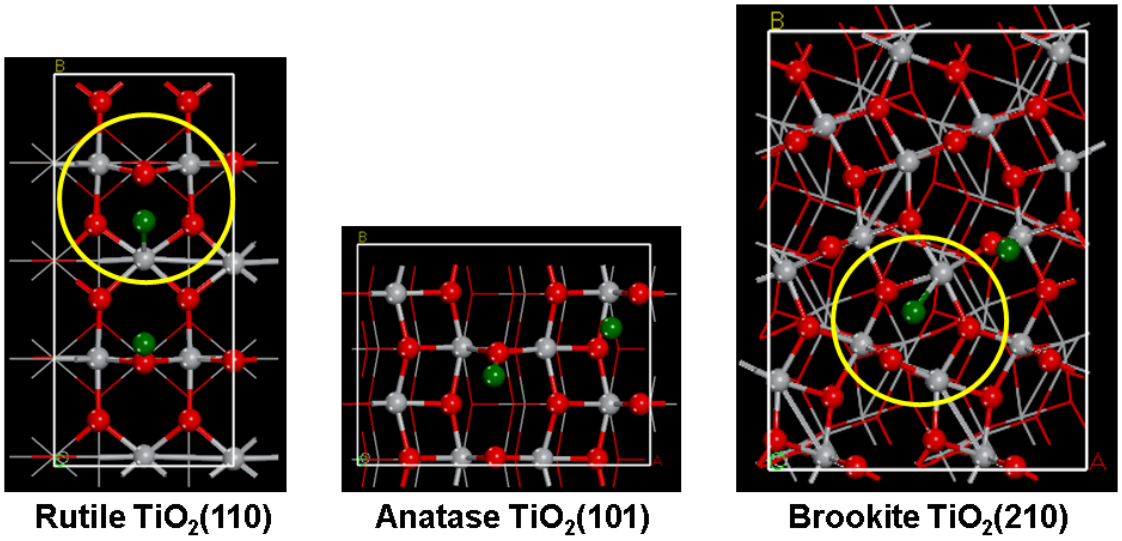

Figure 9.8. Comparison of the transition states for H transfer from Ti to O on rutile TiO_2(110), anatase TiO_2(101), and brookite TiO_2(210) surfaces. The Ti-O pentagons are highlight in yellow circles. Ti, grey; O, red; H, green.

9.3 Implications of H_2 activations on TiO_2. Our study of H_2 activations on TiO_2 surfaces presents several interesting implications. First it implies that other reducible metal oxides, which only show O–H bands in the infrared spectra, may also favor the heterolytic dissociation of H_2 followed by the transfer of hydrogen from the metal site to the O site rather than the homolytic dissociation of H_2. Second, our study shows that the mechanistic proposal of H_2 dissociation based on the FTIR data for the reducible metal oxides is not conclusive. This is because the above experimental observations are indirect, and cannot provide evidence of the operating mechanism. Spectroscopic tools including ^{1}H-NMR and INS can be powerful to detect the hydride species on the metal oxides. At last, our study indicates that brookite TiO_2 (210) is more reactive than anatase TiO_2 (101). This is in agreement with a previous theoretical study of water and formic acid adsorption

on anatase TiO_2 (101) and brookite TiO_2 (210) surfaces.[35] Brookite TiO_2(210) has the same structural building block as anatase TiO_2(101), but the interatomic distances are slightly shorter and the blocks are arranged in a different way. Here we find that the junctions between different structural unites on brookite TiO_2(210) are the active sites for the transfer of hydrogen.

9.4 Conclusions

We have investigated the mechanisms of H_2 dissociation on different TiO_2 polymorphs, namely rutile TiO_2(110), anatse TiO_2(101), and brookite TiO_2(210), by first-principles DFT. We find that for all the three surfaces, although the homolytic dissociation of H_2 is thermodynamically more favorable, the heterolytic pathway is kinetically more favorable. For rutile TiO_2(110) and brookite TiO_2(210), the hydrides which are produced by the heterolytic dissociation of H_2 can easily transfer from Ti to O, finally yielding the homolytic products. However, for anatase TiO_2(101), the energy barrier of hydrogen transfer form Ti to O is very high. This indicates that hydrides on anatase TiO_2(101) can be kinetically stabilized. Thus, it is expected that hydrides on anatase TiO_2(101) can be detected by ^{1}H-NMR or INS. In addition, the hydrides can be also evolved in the hydrogenation reactions of C-C or C-O multiple bonds. Our study sheds light on the mechanisms of H_2 dissociation on TiO_2, and provides valuable guidelines to experimental researchers for the detection of hydrides on TiO_2 or other reducible metal oxides and the use of metal oxide catalysts for hydrogenation reactions.

References

1. Diebold, U.; Ruzycki, N.; Herman, G. S.; Selloni, A., One Step Towards Bridging the Materials Gap: Surface Studies of Tio_2 Anatase. *Catal. Today* **2003**, *85*, 93-100.

2. Chen, X.; Mao, S. S., Titanium Dioxide Nanomaterials: Synthesis, Properties, Modifications, and Applications. *Chem. Rev.* **2007**, *107*, 2891-2959.

3. Foo, G. S.; Hu, G.; Hood, Z. D.; Li, M.; Jiang, D.-e.; Wu, Z., Kinetics and Mechanism of Methanol Conversion over Anatase Titania Nanoshapes. *ACS Catal.* **2017**, *7*, 5345-5356.

4. Yan, Y.; Shi, W.; Yuan, Z.; He, S.; Li, D.; Meng, Q.; Ji, H.; Chen, C.; Ma, W.; Zhao, J., The Formation of Ti–H Species at Interface Is Lethal to the Efficiency of Tio_2-Based Dye-Sensitized Devices. *J. Am. Chem. Soc.* **2017**, *139*, 2083-2089.

5. Diebold, U., The Surface Science of Titanium Dioxide. *Surf. Sci. Rep.* **2003**, *48*, 53-229.

6. Ranade, M.; Navrotsky, A.; Zhang, H.; Banfield, J.; Elder, S.; Zaban, A.; Borse, P.; Kulkarni, S.; Doran, G.; Whitfield, H., Energetics of Nanocrystalline Tio_2. *Proc. Natl. Acad. Sci.* **2002**, *99*, 6476-6481.

7. Amores, J. M. G.; Escribano, V. S., Anatase Crystal Growth and Phase Transformation to Rutile in High-Area Tio_2, Moo_3–Tio_2 and Other Tio_2-Supported Oxide Catalytic Systems. *J. Mater. Chem.* **1995**, *5*, 1245-1249.

8. Lazzeri, M.; Vittadini, A.; Selloni, A., Structure and Energetics of Stoichiometric Tio_2 Anatase Surfaces. *Phys. Rev. B* **2001**, *63*, 155409.

9. Penn, R. L.; Banfield, J. F., Oriented Attachment and Growth, Twinning, Polytypism, and Formation of Metastable Phases: Insights from Nanocrystalline Tio_2. *Am. Mineral.* **1998**, *83*, 1077-1082.

10. Isley, S. L.; Penn, R. L., Relative Brookite and Anatase Content in Sol− Gel-Synthesized Titanium Dioxide Nanoparticles. *J. Phys. Chem. B* **2006**, *110*, 15134-15139.

11. Chen, X.; Liu, L.; Peter, Y. Y.; Mao, S. S., Increasing Solar Absorption for Photocatalysis with Black Hydrogenated Titanium Dioxide Nanocrystals. *Science* **2011**, *331*, 746-750.

12. Sun, C.; Jia, Y.; Yang, X.-H.; Yang, H.-G.; Yao, X.; Lu, G. Q.; Selloni, A.; Smith, S. C., Hydrogen Incorporation and Storage in Well-Defined Nanocrystals of Anatase Titanium Dioxide. *J. Phys. Chem. C* **2011**, *115*, 25590-25594.

13. Zheng, Z.; Huang, B.; Lu, J.; Wang, Z.; Qin, X.; Zhang, X.; Dai, Y.; Whangbo, M.-H., Hydrogenated Titania: Synergy of Surface Modification and Morphology Improvement for Enhanced Photocatalytic Activity. *Chem. Commun.* **2012**, *48*, 5733-5735.

14. Liu, L.; Peter, Y. Y.; Chen, X.; Mao, S. S.; Shen, D., Hydrogenation and Disorder in Engineered Black Tio_2. *Phys. Rev. Lett.* **2013**, *111*, 065505.

15. Coperet, C.; Estes, D. P.; Larmier, K.; Searles, K., Isolated Surface Hydrides: Formation, Structure, and Reactivity. *Chem. Rev.* **2016**, *116*, 8463-8505.

16. Henrich, V. E.; Kurtz, R. L., Surface Electronic Structure of Tio_2: Atomic Geometry, Ligand Coordination, and the Effect of Adsorbed Hydrogen. *Phys. Rev. B* **1981**, *23*, 6280.

17. Kunat, M.; Burghaus, U.; Wöll, C., The Adsorption of Hydrogen on the Rutile Tio_2(110) Surface. *Phys. Chem. Chem. Phys.* **2004**, *6*, 4203-4207.

18. Suzuki, S.; Fukui, K.-i.; Onishi, H.; Iwasawa, Y., Hydrogen Adatoms on Tio_2(110)−(1× 1) Characterized by Scanning Tunneling Microscopy and Electron Stimulated Desorption. *Phys. Rev. Lett.* **2000**, *84*, 2156.

19. Fujino, T.; Katayama, M.; Inudzuka, K.; Okuno, T.; Oura, K.; Hirao, T., Surface Hydroxyl Formation on Vacuum-Annealed Tio_2(110). *Appl. Phys. Lett.* **2001**, *79*, 2716-2718.

20. Leconte, J.; Markovits, A.; Skalli, M.; Minot, C.; Belmajdoub, A., Periodic Ab Initio Study of the Hydrogenated Rutile Tio_2(110) Surface. *Surf. Sci.* **2002**, *497*, 194-204.

21. Calatayud, M.; Minot, C., Effect of Relaxation on Structure and Reactivity of Anatase (100) and (001) Surfaces. *Surf. Sci.* **2004**, *552*, 169-179.

22. Islam, M. M.; Calatayud, M.; Pacchioni, G., Hydrogen Adsorption and Diffusion on the Anatase Tio_2(101) Surface: A First-Principles Investigation. *J. Phys. Chem. C* **2011**, *115*, 6809-6814.

23. Aschauer, U.; Selloni, A., Hydrogen Interaction with the Anatase Tio_2(101) Surface. *Phys. Chem. Chem. Phys.* **2012**, *14*, 16595-16602.

24. Reedijk, J.; Poeppelmeier, K., *Comprehensive Inorganic Chemistry Ii: From Elements to Applications*; Elsevier Ltd, 2013; Vol. 9.

25. Binet, C.; Daturi, M.; Lavalley, J.-C., Ir Study of Polycrystalline Ceria Properties in Oxidised and Reduced States. *Catal. Today* **1999**, *50*, 207-225.

26. Gribov, E. N.; Bertarione, S.; Scarano, D.; Lamberti, C.; Spoto, G.; Zecchina, A., Vibrational and Thermodynamic Properties of H_2 Adsorbed on Mgo in the 300− 20 K Interval. *J. Phys. Chem. B* **2004**, *108*, 16174-16186.

27. Joubert, J.; Salameh, A.; Krakoviack, V.; Delbecq, F.; Sautet, P.; Copéret, C.; Basset, J. M., Heterolytic Splitting of H_2 and Ch_4 on Γ-Alumina as a Structural Probe for Defect Sites. *J. Phys. Chem. B* **2006**, *110*, 23944-23950.

28. Chen, H. T.; Giordano, L.; Pacchioni, G., From Heterolytic to Homolytic H_2 Dissociation on Nanostructured Mgo(001) Films as a Function of the Metal Support. *J. Phys. Chem. C* **2013**, *117*, 10623-10629.

29. Panayotov, D. A.; Yates Jr, J. T., N-Type Doping of Tio_2 with Atomic Hydrogen-Observation of the Production of Conduction Band Electrons by Infrared Spectroscopy. *Chem. Phys. Lett.* **2007**, *436*, 204-208.

30. Barzan, C.; Groppo, E.; Bordiga, S.; Zecchina, A., Defect Sites in H_2-Reduced Tio_2 Convert Ethylene to High Density Polyethylene without Activator. *ACS Catal.* **2014**, *4*, 986-989.

31. Pan, J. M.; Maschhoff, B.; Diebold, U.; Madey, T., Interaction of Water, Oxygen, and Hydrogen with Tio_2(110) Surfaces Having Different Defect Densities. *J. Vac. Sci. Technol., A* **1992**, *10*, 2470-2476.

32. Knotek, M., Characterization of Hydrogen Species on Tio_2 by Electron-Stimulated Desorption. *Surf. Sci. Lett.* **1980**, *91*, L17-L22.

33. Esch, T. R.; Gadaczek, I.; Bredow, T., Surface Structures and Thermodynamics of Low-Index of Rutile, Brookite and Anatase–a Comparative Dft Study. *Appl. Surf. Sci.* **2014**, *288*, 275-287.

34. García-Melchor, M.; López, N. r., Homolytic Products from Heterolytic Paths in H_2 Dissociation on Metal Oxides: The Example of Ceo_2. *J. Phys. Chem. C* **2014**, *118*, 10921-10926.

35. Li, W.-K.; Gong, X. Q.; Lu, G.; Selloni, A., Different Reactivities of Tio_2 Polymorphs: Comparative Dft Calculations of Water and Formic Acid Adsorption at Anatase and Brookite Tio_2 Surfaces. *J. Phys. Chem. C* **2008**, *112*, 6594-6596.

Chapter 10

Conclusions

We have employed first principles density functional theory (DFT) techniques to investigate how hydrogen interacts with various materials, including cobalt phosphide (CoP), h-BN monolayer supported on transition metals (h-BN/metal), atomically precise gold nanoclusters, and titanium dioxide (TiO_2). For the solids and surfaces, we used the Vienna *ab initio* simulation package (VASP)[1] to perform DFT calculations with periodic boundary conditions (PBC) and plane-wave basis sets. The Perdew−Burke−Ernzerhof (PBE) form of the generalized gradient approximation was used for electron exchange and correlation.[2] The ion-electron interaction was described by projector augmented wave (PAW) method.[3] For the molecules and nanoclusters, we used the Turbomole program (Version 6.5)[4] without the periodic boundary conditions at the same DFT-PBE level with the def2-SVP basis sets.[5]

Chapter 2 presents the interaction between hydrogen and the low-Miller-index surfaces of CoP, including (111), (110), (100), and (011). We find that the (111) surface of CoP is the most promising facet for high and long-lived HER activity. The key feature of hydrogen adsorption on the (111) surface is that both Co bridge sites and P top sites are able to adsorb hydrogen with close-to-zero ΔG_H and that there is a synergy of Co and P atoms in adsorbing hydrogen.

In Chapter 3, we investigate the interaction between hydrogen and h-BN/metal systems (metal = Ni, Co, and Cu). We find that hydrogen adsorption is greatly reduced on the h-BN/metal surface, in comparison with hydrogen adsorption on the pure metal surface. This different adsorption leads to selectivity control for HER vs. CO_2 reduction. We find that h-BN/Ni and h-BN/Co can be very good electrocatalysts for CO_2 reduction to HCOOH by avoiding HER.

Chapter 4-7 present our study of atomically precise gold nanoclusters, which are a new class of catalysts. In Chapter 4, we study the thiolate-gold interface and find that the interfacial structures of thiolates on gold are surface sensitive. With this surface sensitivity, we categorize the structure-known $Au_n(SR)_m$ clusters into three groups: (1) no bridging; (2) ambiguous bridging; (3) distinct bridging. To understand HER on the thiolate-protected gold nanoclusters, in Chapter 5, we study how hydrogen interacts with $[Au_{25}(SR)_{18}]^q$ clusters (q=-1, 0, +1) and monoatom-doped bimetallic $[M_1Au_{24}(SR)_{18}]^q$ clusters (M=Pt, Pd, Ag, Cu, Hg, Cd, and q=-2, -1, 0). We find that hydrogen behaves as a metal in these clusters and contributes its 1s electron to the superatomic free-electron count. By calculating ΔG_H, we predict that $PtAu_{24}(SR)_{18}$, $PdAu_{24}(SR)_{18}$, and $CuAu_{24}(SR)_{18}$ clusters can be very good electrocatalysts for HER. Unlike the above thiolate-protected gold nanoclusters, where the surface gold atoms are fully coordinated by the thiolate ligands, the $Au_{22}(L^8)_6$ cluster (L = 1,8-bis(diphenylphosphino) octane) is unique in that it contains eight coordinatively unsaturated (*cus*) gold atoms. In Chapter 6, we investigate the interaction between hydrogen and the $Au_{22}(L^8)_6$ cluster. We find that the eight *cus* Au atoms in the $Au_{22}(L^8)_6$ cluster can adsorb hydrogen stronger than Pt,

thereby being a potentially promising catalyst for HER. In addition, we find that hydrogen behaves as a hydride or electron-withdrawing ligand in the $Au_{22}(L^8)_6$ clusters, in contrast with the metallic hydrogen in thiolate-protected Au nanoclusters. The electrocatalytic applications of atomically precise metal nanoclusters have shown great promise, so in Chapter 7 we highlight recent advances in electrocatalysis by atomically precise metal nanoclusters for water splitting, CO_2 reduction, and some other reactions.

So far we have discussed hydrogen interaction with zero-dimensional (Au nanoclusters), two-dimensional (h-BN monolayer), and three dimensional (CoP) materials. Hydrogen interaction with metal oxides is of growing interest recently. TiO_2 is one of the most important and extensively studied metal oxides. Chapter 8 presents the interaction between hydrogen and TiO_2 surfaces. We find that, for rutile TiO_2(110), anatse TiO_2(101), and brookite TiO_2(210), although the homolytic dissociation of H_2 is thermodynamically more favorable, the heterolytic pathway is kinetically more favorable. Moreover, we find that hydrides on anatase TiO_2(101) can be kinetically stabilized. Thus, it is expected that hydrides on anatase TiO_2(101) can be detected by ^{1}H-NMR or INS.

In conclusion, we have studied hydrogen interaction with different catalytic systems from first principles DFT. Our study has important implications for the use of the catalysts for HER, CO_2 reduction, and H_2 activation. Here are several key points I have learned from the projectes: (1) Interface engineering can be a very powerful method to tune the electronic structure and reaction activities of the catalysts. For example, Ni is a good catalyst for HER, however, after the interface/surface engineering with h-BN monolayer, it becomes a good catalyst for CO_2 reduction. (2) In the metal nanoclusters,

hydrogen-metal interaction is very flexible. Hydrogen can behave as a metal in thiolate-protected gold clusters, and behave as a hydride in phosphine-protected gold clusters. (3) Creating *cus* metal sites in the metal nanoclusters is critical to improving their abilities for activating small molecules. It has been shown that the eight *cus* gold atoms in the $Au_{22}(L^8)_6$ cluster can be very promising for catalysis. (4) Hydrides can be stabilized on the metal oxide surfaces. Therefore, metal oxides can be also used as hydrogenation catalysts. Looking into the future, molecular dynamics and multi-scale modeling can help us have a deeper understanding of the processes of hydrogen interaction with the materials.

References

1. Kresse, G.; Furthmüller, J., Efficient Iterative Schemes for Ab Initio Total-Energy Calculations Using a Plane-Wave Basis Set. *Phys. Rev. B* **1996**, *54*, 11169-11186.

2. Perdew, J. P.; Burke, K.; Ernzerhof, M., Generalized Gradient Approximation Made Simple. *Phys. Rev. Lett.* **1996**, *77*, 3865-3868.

3. Blöchl, P. E., Projector Augmented-Wave Method. *Phys. Rev. B* **1994**, *50*, 17953-17979.

4. Ahlrichs, R.; Bär, M.; Häser, M.; Horn, H.; Kölmel, C., Electronic Structure Calculations on Workstation Computers: The Program System Turbomole. *Chem. Phys. Lett.* **1989**, *162*, 165-169.

5. Schäfer, A.; Horn, H.; Ahlrichs, R., Fully Optimized Contracted Gaussian Basis Sets for Atoms Li to Kr. *J. Chem. Phys.* **1992**, *97*, 2571-2577.